学位論文

Study of $\overline{K}NN$ system produced via the stopped K^- absorption reactions in the FINUDA experiment

FINUDA 実験における静止 K^- 吸収反応により生成される $\overline{K}NN$ 系の研究

平成 19 年 12 月 博士（理学）申請

東京大学大学院理学系研究科
物理学専攻

藤岡 宏之

Abstract

We have carried out the second data taking of the FINUDA (acronym for "FIsica NUcleare a DAΦNE") experiment to study strangeness nuclear physics via the kaon absorption reaction at rest on p-shell nuclei (^{6}Li, ^{7}Li, ^{9}Be, ^{13}C, and D_2O), at a ϕ-factory DAΦNE (acronym for "Double Annular ϕ-factory for Nice Experiments") in LNF-INFN (Laboratori Nazionali di Frascati, Instituto Nazionale di Fisica Nucleare). The data taking started in November 2006, and ended in June 2007. The total integrated luminosity reached $966\,\mathrm{pb}^{-1}$, which is about 5 times more than the first data taking in 2003–2004.

We have succeeded in observing pairs of Λn, $\Sigma^- p$ as well as Λp in good statistics. They showed a back-to-back angular correlation characteristic to the emission from two-nucleon absorption. For these correlated pairs of Λn and $\Sigma^- p$, the energy sum distribution showed an enhancement near the threshold. It suggests that the quasi-free two-nucleon absorption process is existent, at least for Λn and $\Sigma^- p$ pairs. The exclusive measurement of the hyperon-nucleon pairs made it possible to evaluate the yield of each combination. The yield for Λn and $\Sigma^- p$ has been obtained as 2–3% and 0.2–1.1% per stopped K^-, depending on the target. The contribution other than quasi-free two-nucleon absorption was also estimated for Λn, and it was found to be $\sim 2\%$ per stopped K^- at most.

On the other hand, the energy sum of Λp pairs did not show an enhancement near the threshold. The yield in the near-threshold region was only 0.2–0.4% per stopped K^-, much smaller than the total yield of 0.9–2.4%. It was found that the strength in the near-threshold region relative to the total was small, in contrast with the case of Λn. Thus, it indicates a different production mechanism for the correlated Λp pairs from quasi-free two-nucleon absorption.

In the previous data taking, we found the invariant mass of the Λp pairs distributed much lower than the threshold of a kaon and two protons. The newly observed invariant mass spectrum of Λp was consistent with the result of the previous data taking. There was no significant difference of the spectra among the different targets. The strength in the bound region may indicate the existence of $K^- pp$ bound states, although there are no realistic theoretical calculations on the production of $K^- pp$ bound state in kaon absorption to be compared.

Contents

List of Figures

List of Tables

Chapter 1

Introduction

1.1 Antikaon-nuclear bound states

Strangeness nuclear physics is an extension of the traditional nuclear physics by adding the strangeness degree of freedom. One of main subjects is related to hypernuclei, which include hyperon(s), such as Λ, Σ or Ξ. Spectroscopic study, such as formation spectroscopy and γ-ray spectroscopy, will give an almost unique information on baryon-baryon interaction, since a scattering experiment with a hyperon beam is difficult to be carried out because of the short lifetime of hyperons.

Whereas a hypernucleus is a baryon system like a normal nucleus, an antikaon-nuclear bound state, where an antikaon is the lightest meson with strangeness -1, has been extensively investigated both theoretically and experimentally in this decade. It can be considered as a highly excited (200–300 MeV) system, compared with a Λ-hypernucleus in the strangeness -1 sector. The possible existence of such an exotic bound state is assisted by the strong attraction between $\overline{K}N$ with isospin 0.

1.1.1 Antikaon-nucleon interaction

Low-energy antikaon-nucleon interaction has been investigated via two ways; $\overline{K}N$ scattering and X-ray measurement of kaonic hydrogen.

Martin obtained the scattering length for isospin 0 and 1 from low-energy K^-p scattering data as [1]:

$$a^{I=0} = -1.70 + 0.68i\,\mathrm{fm}, \tag{1.1}$$

$$a^{I=1} = 0.37 + 0.60i\,\mathrm{fm}. \tag{1.2}$$

The measurement of the K_α X-ray ($2p \to 1s$ transition) of kaonic hydrogen gives the shift ($\Delta E = E^{\mathrm{measured}} - E^{\mathrm{e.m.}}$) and width ($\Gamma$) of the ground state caused by strong interaction, compared with the pure electromagnetic value ($E^{\mathrm{e.m.}}$). They are related with the K^-p scattering length by the Deser relation:

$$\Delta E + i\frac{\Gamma}{2} = 2\alpha^3\mu^2 a_{K^-p}, \tag{1.3}$$

where α is the fine structure constant and μ is the reduced mass of the K^--p system.

Because the scattering length for K^-p can be expressed in the isospin limit, as:

$$a_{K^-p} = \frac{1}{2}(a^{I=0} + a^{I=1}), \tag{1.4}$$

a_{K^-p} was expected to be negative from Martin's results, which means the repulsive shift of the ground state of kaonic hydrogen. However, old measurements [2–4] showed attractive shifts. It had been a long-standing puzzle on $\overline{K}N$ interaction.

Recently, the KEK-PS E228 (KpX) experiment successfully observed the K_α peak clearly in the repulsive region [5, 6] and they obtained the shift and width as:

$$\Delta E = -323 \pm 63 \pm 11\,\mathrm{eV} \quad , \quad \Gamma = 407 \pm 208 \pm 100\,\mathrm{eV}. \tag{1.5}$$

The result after applying the Deser relation was:

$$a_{K^-p} = (-0.78 \pm 0.15 \pm 0.03) + (0.49 \pm 0.25 \pm 0.12)i\,\mathrm{fm}, \tag{1.6}$$

which is in good agreement with Martin's result. The negative shift was further confirmed by the DEAR Collaboration [7] at the DAΦNE collider with better statistical errors as:

$$\Delta E = -193 \pm 37 \pm 6\,\mathrm{eV} \quad , \quad \Gamma = 249 \pm 111 \pm 30\,\mathrm{eV}, \tag{1.7}$$

although the KpX and DEAR results are slightly different from each other (see Fig. 1.1).

The SIDDHARTA Collaboration, which is the extension of the DEAR Collaboration, is planning to start a very precise measurement of K_α X-ray for kaonic hydrogen and first measurement of K_α X-ray for kaonic deuterium [8], which will enable them to get information on isospin-dependent scattering lengths [9].

Recently, the attempt to understand both the atom data and low-energy scattering data (elastic and inelastic) has been done with the coupled-channel model [10–16]. A result by Cieplý *et al.* is shown as an example in Fig. 1.2. All the calculations show the scattering amplitude for $I = 0$ $\overline{K}N$ is negative at the threshold, and that the sign is changed to positive in the subthreshold region because of the existence of the $\Lambda(1405)$ resonance.

1.1.2 Antikaon-nucleus interaction

Antikaon-nucleus interaction has been studied by fitting experimental data of the shifts and widths of various kinds of kaonic atom levels. The $t\rho$ optical potential is widely used for

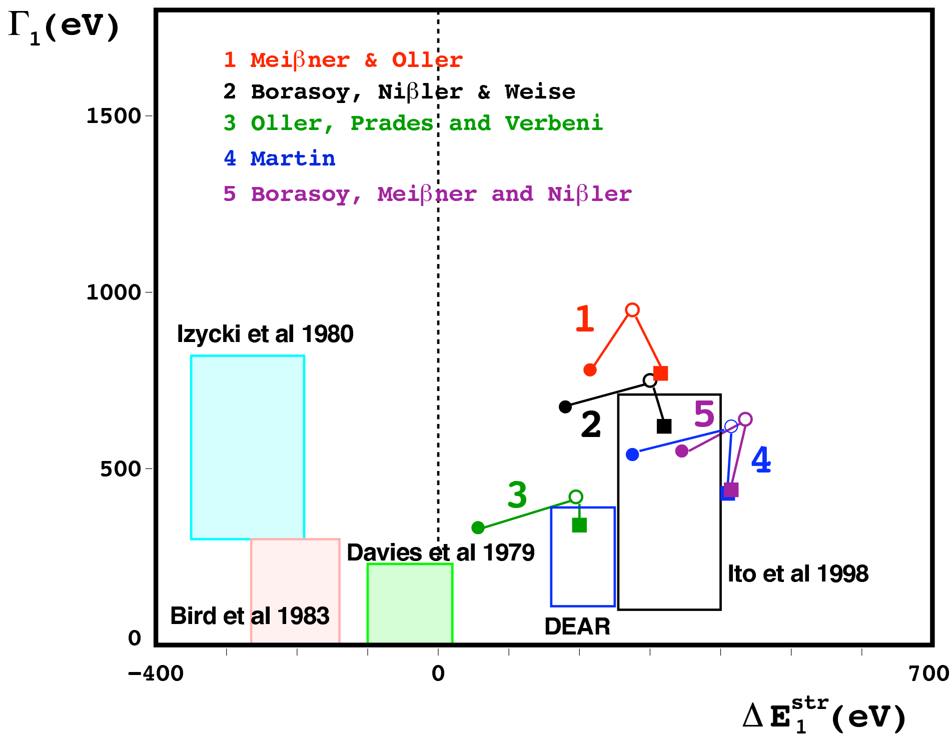

Figure 1.1: Experimental data of the shift and width of kaonic hydrogen, including KpX (Ito *et al.*) and DEAR data. The boundary of each box corresponds to the $\pm 1\sigma$ error. Note that the definitions of $\Delta E_1^{\mathrm{str}}$ and ΔE in the text are sign-inverse. Theoretical calculations with the input for scattering lengths are also shown. Filled circles are the results based on the isospin limit, and empty dots include the effect of the unitary cusp. Filled squares take into account the Coulomb corrections. Taken from [9].

hadron-nucleus interaction. Assuming the isovector component of a nucleus can be negligible, the $t\rho$ potential is described as:

$$2\mu V_{\mathrm{opt}}(r) = -4\pi \left(1 + \frac{A-1}{A}\frac{\mu}{M}\right) b_0 \rho(r), \tag{1.8}$$

where μ is the reduced mass of the kaon and the nucleus, M is the mass of the nucleon and $\rho(r)$ is the nucleon density distribution normalized to the mass number A. A global fit of the available experimental X-ray data results in a so-called “shallow” potential of Re $V(r=0) \sim -80$ MeV [17]. This solution is theoretically supported by chirally motivated coupled-channel approach, which reproduces low-energy K^-p cross sections [10,11,18–24]. A comparison of the calculated shifts and widths with data made by Hirenzaki *et al.* is shown in Fig. 1.3.This approach reproduces the experimental data well.

Meanwhile, one can improve the fit by introducing a density-dependent (DD) potential,

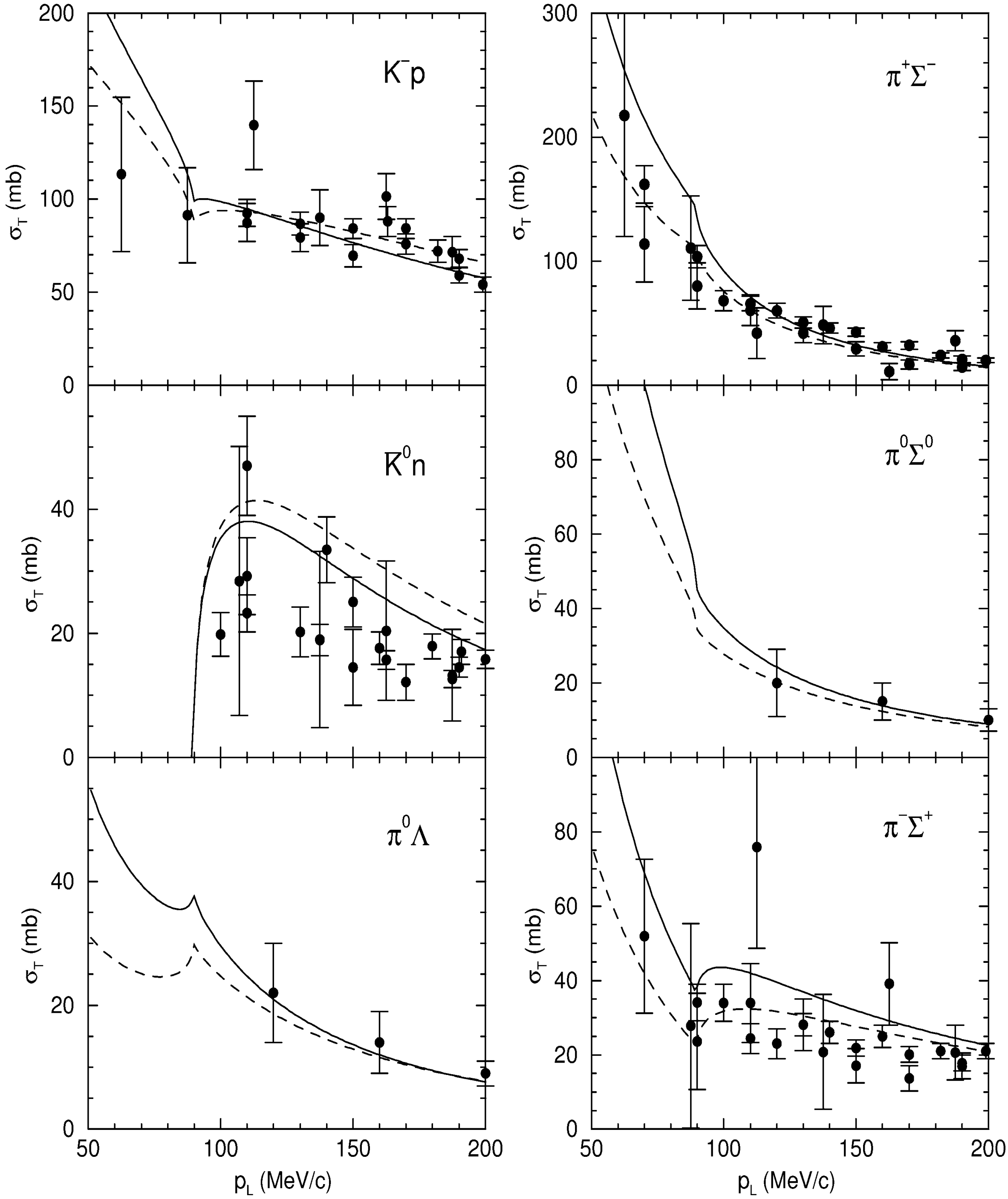

Figure 1.2: Calculations for K^-p scattering and reactions. The dashed lines show free-space chiral-model coupled-channel calculations, and the solid lines show chiral-model coupled-channel calculations with slightly varied parameters in order to fit also K^--atom X-ray data. Taken from [11].

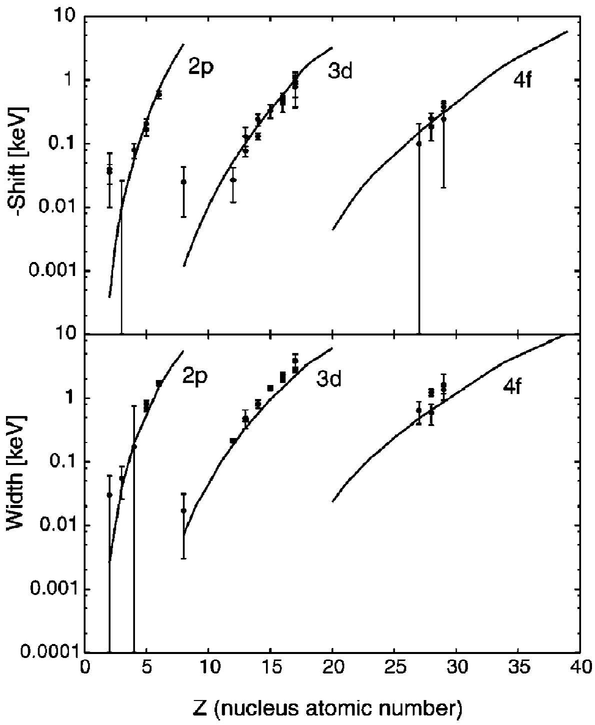

Figure 1.3: Calculated shifts and widths as functions of the nucleus atomic number for $2p$, $3d$, and $4f$ kaonic atoms states. Taken from [22].

substituting b_0 in Eq. (1.8) by $b_0 + B_0[\rho(r)/\rho_0]^{\alpha}$, where b_0, B_0 and $\alpha(> 0)$ are fit parameters. The best fit with this DD potential gives a "deep" potential with Re $V(r = 0) \sim -(150\text{–}200)\,\text{MeV}$ [25–29].

Recently, a different approach starting from $t\rho$ approximation has been suggested [28,29]. A multiplicative function $F(r)$ is introduced so that $F(r) \to 1$ in the internal region and $1 - F(r) \to 1$ in the external region. Thus, the behaviors in the internal and external regions can be connected smoothly, by substituting b_0 in Eq. (1.8) by $B_0F(r) + b_0[1 - F(r)]$, where b_0 and B_0 corresponds to $\overline{K}N$ interaction in the freespace and at the nuclear saturation density, respectively. By using this F potential, a similar deep potential as the DD one is obtained.

A model-independent Fourier-Bessel (FB) method is also applied in [29], where the potential is obtained by adding a FB series to the $t\rho$ potential so as to reduce χ^2. The calculated potential shapes for the four methods shown above ($t\rho$, DD, F, and FB) are compared in Fig. 1.4.

It is still an open question whether the depth of an antikaon-nucleus potential is deep or shallow. The reason of the uncertainty is that the kaonic atom data are sensitive in the low density region of the nucleus because the overlapping of the negative kaon and the nucleus is maximum around the nuclear surface [30].

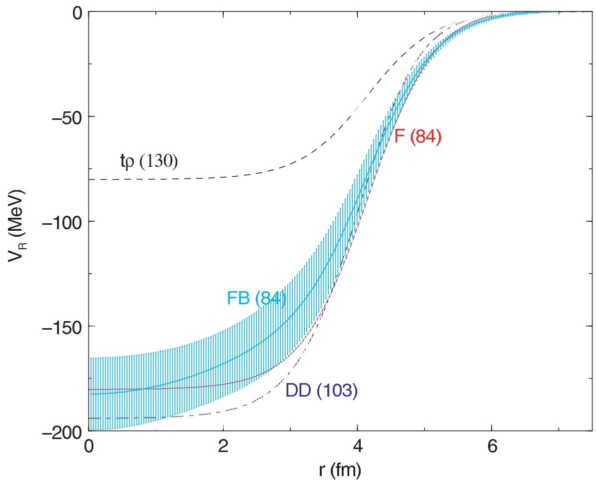

Figure 1.4: Real part of the K^--Ni optical potential for $t\rho$, DD, F, and FB models. The numbers in the parentheses indicate χ^2 for 65 data points. Taken from [29].

An alternative tool to investigate antikaon-nucleus interaction is to study the formation spectrum of the in-flight (K^-, N) reaction. The spectra calculated with a shallow potential (chiral unitary approach) and a deep potential (phenomenological fit) are compared in [31–33]. Experimentally, this reaction was proposed for producing kaon-nucleus bound states [34], and was studied by the BNL-AGS E930 experiment [35,36] and the KEK-PS E548 experiment [37].

1.1.3 Antikaon in nuclear matter

The change of the effective mass of K^- (and K^+) in dense nuclear matter or neutron matter has been investigated with coupled-channel approach [24, 38, 39]. They found the effective mass of K^- decreases as the density increases.It is motivated by the issue of kaon condensation proposed by Kaplan and Nelson [40, 41].

It is not straightforward to confirm these theories by an experiment. The KaoS Collaboration observed the in-medium effect of $K^\pm$ by $p +$ C and $p +$ Au collisions, where kaons are produced in a density near the normal nuclear density but with a finite temperature of several tens MeV [42]. The ratio of the production cross section of K^- over K^+ is enhanced when in-medium $\overline{K}N$ potential is attractive, and the experimental data can be reproduced by a transport model calculation of Boltzmann-Ühling-Uhlenbeck type when an attractive potential of $\sim -80\,\text{MeV}$ is assumed.

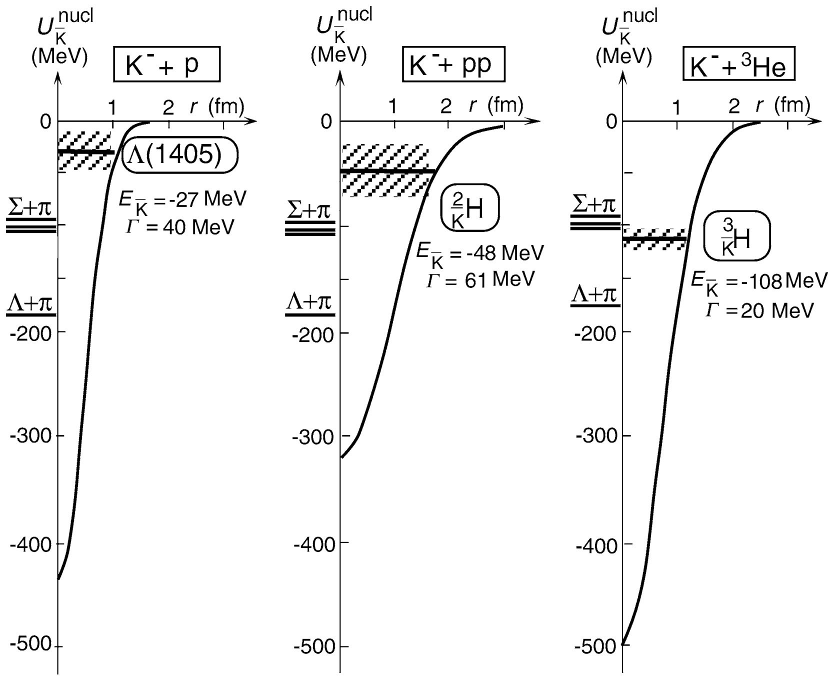

Figure 1.5: $\overline{K}N$ and $\overline{K}$-nucleus potentials for K^-p, K^-pp, and K^-ppn systems. The $\Sigma\pi$ and $\Lambda\pi$ thresholds are also shown. Taken from [46].

1.1.4 Prediction of K^- nuclear states

A possible existence of antikaon bound states with nucleons was pointed out by Nogami [43] for the first time in 1963, when the $\Lambda(1405)$ resonance had been already discovered but its spin and parity had not been determined. He interpreted $\Lambda(1405)$ was a s-wave bound state of $\overline{K}N$ with total spin 1/2, and considered the possibility of the $\overline{K}NN$ bound state. His conclusion was that when the isospin of NN system was 1 and the total isospin was 1/2, the $I = 0$ component of $\overline{K}N$ pairs became the largest and the $\overline{K}NN$ system could be bound below the threshold.

Even if a kaon can be bound deeply inside a nucleus, another question emerges whether the bound state has a narrow decay width enough to be observed experimentally. A possible mechanism of a narrow decay width was suggested by Wycech [44]. If antikaon-nucleus interaction is strongly attractive, the bound state may become so deep ($\sim 100\,\mathrm{MeV}$) that the dominant decay channel $\overline{K}N \to \Sigma\pi$ is closed energetically. Then, the total decay width can be as narrow as $20\,\mathrm{MeV}$.

After a better understanding of $\overline{K}N$ and $\overline{K}A$ interaction was developed in 1990's as shown in previous subsections, Akaishi and Yamazaki quantitatively predicted the existence of nuclear $\overline{K}$ bound states in light nuclei [45]. They constructed a phenomenological $\overline{K}N$

potential, which reproduces the shift and width of the ground state of kaonic hydrogen [5, 6] and Martin's analysis of free $\overline{K}N$ scattering data [1]. They regarded $\Lambda(1405)$ as a bound state of $\overline{K}N$ with isospin 0, and the binding energy and decay width can be reproduced by their potential.

They showed that the ${}^{3}_{K}\mathrm{H}$ $(= K^- \otimes {}^3\mathrm{He} + \overline{K}^0 \otimes {}^3\mathrm{H})$ $[K^- ppn]$ state with isospin 0 has a large binding energy of 108 MeV from the $K^- + {}^3\mathrm{He}$ threshold, as shown in Fig. 1.5. The decay width becomes as narrow as 20 MeV, because the state lies below the $\Sigma + \pi$ decay threshold. The shrinkage of the core nucleus is taken into account, and it increases the total binding energy further, overcoming the core excitation. They proposed to utilize the ${}^4\mathrm{He}(K^-_{\mathrm{stop}}, n)$ reaction to produce $K^- ppn$ states. They also proposed the (K^-, π^-) reaction to produce proton-rich systems via Λ^* doorways [46]. A proton-rich system may be deeply bound with the aid of the strong attraction between a K^- and a proton.

Because of the extremely strong attraction of $I = 0$ $\overline{K}N$ pairs compared with $I = 1$ pairs, the implantation of a single antikaon is expected to deform the nuclear structure. Antisymmetrized molecular dynamics (AMD), which does not require any assumption on the structure of the system, was applied for kaonic nuclei [47, 48]. They found the central density can reach 10 times as large as the normal nuclear density.

On the other hand, there is a criticism against the Akaishi-Yamazaki prediction [49]. One of the main problems discussed in the paper is about the $\overline{K}A$ potential as described in the previous subsection; a "shallow" potential results in a kaon bound state with smaller binding energy and much broader decay width. Moreover, according to the chiral approach, $\Lambda(1405)$ is a superposition of two resonances [50, 51], in contrast to the assumption of a $\overline{K}N$ bound state by Akaishi and Yamazaki. In addition, the drastic increase of two-body absorption such as $K^- NN \to N\Lambda$, $N\Sigma$ for a kaonic nuclear state with extremely high density was pointed out.

It is an open question whether a kaonic nuclear state in a light nucleus exists and it has a decay width narrow enough to be observed experimentally. This question is strongly related with the strength of antikaon-nucleus interaction.

1.1.5 Previous experimental search

KEK-PS E471 and E549 experiment

Iwasaki *et al.* performed a missing-mass spectroscopy experiment (KEK-PS E471) with the (K^-_{stop}, n) reaction using a liquid helium-4 target [52], motivated by the prediction by Akaishi and Yamazaki [45]. Because of the necessity to reconstruct the stopping vertex of kaons, they required one charged particle (p or $\pi^{\pm}$) from the vertex to be detected. Unexpectedly, they observed a distinct peak in the semi-inclusive proton spectrum. It corresponded to a neutral tribaryon system with the mass $3117.0^{+1.5}_{-4.4}\,\mathrm{MeV}/c^2$ and the width less than $21\,\mathrm{MeV}/c^2$ [53].

Assuming the state to be a kaon bound state of K^-pnn, the binding energy from the $K^- + p + n + n$ threshold is about 193 MeV. They also claimed an indication of another peak in the semi-inclusive neutron spectrum, which may correspond to K^-ppn states with the binding energy of about 169 MeV [54, 55].

The observed states were much more deeply bound than the first prediction for K^-ppn states (118 MeV from the $K^-+p+p+n$ threshold) by Akaishi and Yamazaki [45]. Surprisingly, the total isospin $I = 1$ states (K^-pnn) lie lower than the $I = 0$ states (K^-ppn), contrary to their theoretical prediction. Theoretical improvements from the first prediction in order to explain the more binding and inverse the two levels were discussed in [56].

On the experimental side, an upgraded experiment (KEK-PS E549) was carried out with improved neutron detection efficiency and time-of-flight resolution. In order to investigate the inclusive ($K^-_{\rm stop}$, p) spectrum, the trigger condition was also modified. A pair of TOF counters and drift chambers for emitted protons was installed. However, the observed inclusive proton spectrum didn't show any significant narrow peak structure. As for a narrow ($<$ 40MeV) tribaryon state, a formation rate as large as 1% per stopped K^- has been excluded [57]. The reason for the discrepancy between the two experiments was explained in [58]; a small displacement after the slewing correction for TOF counters could deform the proton spectrum. A proton around the peak momentum looses almost all of its kinetic energy in the TOF counters, and the empirical formula for the slewing correction may not be very precise for large energy deposits.

The analysis for the neutron spectrum is on-going [59].

Meanwhile, they reported the correlation of Λd pairs, whose invariant mass distributes close to the threshold of $m_{^4\mathrm{He}} + m_{K^-} - m_n$ [60]. They interpreted it as evidence of a three-nucleon absorption process. A similar correlation was observed by the FINUDA Collaboration, for ^{6}Li target [61], but a different interpretation of a K^-ppn bound state with small binding energy was suggested.

BNL-AGS E930 and KEK-PS E548 experiment

The in-flight (K^-, n) reaction was applied for the first time by Kishimoto *et al.* as a parasite experiment of the BNL-AGS E930 experiment, which was to measure γ rays from $^{16}_{\Lambda}$O hypernuclei with the (K^-, $\pi^-\gamma$) reaction ($p_{K^-} = 930\,\mathrm{MeV}/c$) [35, 36]. The beam momentum was suitable for the (K^-, n) reaction because the elastic scattering has the maximum cross section there. They reported two bump structures at $B_{K^-} = 130$ and 90 MeV.

They continued to study both the (K^-, n) and (K^-, p) reactions for ^{12}C and ^{16}O targets at KEK-PS [37]. The measured missing mass spectrum indicates that $\overline{K}$-nuclear interaction is strongly attractive. The depth of the potential, around -190 MeV for the ^{12}C(K^-, n) reaction and -160 MeV for the ^{12}C(K^-, p) reaction, was obtained by fitting with a spectrum calculated with the Green's function method. The difference was interpreted as the different number of $\overline{K}N$ pairs with isospin 0 in the K^--nucleus systems produced in the two reactions.

GSI-FOPI experiment

Heavy ion collision of Ni + Ni at $1.93A$ GeV was studied at GSI-FOPI experiment. The invariant mass distribution of Λd, which corresponds to a $K^- ppn$ system, had an excess over a combinatorial background around $3.16\,\mathrm{GeV}/c^2$ [62].

Theoretically, a possibility to produce single-$\overline{K}$ or double-$\overline{K}$ nuclear clusters in heavy ion collisions had been pointed out in [63]. In the model, an antikaon (or Λ^*) produced in a collision traps nucleons and forms a cluster. The invariant mass spectroscopy can be performed by detecting all the decay particles from the cluster.

CERN-OBELIX experiment

The OBELIX experiment, which studied antiproton annihilation on ^{4}He at rest, reported Λp and Λd narrow peak structures, in the $p\pi^- p$ and $p\pi^- d$ invariant mass spectra [64]. While Λ or K^0_S cannot be identified directly in the invariant mass spectrum of its decay particles ($p\pi^-$ or $\pi^+\pi^-$) because of a poor resolution and a huge combinatorial background, they claimed the data showed the backward correlation between Λ and proton, and between (Λp)-system and K^0_S.

1.1.6 Search for deeply-bound kaonic nuclei in FINUDA experiment

The FINUDA (acronym for "FIsica NUcleare a DAΦNE") experiment investigates deeply-bound kaonic nuclei in the stopped K^- absorption reactions with both missing-mass spectroscopy and invariant-mass spectroscopy.

Missing-mass spectroscopy

As in the KEK-PS E471/E549 experiment, the missing-mass spectroscopy can be applied in the FINUDA experiment. Inclusive neutron and proton spectra will be obtained. Moreover, the FINUDA spectrometer has an advantage of a large acceptance, which allows to tag decay particle(s) of deeply-bound kaonic nuclei such as a hyperon. This would improve the signal-to-noise ratio in the inclusive missing mass spectra.

In the first data taking, a narrow peak around $500\,\mathrm{MeV}/c$ was observed in the proton spectrum from ^{6}Li target [65]. It was found that the proton was strongly correlated with a fast π^- in a backward direction, which was considered to originate from Σ^- decay. This means that an almost monochromatic proton comes from the quasi-deuteron absorption process:

$$K^- + \text{“}d\text{”} \rightarrow \Sigma^- + p, \tag{1.9}$$

where the "d" corresponds to a quasi-deuteron in a $\alpha + d$ cluster of ^{6}Li.

If the decay width of the state (if exists) is large, it is not easy to search for a deeply-bound kaonic state via missing-mass spectroscopy. The decay width strongly depends on the coupling strength to the main decay channel of $\Sigma\pi$. In addition, non-mesonic decay would enhance the decay width.

Moreover, in two-nucleon and multi-nucleon absorption processes, a nucleon and a hyperon are emitted. Therefore, it is hard to distinguish the formation of deeply-bound kaonic nuclei from these absorption processes, even with tagging the hyperons.

Invariant-mass spectroscopy

If all the decay particles emitted from a kaon bound state could be detected, the invariant mass is obtained. In particular, two-body decay modes such as:

$$K^- pp \to \Lambda + p, \tag{1.10}$$

$$K^- ppn \to \Lambda + d, \tag{1.11}$$

$$K^- ppnn \to \Lambda + t, \tag{1.12}$$

are considered to be clean channels because the decay particles in the final state will be emitted in back-to-back.

So far, in the FINUDA experiment we observed both Λp pairs [66] (discussed in Sec. 1.3) and Λd pairs [61] in back-to-back correlation.

1.2 Stopped K^- absorption

The absorption of a negative kaon from an atomic orbit onto a nucleus had been intensely investigated with the bubble chamber and nuclear emulsion technique [67, 68]. A kaon is principally absorbed by one nucleon at the nuclear surface, and a pair of a hyperon and a pion is emitted:

$$K^- + \text{“}N\text{”} \to Y + \pi, \tag{1.13}$$

where N and Y denotes a nucleon and a hyperon (Λ or Σ), respectively. For accuracy, a nucleon bound in a nucleus is written as "N" in distinction from a free nucleon.

The interests at that time were mainly focused on this one nucleon absorption process, in order to extract information on $\overline{K}N$ interaction at subthreshold. The proton/neutron density distribution near the nuclear surface could be also studied, because the kaon absorption by proton and neutron can be discriminated by detecting the final state particles in principle.

Katz *et al.* [67] studied the branching ratio of each absorption process in ^{4}He in detail (Table 1.1). They reported non-pionic final states account for $16.5 \pm 2.6\%$ per stopped K^-.

Table 1.1: Branching ratios for K^- absorption for ^{4}He. Taken from [67].

Reaction	Events/(stopping K^-) (%)
$K^-He^4 \to \Sigma^+\pi^-H^3$	9.3 ± 2.3
$\to \Sigma^+\pi^- dn$	1.9 ± 0.7
$\to \Sigma^+\pi^- pnn$	1.6 ± 0.6
$\to \Sigma^+\pi^0\, nnn$	3.2 ± 1.0
$\to \Sigma^+\quad nnn$	1.0 ± 0.4
Total $\Sigma^+ = (17.0\pm2.7)\%$	
$K^-He^4 \to \Sigma^-\pi^+H^3$	4.2 ± 1.2
$\to \Sigma^-\pi^+ dn$	1.6 ± 0.6
$\to \Sigma^-\pi^+ pnn$	1.4 ± 0.5
$\to \Sigma^-\pi^0\, He^3$	1.0 ± 0.5
$\to \Sigma^-\pi^0\, pd$	1.0 ± 0.5
$\to \Sigma^-\pi^0\, ppn$	1.0 ± 0.4
$\to \Sigma^-\quad pd$	1.6 ± 0.6
$\to \Sigma^-\quad ppn$	2.0 ± 0.7
Total $\Sigma^- = (13.8\pm1.8)\%$	
$K^-He^4 \to \pi^-\Lambda\ He^3$	11.2 ± 2.7
$\to \pi^-\Lambda\ pd$	10.9 ± 2.6
$\to \pi^-\Lambda\ ppn$	9.5 ± 2.4
$\to \pi^-\Sigma^0\, He^3$	0.9 ± 0.6
$\to \pi^-\Sigma^0\ (pd,ppn)$	0.3 ± 0.3
$\to \pi^0\Lambda\ (\Sigma^0)(pnn)$	22.5 ± 4.2
$\to \Lambda\ (\Sigma^0)\ (pnn)$	11.7 ± 2.4
$\to \pi^+\Lambda\ (\Sigma^0)nnn$	2.1 ± 0.7
Total $\Lambda\ (\Sigma^0) = (69.2\pm6.6)\%$	
Total $= \Lambda+\Sigma = (100_{-7}^{+0})\%$	

This non-pionic absorption must involve at least two nucleons, such as,

$$K^- + \text{“}NN\text{”} \to Y + N. \tag{1.14}$$

The total multi-nucleonic absorption rate was obtained for various kinds of nuclei by subtracting the contribution of pionic absorption, as summarized in Table 1.2. Except for deuterium target (only 1%), it is as large as $\sim 20\%$, almost independent of the mass number. Although various interpretations to this behavior were reviewed in [69], the mechanism of the multi-nucleon absorption process is still not well-understood.

Experimentally, the bubble chamber or emulsion can detect only charged particles. Neutral particles, such as γ's (from Σ^0 or π^0 decay) and neutrons, are not detected. Thus, the $\Lambda\pi^0$ events in the reaction (1.13) can not be distinguished from the Λn events in the reaction (1.14) as well as the $\Sigma^0 n$ events. Furthermore, some secondary effects such as pion absorption in the same nucleus after the one-nucleon kaon absorption might contribute to the multi-nucleon kaon absorption processes. Therefore, we need theoretical assistance to completely sort out the events originated from the reaction (1.13) and reaction (1.14).

An exclusive detection of a pair of hyperon and nucleon would give a direct information on two-nucleon absorption. However, the final state with only charged particles, such as $\Lambda + p \to (p + \pi^-) + p$, could be investigated in old experiments. For example, Davis *et al.* mentioned in their paper [70],

Table 1.2: Branching ratios for multi-nucleon absorption for various media. Taken from [68].

D	He	C
~ 0.01	0.16 ± 0.03	$0.19 \pm 0.02 \pm 0.03$

Ne	CF_3Br-C_3H_8	CF_3Br
0.23 ± 0.03	0.26 ± 0.03	~ 0.26

> "It is found that the sum of the energies of the Λ^0 and a single proton rarely approaches the energy release appropriate to an interaction of the K^- on two nucleons."

Their finding was reconfirmed by the FINUDA experiment as described in the next section. Unfortunately, there was no further information about this mode in the paper.

Except for helium, detail decay branching ratios of multi-nucleon absorptions are not available and only the total non-pionic absorption rate has been obtained as a contribution distinguished from the pionic absorption. An exclusive measurement of a final state will give a new information on multi-nucleon absorption.

1.2.1 π^- two-nucleon absorption at rest

It would be instructive to review the π^- two-nucleon absorption at rest for reference. They are similar in that a negative meson in an atomic orbit is absorbed by two correlated nucleons, and two particles are emitted in back-to-back.

In case of π^- absorption, the conservation law of energy and momentum forbids one-nucleon absorption. Therefore, a negative pion is absorbed by at least two nucleons. Here, the most dominant process of two-nucleon absorption:

$$\pi^- + \text{“}pn\text{”} \rightarrow n + n, \tag{1.15}$$

$$\pi^- + \text{“}pp\text{”} \rightarrow n + p, \tag{1.16}$$

is considered.

The first observation indicating two-nucleon absorption was reported by Ozaki *et al.* [71], by a coincidence measurement of outgoing nn pairs and np pairs with large kinetic energy. Before then, there had been only single-particle measurements, and the picture of two-nucleon absorption had not been established, although it had been realized that the kinetic energy corresponding to the pion mass was shared only by a few nucleons. For example, an α-absorption mechanism had been also suggested.

Later, Bassalleck *et al.* carried out a series of coincidence measurements of two neutrons for various kinds of p-shell nuclei [72–76]. In these papers, the excitation energy spectrum of the residual nucleus for each target was obtained in a good energy resolution. Depending on the transition strength, some specific states with favored ΔT (isospin) and ΔL (angular momentum) were selectively populated. Especially, $\Delta T = 0$ transitions, which mean the absorption by quasi-free deuteron, were predominantly observed.

As for pp-absorption, the coincidence measurement of $n + p$ and $n + n$ was studied by Heusi *et al.* for ^{6}Li, ^{7}Li, ^{12}C, and heavier nuclear targets [77]. For ^{6}Li target (Fig. 1.6, taken from [77]), the spectrum for back-to-back neutron-neutron pairs showed an enhancement between 118 and 153 MeV of the sum energy, which was attributed to the quasi-free absorption by a neutron-proton pair in the p-shell (p-shell absorption). Another small enhancement was seen between 82 and 118 MeV, and it can be interpreted as the absorption by two nucleons of which at least one nucleon is in the s-shell. Note that the absorption by two nucleons, one from the s-shell and the other from the p-shell, is expected to be suppressed, according to a calculation by Golovanova and Zelenskaya [78]. With the same reason, the neutron-proton pairs must comes from the pp pair absorption in s-shell, because a ^{6}Li nucleus has only one proton in the p-shell. The corresponding energy region is shown in the figure, but it doesn't show any clear enhancement. The energy spectrum of the proton seemed to indicate a contamination of secondary particles after pn-absorption.

To the contrary, the absorption in^{12}C target, which has four neutrons and protons in the p-shell, showed much different behaviors (Fig. 1.7, taken from [77]). The neutron-neutron pairs are mainly from the p-shell absorption, which is indicated by the two lines in the left figure. Similarly, the neutron-proton pairs have an enhancement in the p-shell absorption region. This fact suggests that the quasi-free absorption by two protons in p-shell may be also observed for π^- absorption in other p-shell nuclei, except for Li in which p-shell absorption is not possible.

From a theoretical point of view, the contribution of single-nucleon absorption with two-nucleon correlation is too small to explain the reaction strength of two-nucleon absorption, and a second order term of the rescattering process with an intermediate Δ was proposed. One of theoretical interests was to reproduce an experimental observable, the ratio of $\Gamma(nn)$ over $\Gamma(np)$, where Γ denotes a partial reaction rate. Experimental results showed around 3–6, while theoretical calculations gave somewhat larger values. For instance, Shimizu and Faessler [79] calculated s- and p-wave absorption in nuclear matter and the results were 9.3 for s-wave, 8.5 ($\pi + \rho$ exchange) and 15.0 ($\pi + \rho + 2\pi$ exchange) for p-wave. The difference between experiment and theory may be due to some final state interaction.

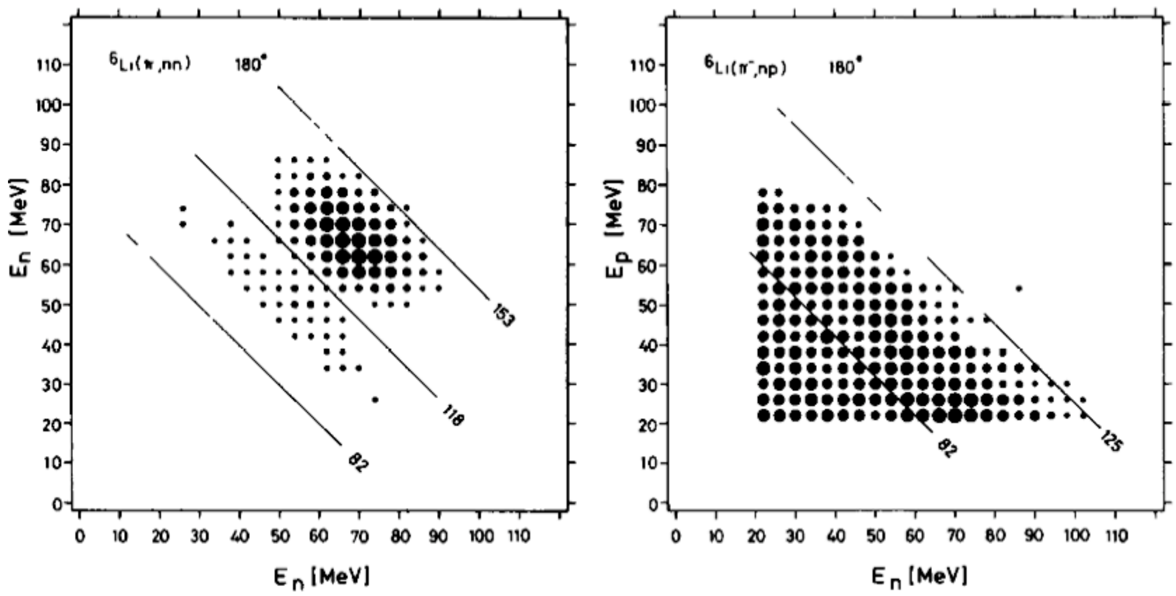

Figure 1.6: Two-dimensional energy spectra of neutron-neutron (left) and neutron-proton (right) pairs for ^{6}Li target. Taken from Fig. 4 in [77].

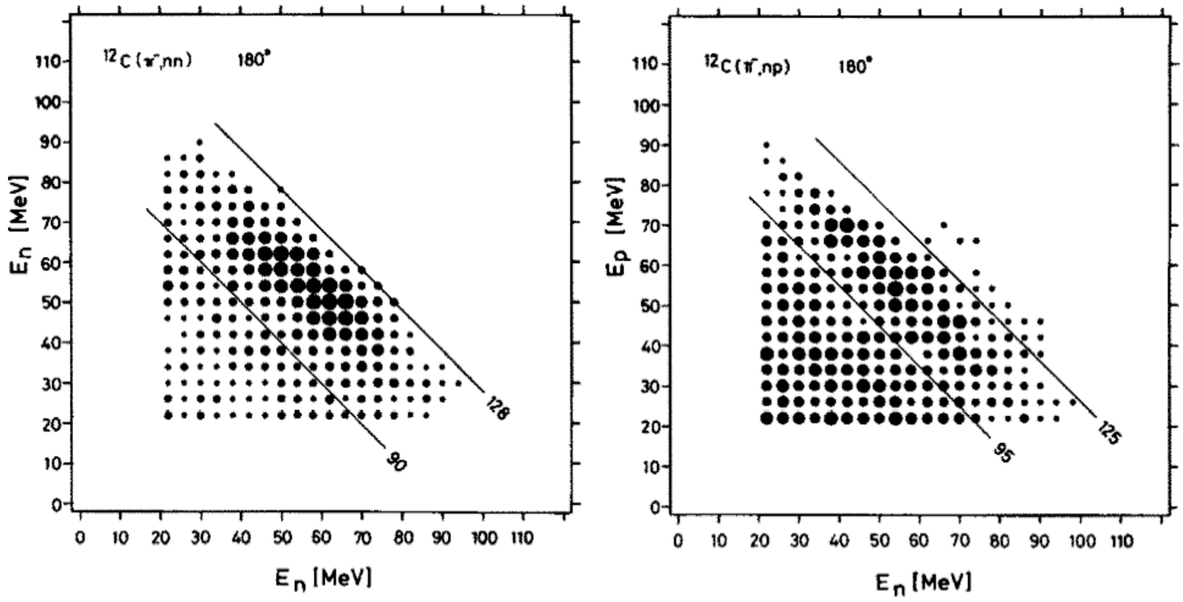

Figure 1.7: Two-dimensional energy spectra of neutron-neutron (left) and neutron-proton (right) pairs for ^{12}C target. Taken from Fig. 12 in [77].

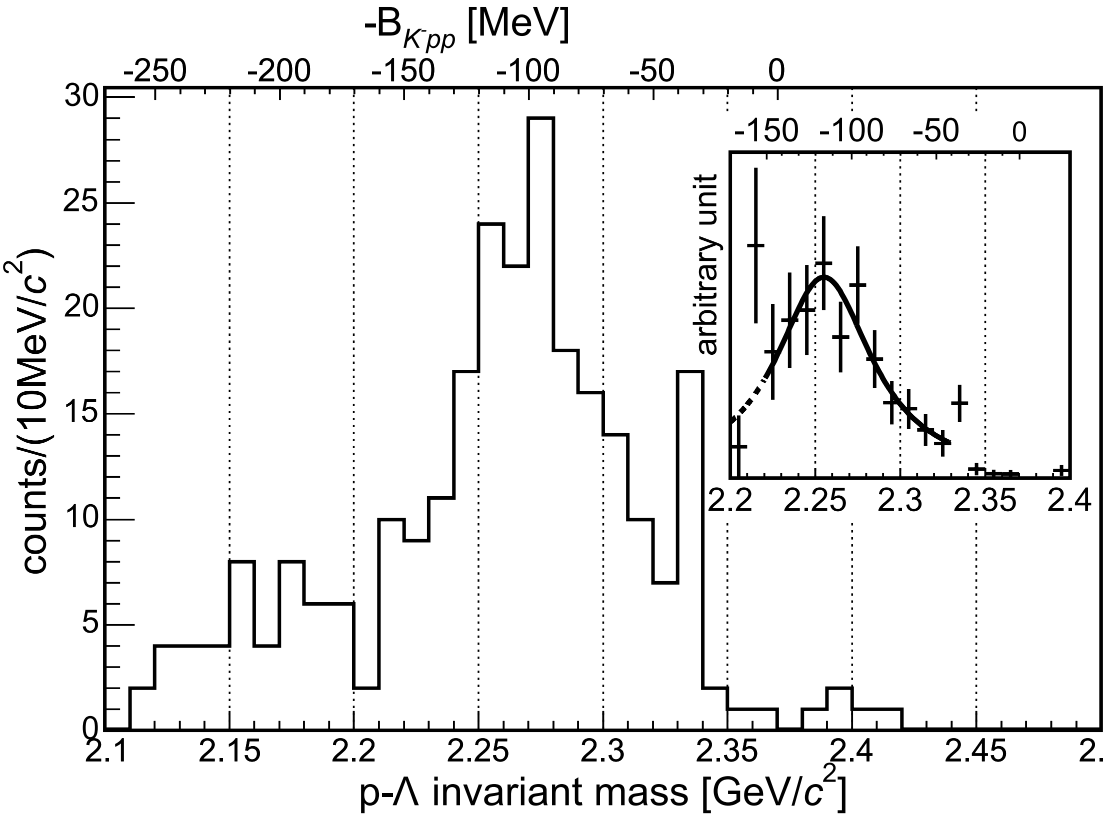

Figure 1.8: Invariant mass of a Λ and a proton in back-to-back from light targets before the acceptance correction. The inset shows the result after the acceptance correction. Taken from [66].

1.3 Observation of K^-pp system in the first FINUDA data taking

In the first data taking of the FINUDA experiment, we took the data of the stopped K^- absorption reactions on five kinds of targets: ^{6}Li, ^{7}Li, ^{12}C, ^{27}Al, and ^{51}V. From the analysis of the events in which a Λ hyperon and a proton were in the final state, we reported the invariant mass distribution of back-to-back Λ and proton pairs for light nuclei (^{6}Li, ^{7}Li, and ^{12}C) in 2005 [66]. A pair of Λ and proton is expected to originate from the kaon absorption by two protons inside a nucleus, but their invariant mass had a large deficit from the sum of the mass of a kaon and two protons ($2.370\,\mathrm{GeV}/c^2$), as shown in Fig. 1.8. It conflicts with a naïve expectation that it should distribute slightly below the threshold due to the binding of the two protons, if the pair comes from so-called two-nucleon absorption ($K^- +$ "pp" $\rightarrow \Lambda + p$). In Ref. [66], some possible interpretations to explain the observed distribution, assuming the existence of two-nucleon absorption process, were discussed. However, none of them can explain the invariant mass spectrum and the observed angular correlation simultaneously. Then, an interpretation, that a deeply-bound state of K^-pp from the $K^- + p + p$ threshold was produced after kaon absorption and it decays into $\Lambda + p$, was considered. Assuming that the Λp pair comes from the decay of a K^-pp subsystem in a free space and the decay particles do not suffer final state interaction, the binding energy (B) and decay width (Γ) were obtained as:

$$B = 115^{+6}_{-5}(\text{stat})^{+3}_{-4}(\text{syst})\,\text{MeV} \quad \text{and} \quad \Gamma = 67^{+14}_{-11}(\text{stat})^{+2}_{-3}(\text{syst})\,\text{MeV}, \tag{1.17}$$

from a global fit on the invariant mass distribution with a Lorentzian function.

The important statements in the paper are two-folded as follows.

First observation of Λp pairs in stopped K^- absorption

As described in the previous section, one-nucleon absorption, which emits a hyperon and a pion in a low momentum, had been intensively studied in 1960's and 1970's. It was also noticed that there were significant amount of hyperons which do not associate any pions. However, a detailed discussion on multi-nucleon absorption processes was difficult due to the limited experimental information. One of non-pionic absorption modes of Λp pairs was directly observed with a good momentum resolution for the first time, thanks to the large acceptance of the FINUDA spectrometer.

Assignment of back-to-back Λp pairs to K^-pp decay

We attributed the decrease of the invariant mass from the threshold to the binding of K^- into two protons, and we assumed the existence of K^-pp bound states. However, the obtained binding energy was much larger than a theoretical prediction (48 MeV) by Yamazaki and Akaishi in 2002 [46]. Also, the decay width was moderately large although the binding energy was close to the main decay threshold of $\Sigma\pi$ channel (see Fig. 1.5). There were no other theoretical calculations, and our interpretation seemed to somewhat deviatefrom the only one theoretical calculation at that time.

The invariant mass distributions of the Λp pairs did not exhibit the contribution from "quasi-free" two-nucleon absorption. Here, a quasi-free absorption process is defined as an absorption process with two nucleons, picked up from the nucleus without breaking up the residual. This process is similar to the absorption with two nucleons in a free space except for small effects due to the Fermi motion and the binding energy of the two nucleons. A "deeply-bound" K^-pp state can not be formed with such a quasi-free process, because the energy transfer of around 100 MeV, corresponding to the binding energy of K^-, is so large that the residual nucleus must be involved in the formation process.

In this respect, there was a criticism; "Why there were no quasi-free two-nucleon absorption observed in the FINUDA experiment ?" It is based on a prejudice that the large fraction of $\sim 20\%$ per stopped kaons for non-mesonic absorptions must come from the "quasi-free" two-nucleon absorption as naively expected. However, it should be noted that nobody had ever kinematically identified the two-nucleon absorption and the absorption on pp pairs was not the only absorption mode of two-nucleon absorptions. Nevertheless, such a model calculation to interpret the observed Λp pairs as a secondary product of the quasi-free two-nucleon absorption was carried out [80]. In the model, the invariant mass distribution of the Λp pairs is modified to a low mass side from the original near-threshold region and broadened because of the rescattering of Λ or proton with the residual nucleus.

Two interpretations, the decay of K^-pp bound states and quasi-free two-nucleon absorption followed by secondary processes, could explain the observed invariant mass distribution reasonably.The difference between two interpretations would be prominent in the angular correlations between the Λ and proton. The interpretation based on the rescattering should have a large mass-number dependence of the angular correlations, broadened for heavy systems.

Here, it should be noted that the rescattering interpretation predicts the quasi-free two-nucleon absorption should not be observed in Li, C and heavier targets because of the strong rescattering. While, the existence of K^-pp does not exclude the existence of the quasi-free two-nucleon absorption in other absorption modes.

1.4 Motivation

It is known that the kaon absorption can occur with pn pairs as well as pp pairs.

If the observed Λp pairs are really from the decay of K^-pp bound states, kaon absorption on a pn pair is expected to result in a different distribution. This is because the strong binding of a $\overline{K}NN$ system is expected only for K^-pp, but not for K^-d. In the FINUDA experiment, two kinds of final states of Λn and Σ^-p pairs from the pn-absorption can be investigated. They would be observed as quasi-free two-nucleon absorption processes.

On the other hand, based on the other interpretation of secondary processes for the observed Λp pairs, this would be also the case for Λn and Σ^-p pairs from quasi-free two-nucleon absorption. For example, the distributions of Λp and Λn pairs were expected to be similar because the effect of final state interaction for proton and neutron would be almost the same. Therefore, the quasi-free component is expected to be suppressed in observed distributions of Λn and Σ^-p pairs as well as the Λp pairs, according to this interpretation.

In order to discriminate the two interpretations for and against the K^-pp bound states, it would be a key feature whether quasi-free components are observed for the Λn and Σ^-p pairs. However, the low detection efficiency of neutrons in the FINUDA experiment did not allow such analyses with the limited statistics in the first data taking.

The target dependence of the invariant mass distribution and the angular correlation of the Λp pairs will provide another information; the published spectrum was the sum for three different nuclei. If the rescattering interpretation is true, the invariant mass distributions and the opening angle distributions should strongly depend on the targets. In contrast, a target dependence inferred in the interpretation of K^-pp should be small. Thus, it is desired that the target-by-target results be compared with each of interpretations. Unfortunately, we could not show the invariant mass distributions target by target with the limited statistics in the first data taking.

Therefore, we decided to have the second data taking with light targets of ^{6}Li, ^{7}Li, ^{9}Be, ^{13}C, and D_2O with ~ 5 times more beam luminosity supplied. It would enable us to present invariant mass distributions and opening angle distributions for Λp target by target, and the comparison among them would be possible. If final state interaction changes the invariant mass distribution, its shape might be different from lithium to oxygen. Furthermore, a detailed analysis of Λn and $\Sigma^- p$ would be possible with much higher statistics. It would give us a key to investigate whether the quasi-free two-nucleon absorption process occurs for Λn or $\Sigma^- p$ pairs.

Through the analysis of three kinds of final state (Λp, Λn and $\Sigma^- p$) for each target, the origin of Λp pairs far below the threshold will be investigated.

1.5 Thesis composition

The detail of the FINUDA experiment is described in Chapter 2. The analysis of a single particle and a hyperon is shown in Chapter 3. The correlation between a hyperon and a nucleon is depicted as a result in Chapter 4. Based on the result, several interpretations of the observed correlations are discussed in Chapter 5. The conclusion is given in Chapter 6.

Chapter 2

FINUDA experiment

The FINUDA experiment [81–83] is a unique experiment which has two good features of a *collider experiment* and a *fixed target experiment* in common. The experiment has been performed at a ϕ-factory DAΦNE (acronym for "Double Annular ϕ-factory for Nice Experiments") in LNF-INFN, Italy. The uniqueness of DAΦNE is that the abundantly produced ϕ mesons in the e^+e^- collisions are used for the source of secondary mesons, such as $K^\pm$, K_S^0 and K_L^0. In case of the FINUDA experiment, the secondary charged kaons are stopped inside thin fixed targets surrounding the DAΦNE beampipe. Various nuclear reactions after the absorption of stopped K^- in a nucleus have been studied.

2.1 Physics program

The FINUDA experiment has two main physics programs; hypernuclear physics and searches for deeply-bound kaonic nuclei. Two kinds of spectroscopy, missing-mass spectroscopy and invariant-mass spectroscopy, as already discussed in Sec. 1.1.6, are applied in searching for deeply-bound kaonic nuclei.

2.1.1 First data taking

The first data taking was carried out from October 2003 to March 2004. In this data taking, five kinds of nuclear targets ($2\times{}^6$Li, $1\times{}^7$Li, $3\times{}^{12}$C, $1\times{}^{27}$Al, $1\times{}^{51}$V) were selected, mainly for hypernuclear spectroscopy. We collected a total integrated luminosity of $250\,\mathrm{pb}^{-1}$, of which $33\,\mathrm{pb}^{-1}$ were used for the DAΦNE tuning, and $10\,\mathrm{pb}^{-1}$ were used for debugging the FINUDA detector system.

2.1.2 Second data taking

In the first data taking, we needed to analyze the Λp events from light nuclear targets in order to avoid the possible final state interactions for heavier nuclei. Thus, we decided to put a different set of p-shell nuclear targets ($2 \times {}^{6}$Li, $2 \times {}^{7}$Li, $2 \times {}^{9}$Be, $1 \times {}^{13}$C, $1 \times$ D_2O), for the second data taking.

In order to improve the statistics, the total luminosity of 966 pb^{-1} was accumulated from October 2006 to June 2007, especially for non-mesonic weak decays of hypernuclei and for deeply-bound kaonic nuclei. Thanks to the experience in the previous data taking, a stable operation enabled us to obtain 5 times or more statistics in total. In this thesis, the data set in the second data taking is analyzed.

2.2 The DAΦNE collider

The DAΦNE facility is an electron-positron collider with $\sqrt{s} = 1020$ MeV, corresponding to the ϕ meson mass.

As shown in Figs. 2.1 and 2.2, two main rings for electrons and positrons, injected from a LINAC, has two crossing points. The FINUDA spectrometer and KLOE spectrometer are located in the opposite sides of the crossing points. For the second data taking, the crossing angle (half of the angle between beams) is 25 mrad, which causes a small boost in the outward direction of the main ring.

The main decay modes of a ϕ meson are [84],

$$\begin{aligned} \phi &\to K^+\ K^- && (\text{B.R.} = 49.3 \pm 0.6\%), && (2.1)\\ &\to K_L^0\ K_S^0 && (\text{B.R.} = 34.0 \pm 0.5\%), && (2.2)\\ &\to \pi^+\pi^-\pi^0\ (\rho\pi) && (\text{B.R.} = 15.23 \pm 0.35\%). && (2.3) \end{aligned}$$

The decay product of $K^{\pm}$ and K_L^0, K_S^0 are used for various particle and nuclear physics experiments. In the KLOE experiment K_L^0, K_S^0 and K^+ are used to measure their decay branching ratio. On the other hand, a negative kaon with initial kinetic energy of about 16 MeV is used in the FINUDA experiment. It knocks out an electron in an atom when it stops to form a kaonic atom. The kaonic atom deexcites by emitting X-rays until a kaon is absorbed by the nucleus due to strong interaction. The DEAR experiment measured this atomic X-ray of kaonic hydrogen at DAΦNE. The SIDDHARTA experiment is further planned to measure the X-ray transitions of kaonic atoms (hydrogen and deuterium) with newly developed silicon drift detectors.

The production rate of ϕ mesons is 440 Hz at the luminosity of $10^{32}/\text{cm}^2/\text{s}$ (equal to 8.64 pb^{-1}/day), corresponding to ~ 220 Hz for K^+K^- pairs. Figure 2.3 is a summary of the delivered luminosity in the second data taking from October 2006 to June 2007.

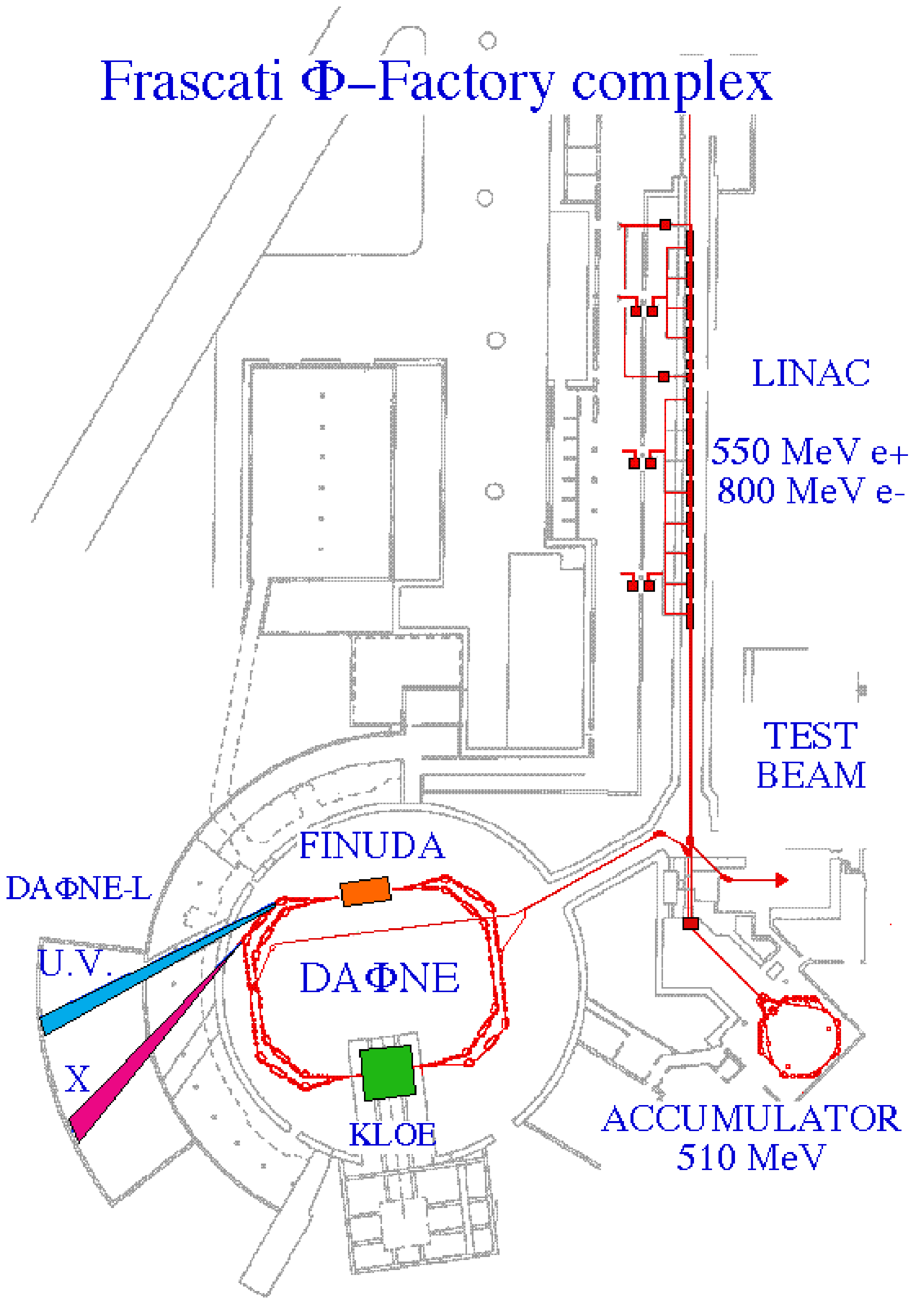

Figure 2.1: Schematic layout of the DAΦNE accelerator complex. Taken from [85].

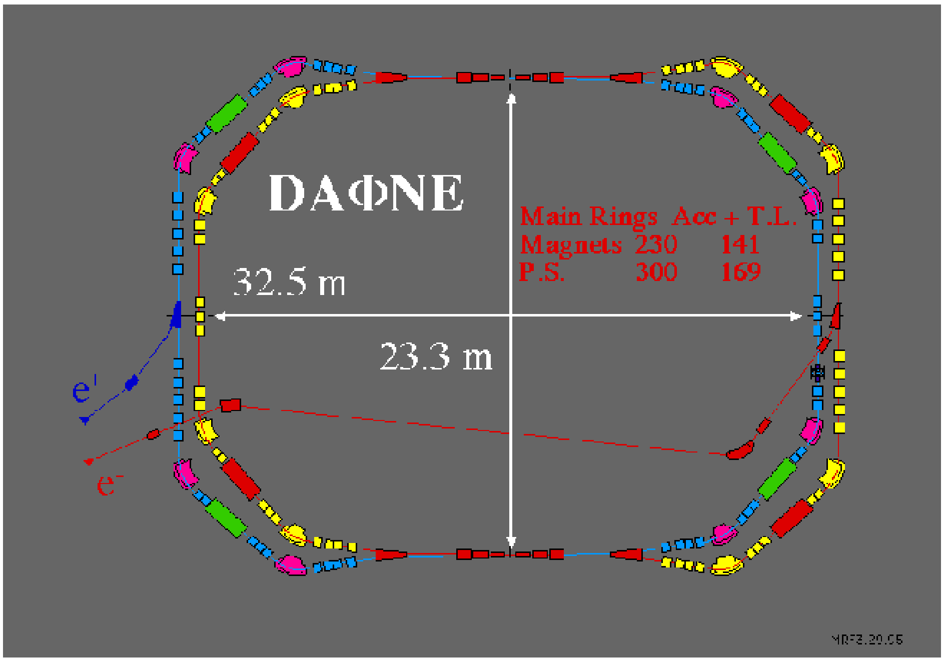

Figure 2.2: Schematic layout of the DAΦNE main rings. Taken from [85].

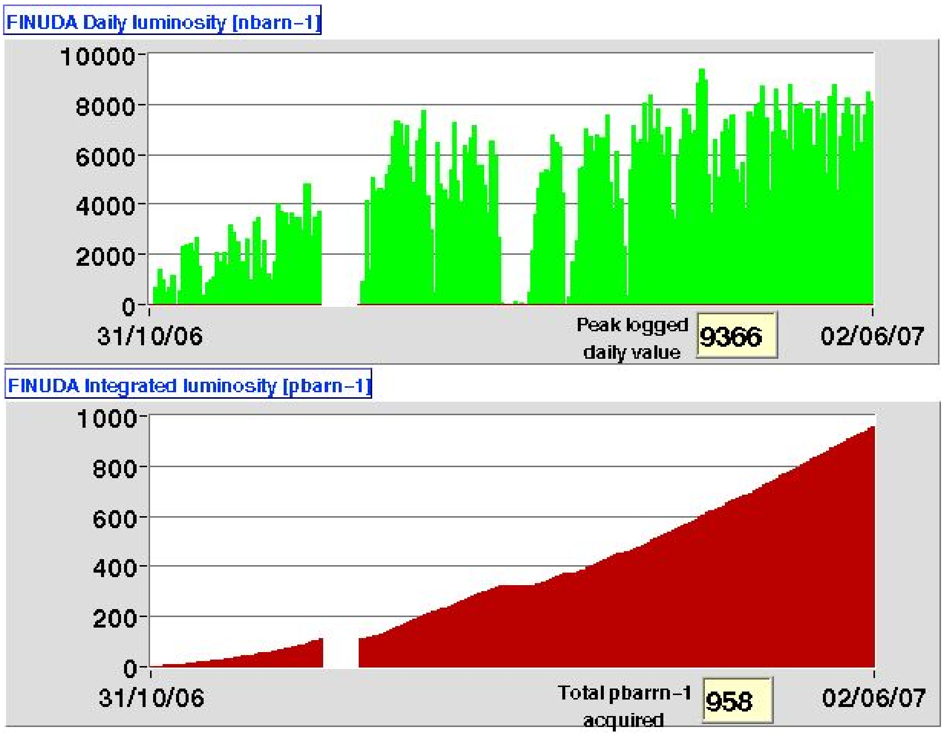

Figure 2.3: Daily and integrated luminosity during the data taking.

Table 2.1: Specifications of detectors.

TOFINO (plastic scintillator)	$\sigma_t \sim 330\,\mathrm{ps}$ (time difference between two slabs)
ISIM (silicon microstrip module)	$\sigma_{r\phi} \sim \sigma_z \sim 30\,\mu\mathrm{m}$
(target)	
OSIM (silicon microstrip module)	$\sigma_{r\phi} \sim \sigma_z \sim 30\,\mu\mathrm{m}$
DCH1 (low mass drift chamber)	$\sigma_{r\phi} \sim 150\,\mu\mathrm{m}$, $\sigma_z \sim 1.5\,\mathrm{cm}$
DCH2 (low mass drift chamber)	$\sigma_{r\phi} \sim 150\,\mu\mathrm{m}$, $\sigma_z \sim 2.0\,\mathrm{cm}$
STRAW (straw tube)	$\sigma_{r\phi} \sim 200\,\mu\mathrm{m}$, $\sigma_z \sim 500\,\mu\mathrm{m}$
TOFONE (plastic scintillator)	$\sigma_t \sim 430\,\mathrm{ps}$ (time difference between two slabs)

2.3 The FINUDA spectrometer

Figure 2.4 is a global view of the FINUDA apparatus, together with a superconducting solenoid which supplies a homogeneous magnetic field of 1.0 Tesla along the beam axis.

The K^+K^- pairs emitted from the center of the spectrometer were stopped in targets, after passing through a beam pipe, an array of plastic scintillator (TOFINO) and silicon microstrip modules (ISIM) (see Fig. 2.5). The region inside the target is called "interaction/target region". The particles emitted from the targets were detected with the detectors in the "tracking region" outside of the targets.

Table 2.1 summarizes specifications of the detectors installed in the spectrometer.

2.3.1 Interaction/target region

There were two kinds of detectors in the interaction/target region: TOFINO, ISIM, together with targets. While OSIM is in the tracking region, it is discussed in this subsection because the modules of ISIM and OSIM are common.

TOFINO

The K^+K^- pairs were triggered and identified with an array of 12 plastic scintillator slabs (TOFINO), located outside of the 500-μm thick beam pipe made of beryllium.

Figure 2.6 is a picture of TOFINO assembled in a mechanical support flange. Each scintillator (EJ-230) was 20-cm long, 3.1-cm wide and 1.8-mm thick, wound with the inner radius of 5.8 cm. On both sides, photomultiplier tubes (R5505-70) which can be operated in a magnetic field up to 1.0 Tesla, were connected.

The energy deposited in TOFINO for slow kaons from the ϕ decay is about 8 times larger than that for minimum ionizing particles (MIP). Therefore, two levels of discrimination

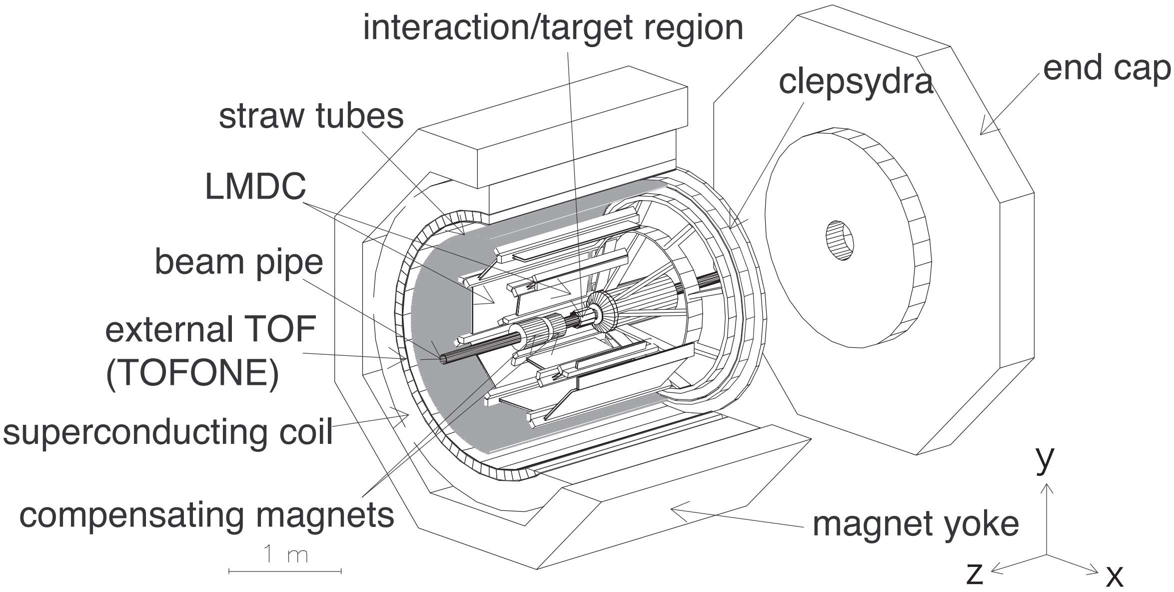

Figure 2.4: Global view of the FINUDA spectrometer.

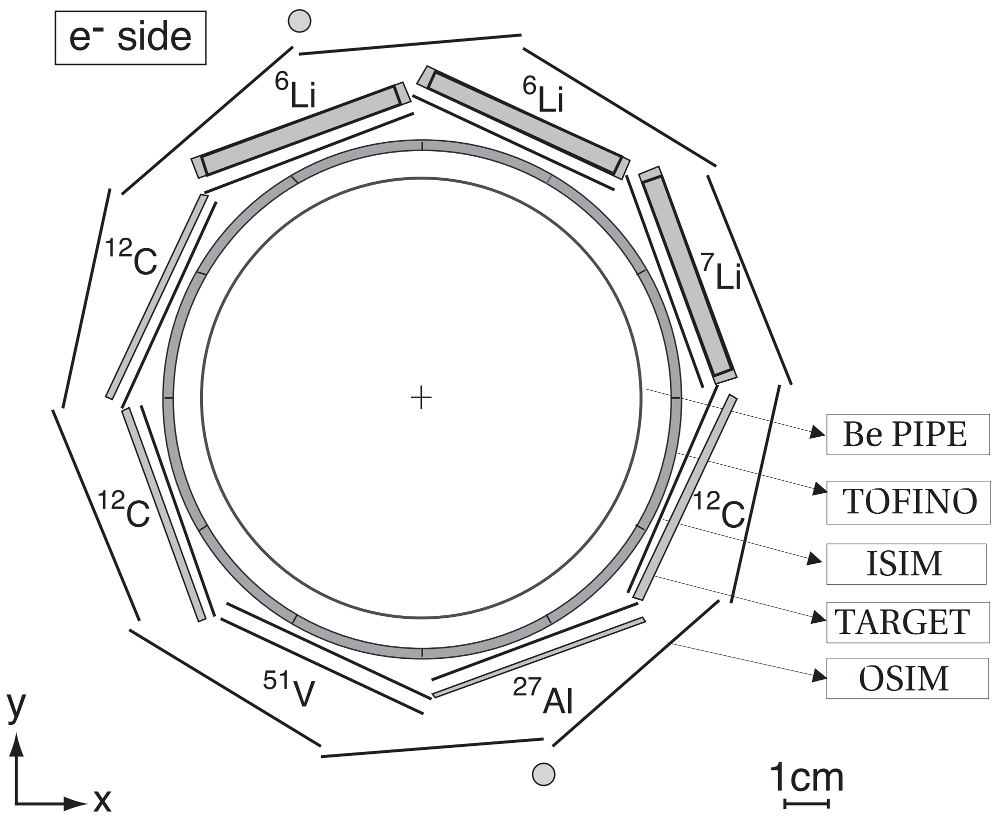

Figure 2.5: Interaction/target region of the FINUDA spectrometer. Note that the target configuration is as for the first data taking.

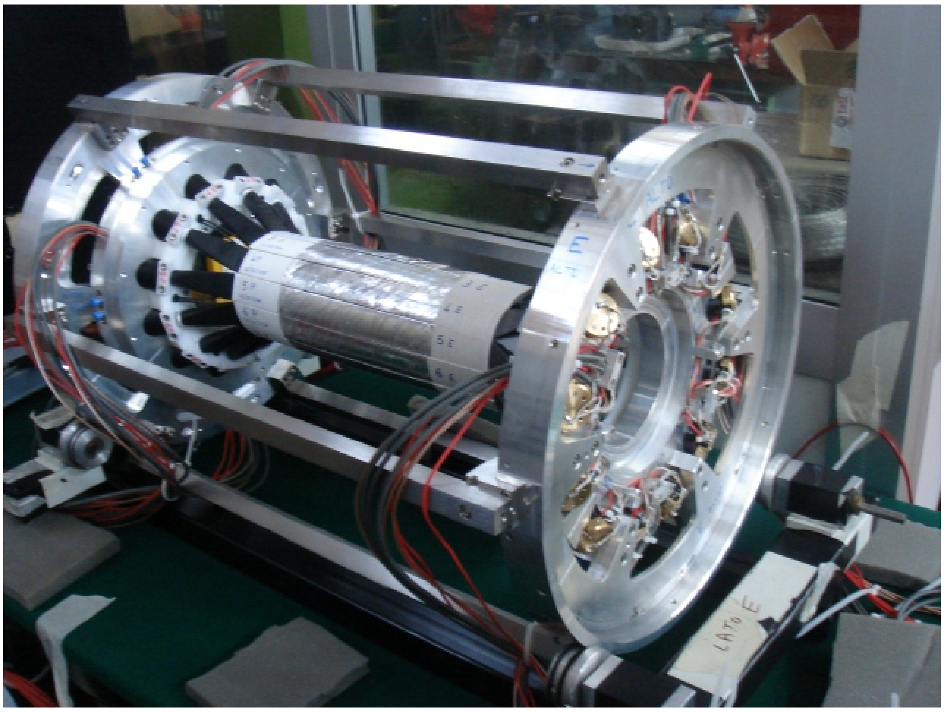

Figure 2.6: Assembled TOFINO detector system.

thresholds were created for the K^+K^- triggers and the e^+e^- triggers from Bhabha scattering.

One of two signal outputs from each PMT was split into two, and the two pulses were independently discriminated by two constant fraction discriminators (CFD) with a low threshold and a high threshold, respectively. Then, the two corresponding TDC's for each PMT were recorded. The other signal output from a PMT was fed into ADC.

The charge distribution, obtained as a geometric mean of ADCs on both e- and p-sides, was obtained as shown in Fig. 2.7. Kaon events were clearly identified by the requirement above high threshold on both sides. By selecting the hits with only low-threshold TDC on both sides, the MIPs were identified. The conversion from channel to photoelectron was carried out so that the contribution of MIPs is normalized to be 50 photoelectrons for every PMT. As expected, MIPs and kaons could be distinguished clearly. For example, a software threshold of 400 photoelectrons was applied to select kaons for slab.

ISIM and OSIM

Two layers of vertex detectors, ISIM and OSIM, sandwich targets. ISIM was composed of 8 modules, and OSIM with 10 modules. Each module had an active surface of 196-mm length and 52-mm width, consisting of three units of double-sided silicon detectors with 300-μm thickness. The pitch of the junction-side strips, for measuring the $r\phi$ coordinate, was 25 μm.

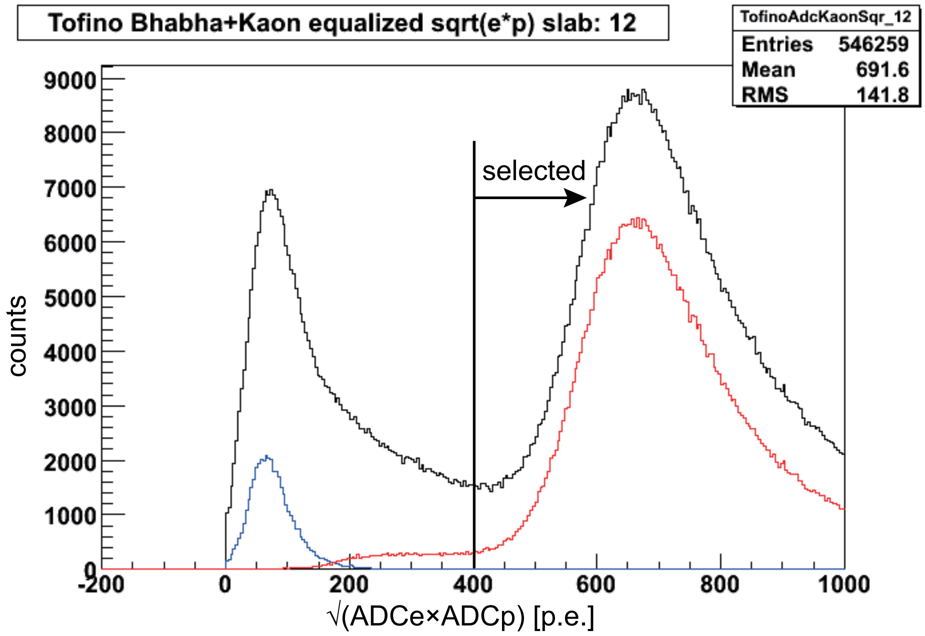

Figure 2.7: Charge ($\sqrt{\mathrm{ADC_e} \times \mathrm{ADC_p}}$) distribution in unit of photoelectrons for one slab of TOFINO. The red and blue histograms correspond to kaons and MIPs after TDC coincidence, respectively.

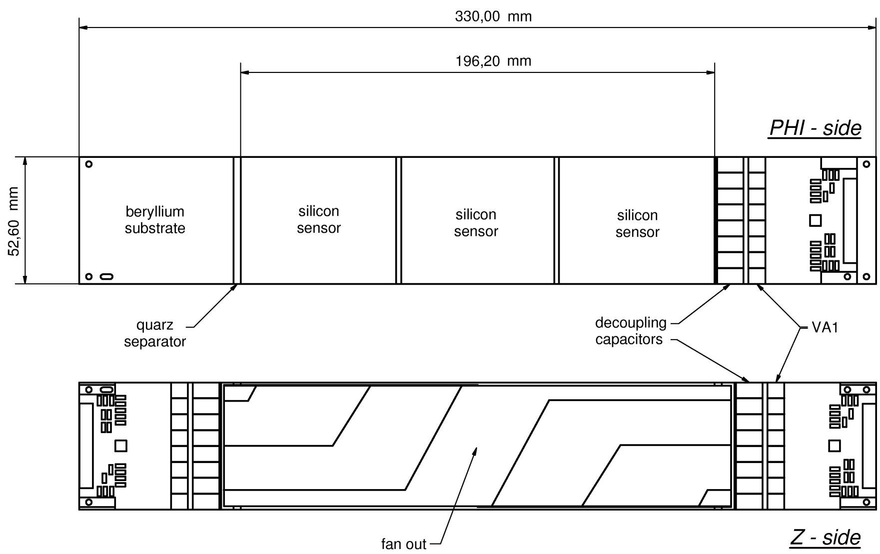

Figure 2.8: Module layout of vertex detectors.

Table 2.2: Dimensions of targets used in the second data taking.

target	$L \times W \times T$ [cm^3]
#1 (^{6}Li)	$17.6 \times 4.75 \times 0.4$
#2 (^{9}Be)	$20.0 \times 5.26 \times 0.2$
#3 (^{7}Li)	$17.6 \times 4.75 \times 0.4$
#4 (^{13}C)	$19.0 \times 4.20 \times 1.0$
#5 (^{7}Li)	$17.6 \times 4.75 \times 0.4$
#6 (D_2O)	$19.0 \times 4.66 \times 0.3$
#7 (^{9}Be)	$20.0 \times 5.26 \times 0.2$
#8 (^{6}Li)	$17.6 \times 4.75 \times 0.4$

Every second strip was connected to a readout strip by use of capacitive charge division, and the readout pitch was 50 μm. The ohmic-side strips, for measuring the z coordinate, had a 50 μm pitch, mutually separated by intermediate p-stop implants. Similarly, its readout pitch was 100 μm. The module layout is shown in Fig. 2.8.

The readout electronics for one module consisted of three hybrids; one for ϕ-side, and two for z-side readout. A hybrid had eight cascaded VA1 integrated circuits, based on a preamplifier followed by a pulse-shaping circuit and an analogue sample/hold circuit. The analog signals were sent to VME flash-ADC cards.

The position resolution for each coordinate was around 30 μm. The energy deposit was utilized for particle identification, among pions, kaons, protons, and heavier particles.

Targets

Except for a ^{13}C target, targets were as thin as 0.2–0.4 cm, so as to minimize the energy loss in the target for outgoing particles. The ^{13}C target (compressed powder) had 1.0 cm thickness. The sizes of the targets are listed in Table 2.2.

2.3.2 Tracking region

In order to minimize multiple scattering, the tracking region was immersed in a helium atmosphere. Two layers of low-mass drift chambers (LMDC) and straw tube detectors were installed for tracking charged particles. In the outermost part, there was an array of 72 plastic scintillator slabs (TOFONE) for measuring the time-of-flight, as well as for triggering purpose.

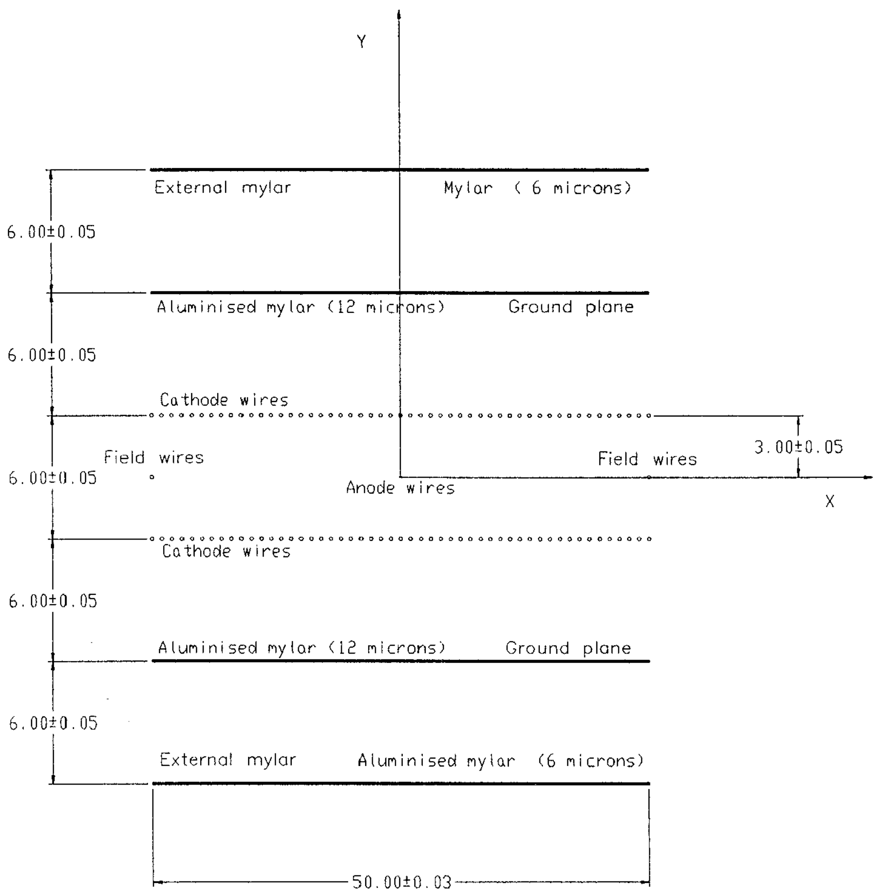

Figure 2.9: Cross section of the drift cell. Note that the anode wire in the center is a doublet of sense wires.

Low mass drift chamber

Both inner and outer layers consisted of eight planar chambers. Their radii were 367 mm and 649 mm. The active volumes for inner and outer chambers were $316 \times 6 \times 930\,\mathrm{mm}^3$ and $566 \times 6 \times 1570\,\mathrm{mm}^3$, respectively. The octagonal structures were rotated by $\sim 11°$, in order to maximize the acceptance for negative pions with 270 MeV/c momentum, which come from the formation of Λ-hypernuclei via the $(K^-_{\mathrm{stop}}, \pi^-)$ reactions.

The key feature of the chamber was to reduce the amount of materials crossed by particles as low as possible. Then, a helium-based gas mixture (62% helium and 38% isobutane) was selected. Furthermore, each chamber had a single layer of sense wires with a diameter of 25 μm, as shown in Fig. 2.9. Despite of no redundancy in a chamber itself, the left-right ambiguity was solved by a doublet of sense wires with 200 μm-separation. The doublets were

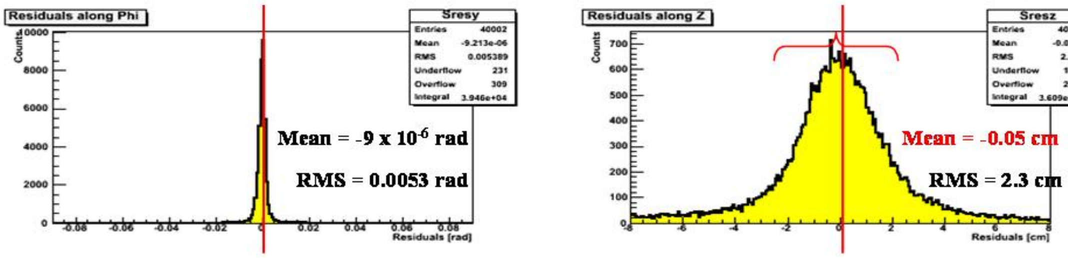

Figure 2.10: Residual along the ϕ coordinate (left) and the z coordinate (right) for inner chambers after alignment.

spaced by 50 mm, and a field wire was located in the center of two doublets. The distance between two parallel layers of cathode wires was 6 mm, and the cathode wire spacing was 1 mm. The voltage supplied to the cathode wires on one side was horizontally displaced from the other, so as to compensate the Lorentz angle.

The space-time relationship for the chamber cell was estimated with the GARFIELD code, because the drift velocity was not saturated at the operating condition of 1.5 kV/cm with the helium-based gas. The z coordinate along the sense wire could be also measured with the charge division method. The difference of the resistances of the sense wires between the avalanche point and both wire ends resulted in the different charges collected on both ends.

A twin differential amplifier for both ends of each doublet was introduced, instead of two single amplifiers. It added a true negative pulse on a wire and an induced positive pulse on the other of the doublet with inverse polarity. The large induced signal around 80% of the direct signal made it possible to improve the signal-to-noise ratio for uncorrelated noise, and also the common noise was automatically cancelled. Hence, a better position resolution along the wire was obtained. The analogue signals from a twin amplifier was fed into ADC and TDC, after being discriminated.

Figure 2.10 shows the present residual distribution for the inner chambers after geometrical alignment.

Straw tube detector

As shown in Fig. 2.11, the straw tube detector was composed of 2 axial- and 4 stereo-layers. Each layer consists of 404 tubes with 15 mm diameter and ~ 2.55 m length, filled with Argon-Ethane (50%-50%) gas mixture. An anode wire had a diameter of 30 μm made of gold-plated tungsten. The stereo tubes had a skew angle of $\sim \pm 12^\circ$ against the beam axis. The drift time was first converted into the drift length perpendicular to the wire. The z coordinate of the trajectory of a particle was estimated from the crossing point of the fired axial tubes and

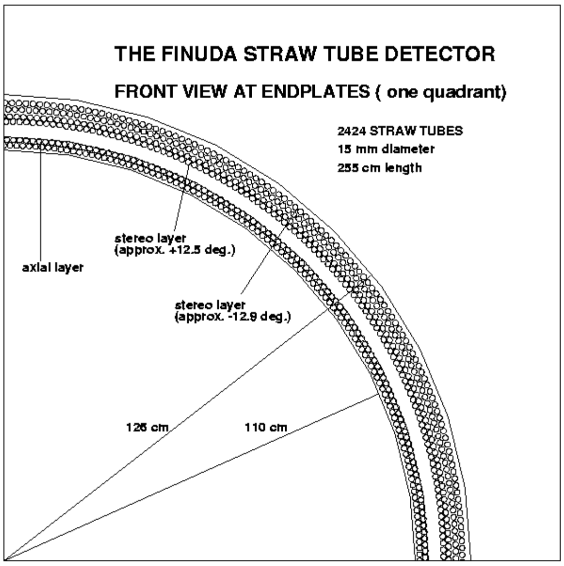

Figure 2.11: Layout of straw tube detectors.

stereo tubes.

By this configuration, the resolution of 200 μm in the $r\phi$ plane and 500 μm along the z coordinate was achieved.

TOFONE

The external scintillator barrel (TOFONE) consisted of 72 trapezoidal plastic scintillator slabs with the length of 2550 mm, the outer width of 116 mm, the inner width of 107 mm, and the thickness of 100 mm. The distance between the beam axis and the inner surface of TOFONE slabs was 1270 mm. The scintillation light was guided to XP2020 photomultiplier tubes, which was located outside the yoke, through a reflecting prism. Both analogue pulses and the discriminator outputs were fed into ADC's and TDC's, respectively.

2.4 Trigger

The trigger logic was based on fast detectors of TOFINO and TOFONE. The bunch crossing RF signal with 2.6 ns interval was not used. We have used three main trigger modes for event selection (HYPE, BHABHA, and COSM) in the data taking.

2.4.1 HYPE trigger

The HYPE trigger selected events with Λ-hypernuclear formation. The event is characterized by a pair of K^+K^- from the ϕ decay and a fast π^- via the $(K^-_{\rm stop}, \pi^-)$ reaction. The kaon pairs were identified with the energy deposit in TOFINO. Because the energy deposits of slow kaons were about 8 times larger than that of MIPs, the kaons can be easily selected with high threshold discriminators. Due to the magnetic field, the event topology is not completely back-to-back and each trajectory is bent toward the same direction. Therefore, for a slab fired by a kaon, we allowed not only the opposite one but also the neighbor ones to the opposite (called as extended back-to-back). The multiplicity ≥ 2 was the requirement for TOFINO, because an additional hit may be caused by an outgoing particle from the target.

For TOFONE, we required the multiplicity ≥ 2. It is not severe for a hypernuclear event, because a curved trajectory of emitted π^- generally passes through more than 2 slabs. The first hit in TOFONE within $\sim 20\,$ns after the TOFINO hit was accepted.

The trigger with TOFONE multiplicity ≥ 1 can not be accepted because of the huge background of Touschek effect caused by DAΦNE in the order of $10^5\,$Hz, compared with a few tens of Hz for hypernuclear events. A scattered electron or positron in a bunch caused by this effect interacts with the beam pipe, and generate a shower. Some of them can still survive even after the event selection with TOFINO. Because the most of the background events had multiplicity 1, the requirement of the multiplicity ≥ 2 reduced the Touschek background to a negligible rate.

While the HYPE trigger was optimized for hypernuclear formation, it was also suitable for two-nucleon absorption processes, since TOFONE multiplicity ≥ 2 could be achieved by two outgoing particles.

2.4.2 BHABHA trigger

Bhabha scattering events $(e^+e^- \to e^+e^-)$ were used for many purposes; the calibration of the detectors with scattered particles, and the monitoring of DAΦNE collider. Especially, the beam luminosity was evaluated from the rate of the Bhabha events.

An extended back-to-back hits in TOFINO with multiplicity $= 2$ and more than 2 hits in TOFONE within a time gate of $\sim 10\,$ns were required in the BHABHA trigger.

2.4.3 COSM trigger

We took the data for cosmic rays with and without magnetic field when the beam was not circulating. They were used for calibration of the detectors. The straight trajectory of cosmic rays without magnetic field was very important in geometrical alignment of the tracking detectors.

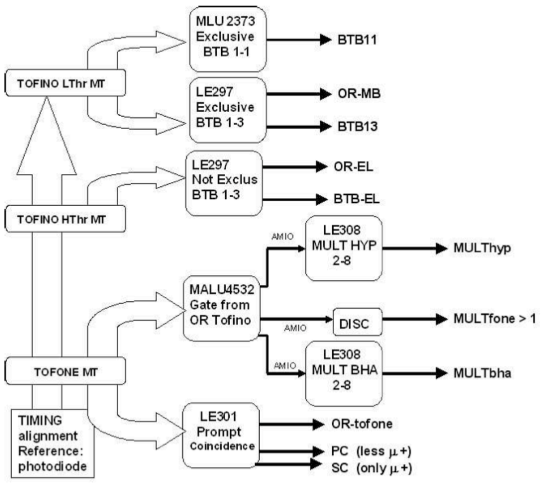

Figure 2.12: Layout of basic trigger selections with TOFINO and TOFONE.

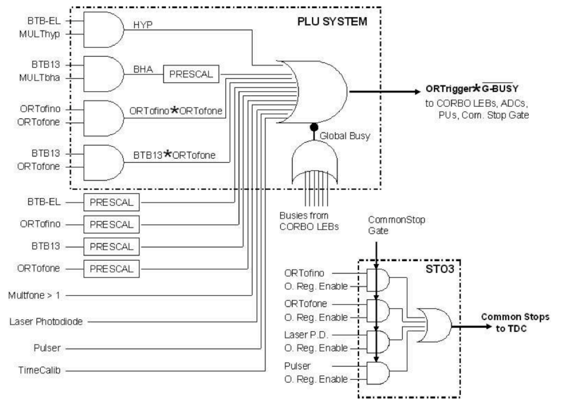

Figure 2.13: Trigger selections given by the programmable logic units (PLU) system.

For a cosmic-ray particle passing through all the layers of the apparatus, we required at least one hit both in TOFINO and TOFONE.

2.4.4 Trigger selection

Figure 2.12 shows the basic trigger selections using the meantimer (MT) signals of TOFINO and TOFONE. Five basic triggers were built up using the low-threshold (LThr) and high-threshold (HThr) MT's from TOFINO, according to the back-to-back pattern (BTB 1-1 or BTB 1-3). As described in Sec. 2.4.1, BTB 1-3 means that for a fired slab, one of the three slabs in the opposite side is fired. Similarly, six basic triggers were built up using the MT's from TOFONE.

The trigger was constructed as a combination of TOFINO triggers and TOFONE triggers by use of Programmable Logic Units (PLU) system, as shown in Fig. 2.13. All the TDC modules were operated in Common Stop mode with the ORtofino signal.

For example, the HYPE trigger was defined by BTB-EL $\otimes$ MULThyp, where BTB-EL is the BTB 1-3 pattern of the HThr MT signals from TOFINO with additional hits allowed (not exclusive), and MULThyp means the TOFONE multiplicity between 2 and 8.

2.5 Data acquisition and on-line monitoring system

The Front End Electronics (FEE) in each VME crate for GTS (global trigger supervisor), STB (straw tubes), LMD (low-mass drift chambers), TOF (TOFINO and TOFONE), ISIM

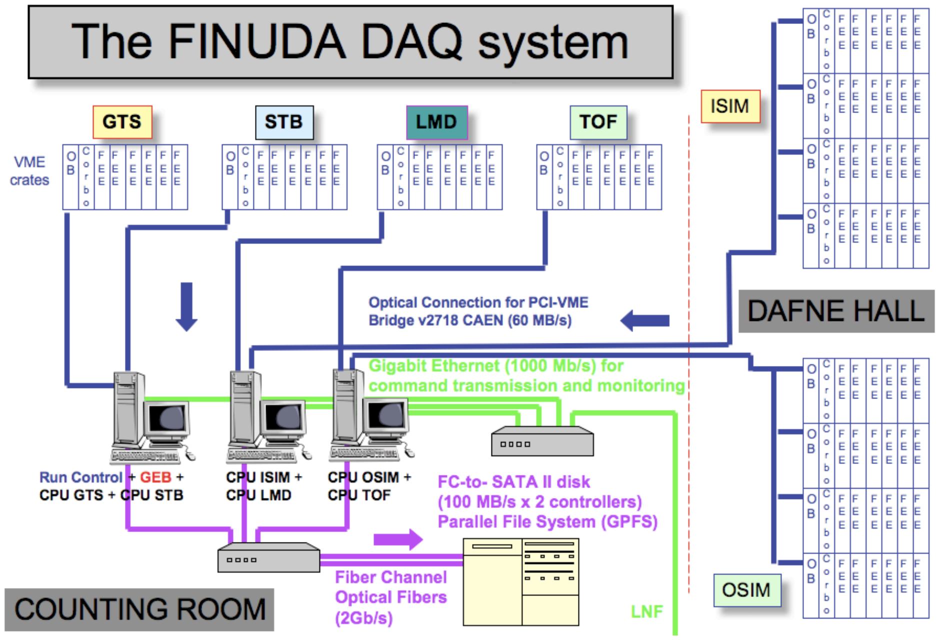

Figure 2.14: Schematic diagram of the data flow.

and OSIM, was read out in parallel by three computers. They were connected by a VME-PCI bridge (CAEN V2718-A2818). Two other processes of Finuda Run Control (FRC) and Global Event Building (GEB) were working on one of the three computers. The FRC program was used for starting and stopping other processes.

Each process read the data and wrote it on a fiber channel disk storage when the FEE received a trigger signal. GEB opened all the files for each of the detectors, and produced a new file with complete events. It also provided the information on events via Ethernet to monitoring processes and event display programs.

2.6 Summary of the data taking

We started the data taking from November 2006, and ended in June 2007. We collected the integrated luminosity of $966\,\mathrm{pb}^{-1}$.

We have collected 210M events with the HYPE trigger, and 32.8M events with the BHABHA trigger. We also took cosmic ray data of 8.8M without magnetic field and 3.7M with magnetic field. The collected HYPE data were 7 times more than in the previous data taking.

Chapter 3

Analysis

3.1 Event reconstruction

In this section, the procedure for event reconstruction is described. First, the stopping points of $K^{\pm}$ are estimated after the identification of kaon pairs, by using the reconstructed hits at detectors in the interaction/target region. If the stopping points are found inside targets, pattern recognition for the hits in the tracking region is carried out for track finding. Once the trajectories are found, the tracks are fitted with a helix curve. Neutrons are identified after the tracking of all the charged particles.

3.1.1 K^+K^- identification

The ϕ mesons were produced with some boost along the horizontal direction (defined as the x-axis), perpendicular to the beam axis (the z-axis). The boost momentum was assumed to be constant, determined by the crossing angle between the electron and positron beams. The two kaons from the ϕ decay have different momenta because of the boost. However, they are still kinematically constrained in a way so that they must be antiparallel with the same momenta in the center-of-mass system. With these constraints and the hits in the vertex detectors (ISIM), the following quantities were estimated:

- the ϕ vertex position,
- the directions and momenta of K^+ and K^- at the ϕ vertex.

From an analysis of the Bhabha scattering ($e^+e^- \to e^+e^-$), the collision points spread in a few mm in the x direction and a few cm in the z direction, as shown in Fig. 3.1. Since the vertical spread is known to be negligibly small from the beam optics, we fixed the y coordinate of the ϕ vertex to be zero. Figure 3.2 shows an example of the reconstructed K^+K^- pair from the ϕ decay near the center of the apparatus.

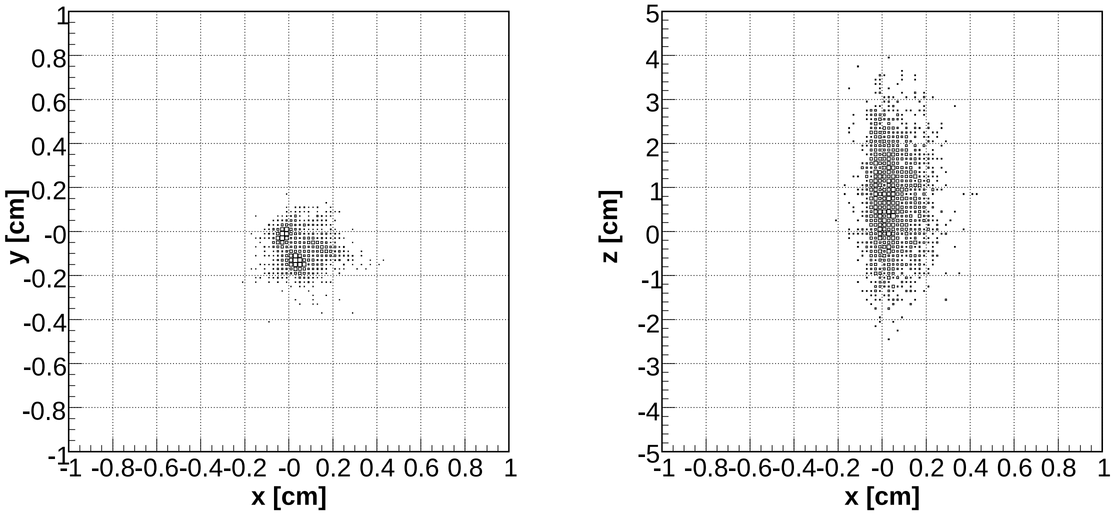

Figure 3.1: ϕ vertex distribution, estimated from the center of the closest approach between the trajectories of electron and positron from the Bhabha scattering.

3.1.2 Pattern recognition for outgoing particles

The spectrometer had five layers of tracking devices; ISIM, OSIM, inner LMDC (DCH1), outer LMDC (DCH2) and straw tubes (STRAW). The hit information of each detector was converted to spacial coordinates as described in Chapter 2. For straw tube detectors, the clustering of the axial and stereo tubes with hits was done first, and a cluster was treated as a single hit in STRAW like in other layers.

In the next step, the pattern recognition was carried out. It connects the hits along an arc in the $r\phi$ plane. The following six combinations of hit patterns were examined in order:

- STRAW–DCH2–DCH1–OSIM(–ISIM),
- STRAW–DCH2–OSIM(–ISIM),
- STRAW–DCH1–OSIM(–ISIM),
- DCH2–DCH1–OSIM(–ISIM),
- DCH2–OSIM–ISIM,
- OSIM–ISIM–ISIM,

where a hit in the detector is simply abbreviated as the detector name. For the first four combinations, a hit in ISIM was connected if found, when the corresponding particle was emitted inward from the target.

Among the six combinations shown above, two categories of tracks with STRAW–DCH2–DCH1–OSIM(–ISIM) and DCH2–DCH1–OSIM(–ISIM) were used for the further analyses. For simplicity, they are named as “long tracks” and “short tracks”, respectively.

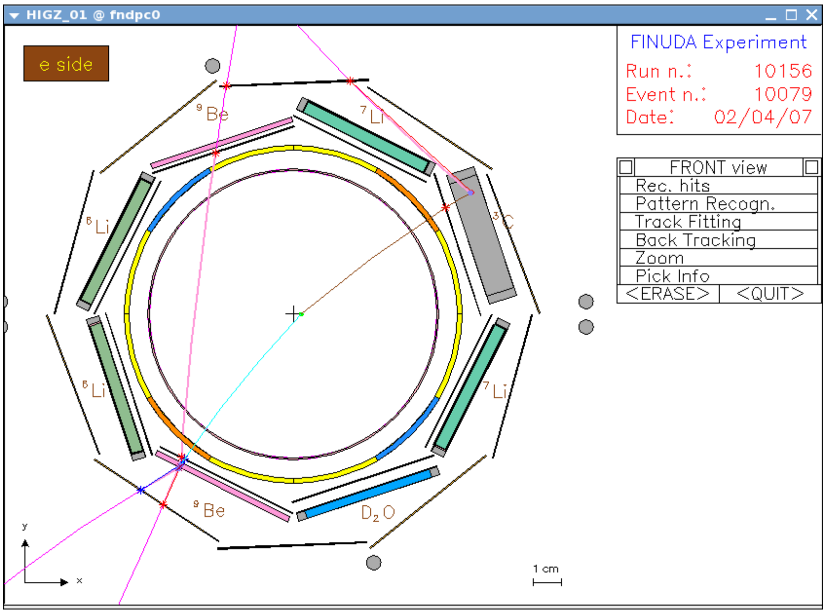

Figure 3.2: Example of reconstructed K^+ (brown) and K^- (aqua), together with outgoing particles (magenta). The dot near the cross in the center is the estimated ϕ vertex.

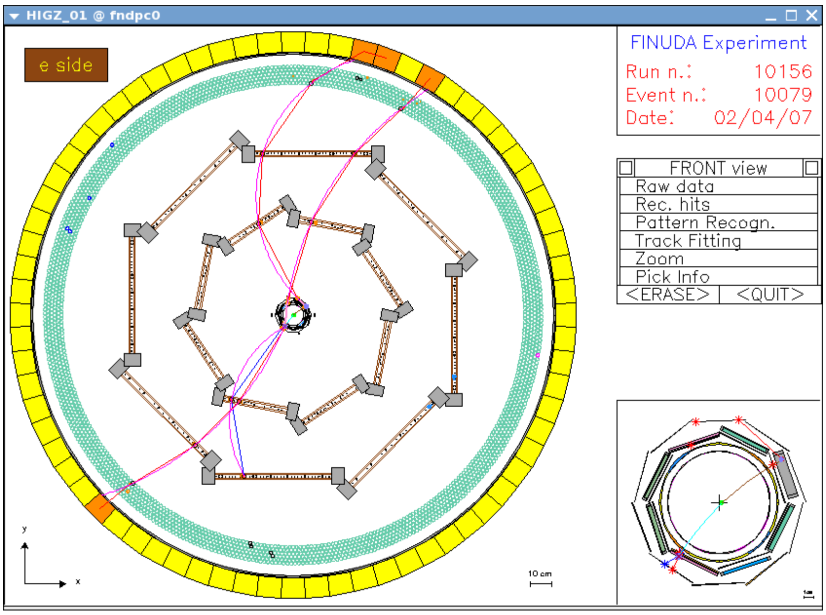

Figure 3.3: Example of reconstructed outgoing particles for the same event as above. In this event, three particles from the K^- vertex ($p\pi^-$ from Λ decay, in a similar direction, and a proton in the opposite direction) and one μ^+ from the K^+ vertex are reconstructed. The broken lines in red (positive particles) and blue (negative particles) are the result of pattern recognition.

For example, the procedure for finding a long track is as follows. A circle which connects STRAW–DCH2–DCH1 was uniquely determined in the $r\phi$ plane for any three hits. If there were hits in OSIM and/or ISIM along the circle, these hits were connected to the circle. Tracks without hits in OSIM were discarded at this stage. The hit in OSIM was required because it was used for particle identification later.

The circle in the $r\phi$ plane or the helix was validated as a trajectory, if all the hits were also on the helix along the z direction. This was checked by a linear fit in the $z\phi$ plane in the local coordinate system of the helix, with the origin defined as the center of the circle. If there was a TOFONE hit on the helix, it was also connected, but not used for the fitting.

After pattern recognition, the momentum and charge were obtained in the three-dimensional fit with a helix. The energy loss in the interaction/target region or in the target was corrected using the track information. The particle identification was done at this stage from the energy deposit in OSIM, together with the measured momentum and charge.

Figure 3.3 shows a typical reconstructed event after the K^+K^- reconstruction as zoomed up in Fig. 3.2. Red and blue tracks correspond to the positive and negative particles, respectively. Two long tracks (protons) and one short track (π^-) from a K^- stopping point, and one long track (μ^+) from a K^+ stopping point are successfully reconstructed. Here, the lower proton and the pion originated from a Λ particle decaying between the target and an OSIM module. It is worth mentioning that the track multiplicity both from K^- and K^+ was generally less than 3, and the event with multiplicity 4 (such as the event in Fig. 3.3) accounts for only $\sim 0.2\%$ over the events with both kaons stopped inside targets.

3.2 Charged particles

Charged particles both from the K^- and K^+ vertices were tracked simultaneously. While in the stopped K^- absorption particles are emitted in a widely spread momentum due to the Fermi motion of the interacting nucleon(s), particles from the K^+ stopped in a target are emitted just like in a free space with the following two-body decay modes [84]:

$$K^+ \rightarrow \mu^+ + \nu_\mu, \qquad (\text{B.R.} = 63.44 \pm 0.14\%) \tag{3.1}$$

$$K^+ \rightarrow \pi^+ + \pi^0. \qquad (\text{B.R.} = 20.92 \pm 0.12\%) \tag{3.2}$$

They produce μ^+ and π^+ with the characteristic momenta.

3.2.1 Charged particles from K^+ vertices

The muons (236 MeV/c) from the $K_{\mu 2}$ decay (Eq. (3.1)) and the pions (205 MeV/c) from $K_{\pi 2}$ decay(Eq. (3.2)) can be observed as long tracks, as shown in Fig. 3.4. These monochromatic peaks were used for estimation of the accuracy of the absolute momentum, momentum resolution and the number of stopped kaons.

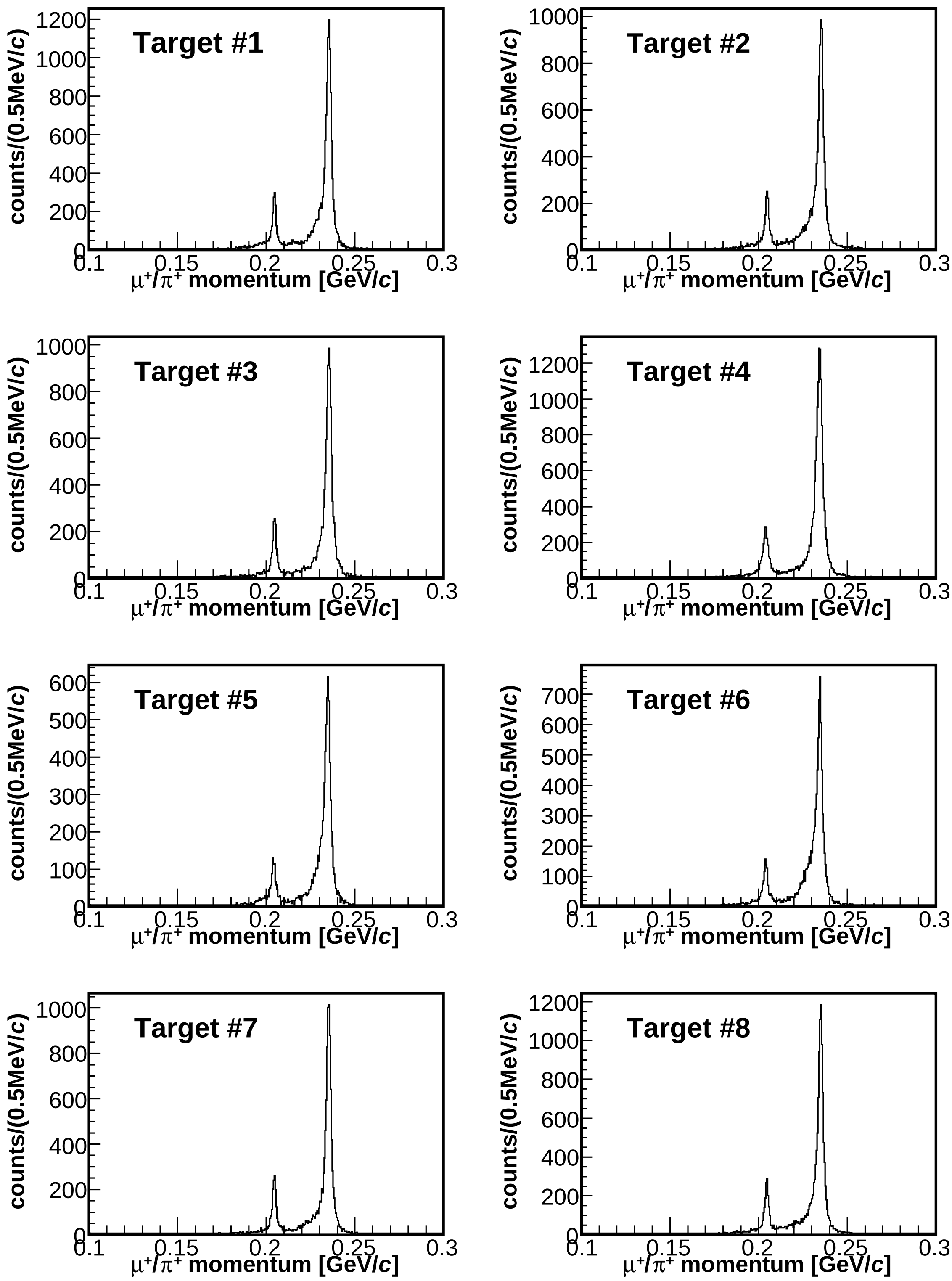

Figure 3.4: Momentum distribution of positive particles from K^+ vertices.

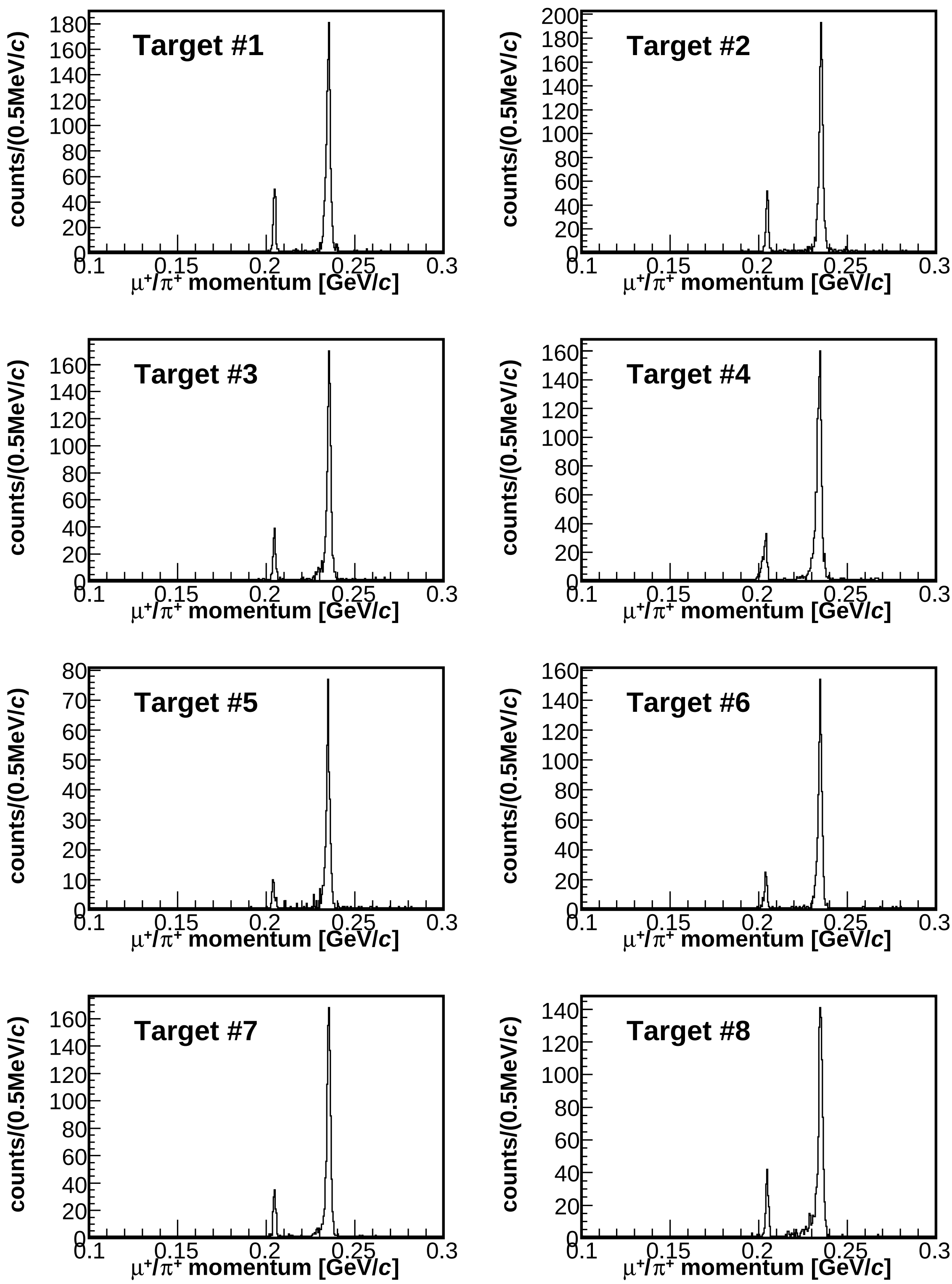

Figure 3.5: Same as Fig. 3.4, but a tight quality cut is applied.

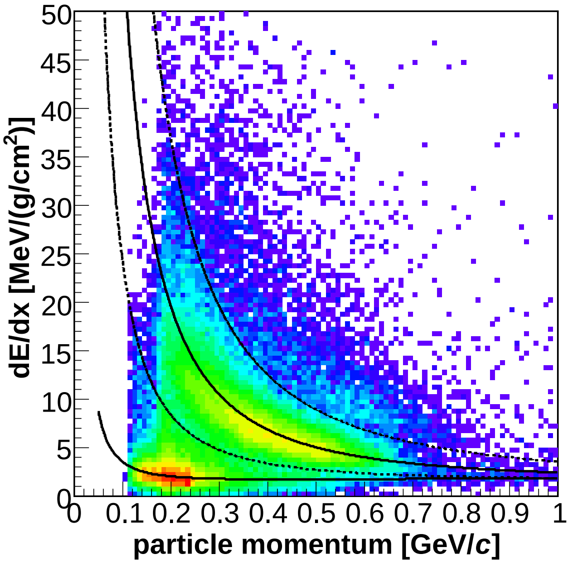

Figure 3.6: Energy deposit at OSIM versus particle momentum. The curves obtained from the Bethe-Bloch formula for protons (up) and pions (down) are also shown. The dotted lines mean the boundary for particle selection.

By imposing a quality cut on the tracks on the emission angles (relative to the normal line of the target surface), χ^2 and residuals, a better resolution was obtained ($\sigma_p/p \sim 0.5\%$) as shown in Fig. 3.5. In this thesis, no such cut was applied for the tracks, since the resolution was enough to observe the signals such as Λ's and Σ^-'s in the invariant mass spectrum.

3.2.2 Charged particles from K^- vertices

As described in Sec. 1.2, the one-nucleon absorption process which emits a hyperon and a pion is predominant (about 80% per stopped K^-), whereas the rest (about 20% per stopped K^-) has only hyperon and nucleons without pions in the final state.

The charged pions and protons mainly emitted from the K^- vertices were distinguished with an array of silicon microstrip detectors (OSIM). Figure 3.6 shows a scatter plot of the energy deposit (dE/dx) versus the particle momentum. The energy deposits for pions and protons distribute along the mean values calculated from the Bethe-Bloch formula, and pions and protons can be clearly distinguished.

In Figs. 3.7 and 3.8, the inclusive momentum distributions for π^- and proton in the HYPE trigger are shown for all the targets.

For a reference, the ($K^-_{\rm stop}$, π^-) spectrum on ^{12}C target obtained by Tamura *et al.* [86] is shown in Fig. 3.9. Roughly speaking, slow π^-'s, observed as short tracks, come from the

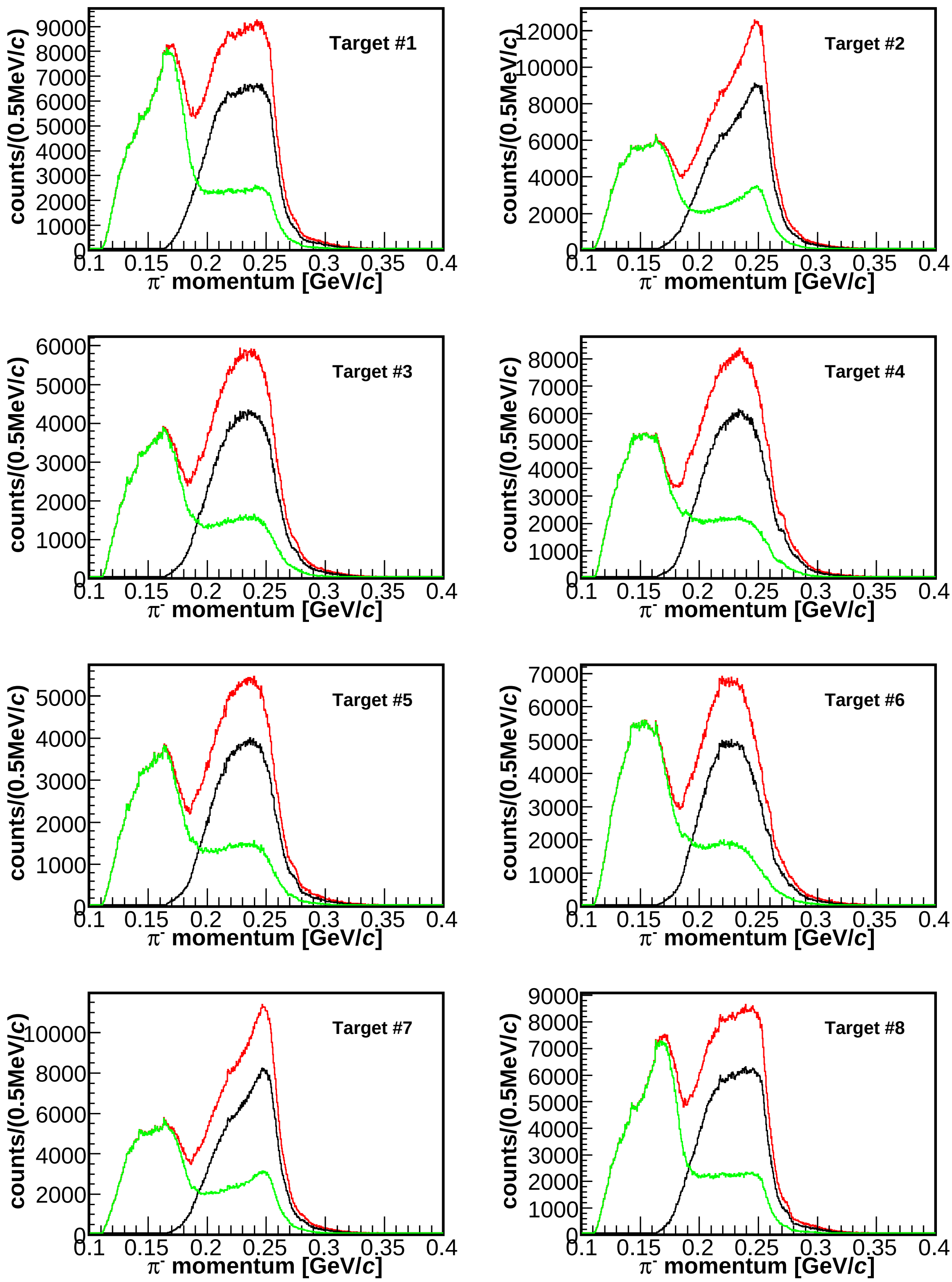

Figure 3.7: Momentum distribution of π^- from K^- vertices. The black and green histograms correspond to long tracks and short tracks, respectively, and the sum is shown in red histograms.

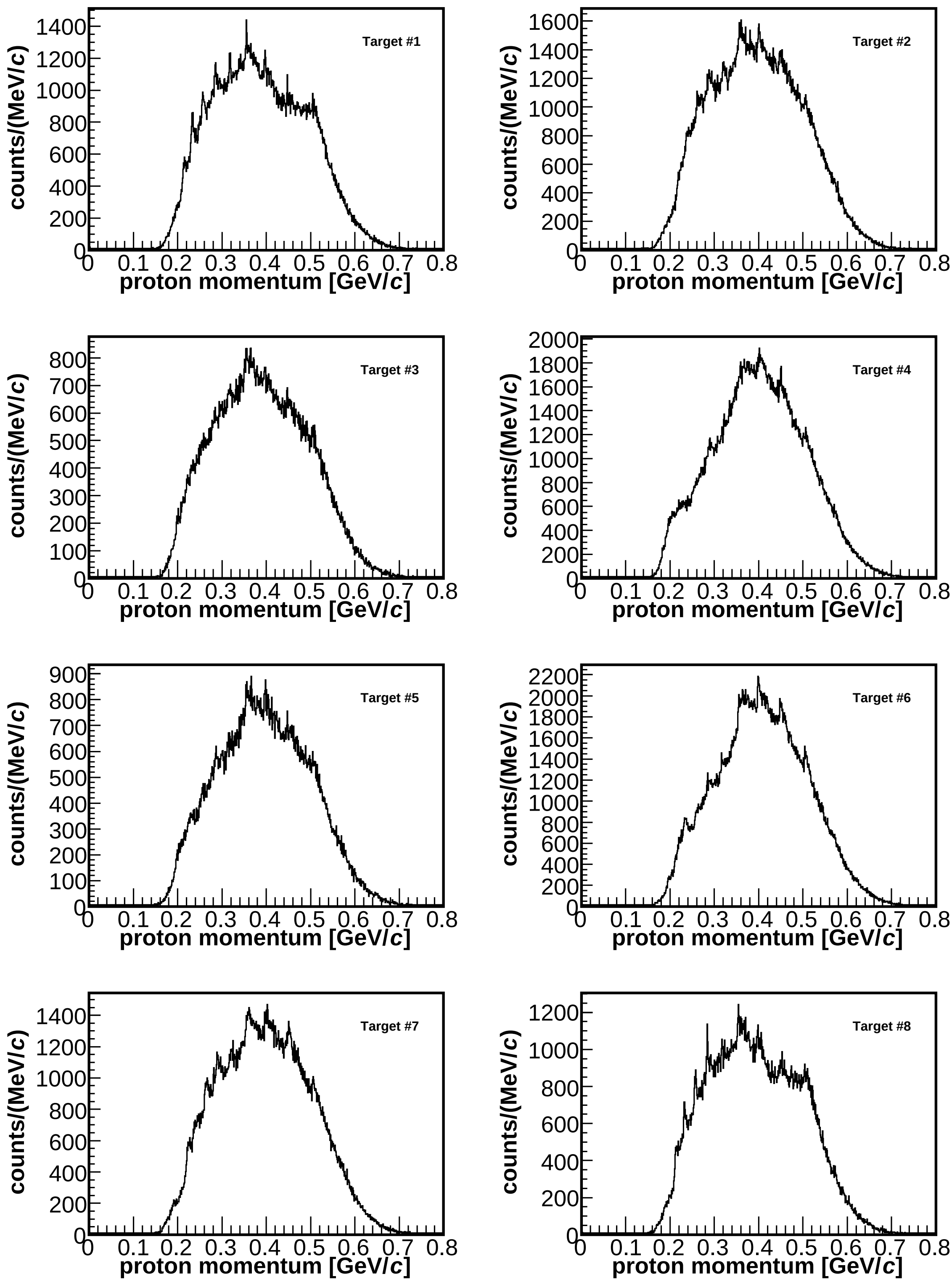

Figure 3.8: Momentum distribution of long-track protons from K^- vertices.

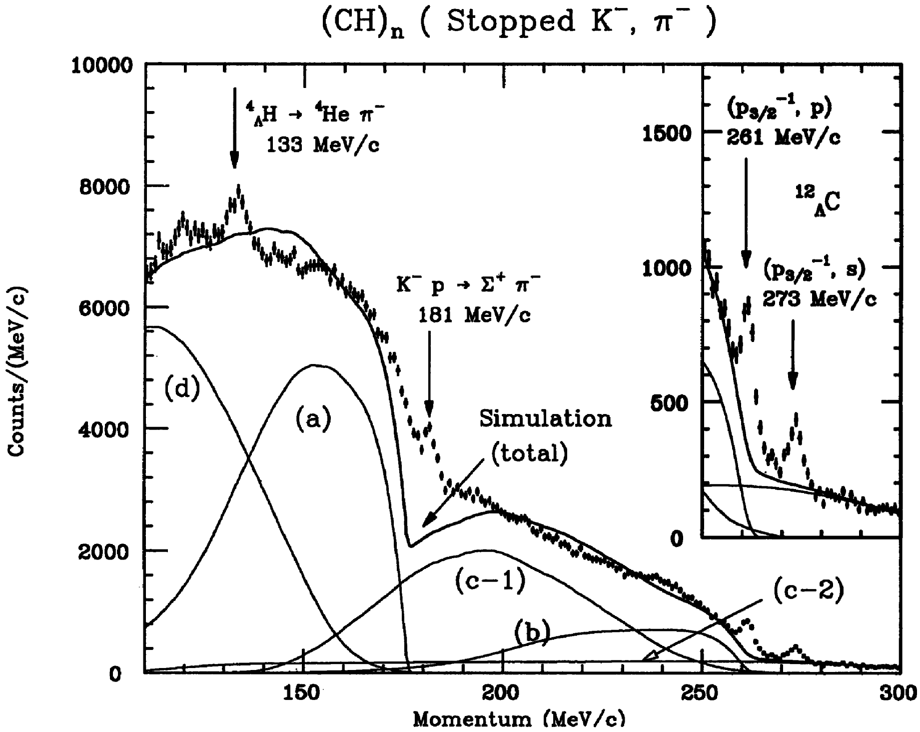

Figure 3.9: ($K^-_{\rm stop}$, π^-) spectrum on ^{12}C target. Thin lines show the result of the decomposition into each process, (a) $\Sigma^+\pi^-$ and $\Sigma^0\pi^-$ productions, (b) $\Lambda\pi^-$ production, (c-1), (c-2) $\Sigma^- \to n\pi^-$ decay ((c-2) corresponds to Σ produced by two nucleon absorption of K^-), (d) $\Lambda \to p\pi^-$ decay. Taken from Fig. 2 in [86].

decay of Λ or the quasi-free Σ production, and fast π^-'s detected as long tracks originate from the decay of Σ^- or the quasi-free Λ production.

Acceptance and momentum resolution

The geometrical acceptance for pions and protons was estimated with a Monte Carlo simulation based on the GEANT3 package. It generates a pair of $K^\pm$ as the decay product of a ϕ meson in the center of the spectrometer, and particle(s) from the stopping point of K^- isotropically. When a particle passed through a detector, its hit information was stored after digitization. The reconstruction program for a simulation is almost the same as for the real data, but the hit position and timing was smeared out with its intrinsic resolution (Table 2.1). Then, the reconstruction efficiency was automatically taken into account. In the simulation, the detection efficiency of each detector was not considered, as all the detectors were assumed to be always active.

The overall detection efficiency was estimated from the data in the next subsubsection. As

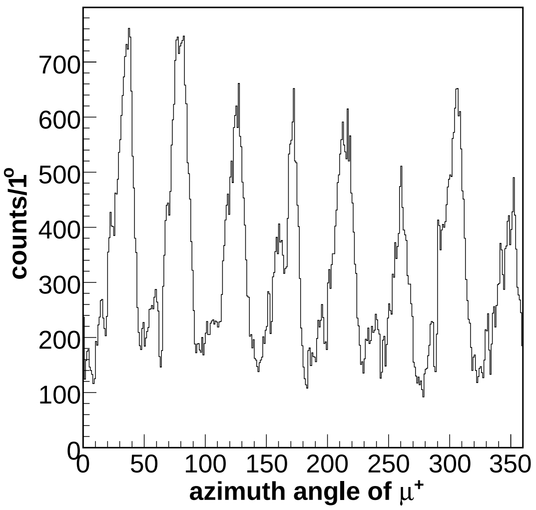

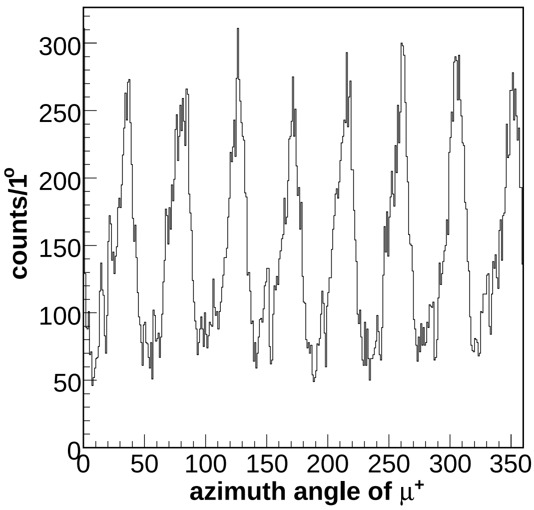

Figure 3.10: Azimuth angle distribution of μ^+ from the K^+ decay for the real data (left) and a simulation (right).

an example, the distributions of the azimuth angle in the $r\phi$ plane of the emitted μ^+ from the K^+ decay are shown in Fig. 3.10. In the real data, the detection efficiency had a dependence on the azimuth angle, mainly because the eight chambers in a layer had a different detection efficiency. However, it would be averaged in the analysis because a particle from the $K^\pm$ vertices is emitted isotropically.

The Monte Carlo results are shown in Figs. 3.11 and 3.12. The detection threshold for long tracks was found to be around 180 MeV/c for pions and 220 MeV/c for protons. Since the energy loss for protons is much larger than that of pions (cf. Fig. 3.6), a higher momentum is required for a proton to be detected. While this pion threshold momentum is low enough for hypernuclear spectroscopy, the pions from the Λ decay are almost below the threshold (cf. Fig. 3.9 and Fig. 3.21). Therefore, a short-track pion was also included for detection of a Λ. The difference of the acceptance between π^+ and π^- comes from the geometrical design of the mechanical supports of DCH1 and DCH2. The acceptance of π^- was higher because the tracking device was optimized for the detection of π^- as described in Sec. 2.3.2.

The momentum and kinetic energy resolution for pions and protons obtained from the simulation are shown in Figs. 3.13 and 3.14. The observed resolution (σ_p = 1.5–1.7 MeV/c) for the monochromatic μ^+ peak from the $K_{\mu 2}$ decay was consistent with this simulation.

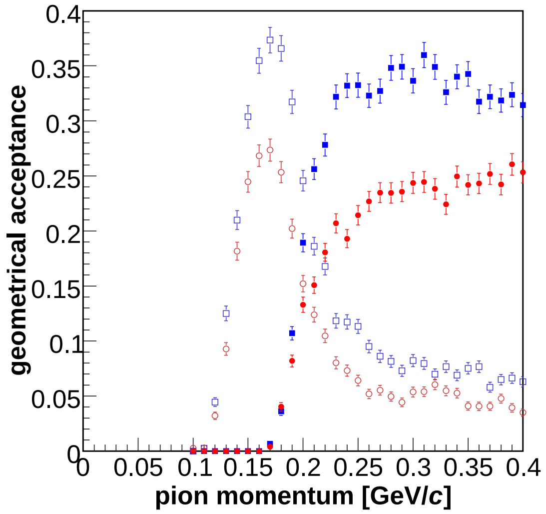

Figure 3.11: Geometrical acceptance for charged pions. The red/blue points corresponds to π^+ and π^-, and the filled/open marker corresponds to long/short tracks.

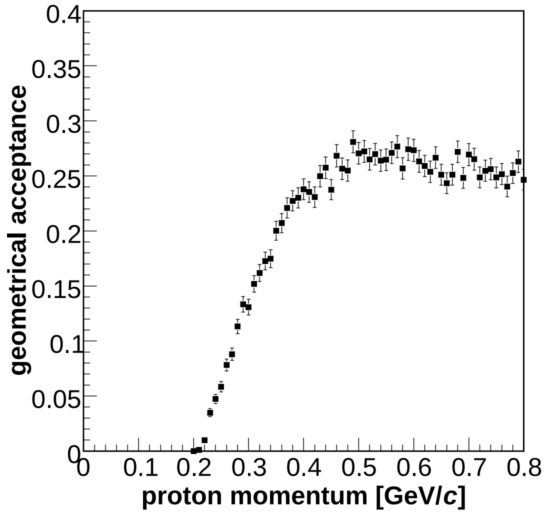

Figure 3.12: Geometrical acceptance for protons.

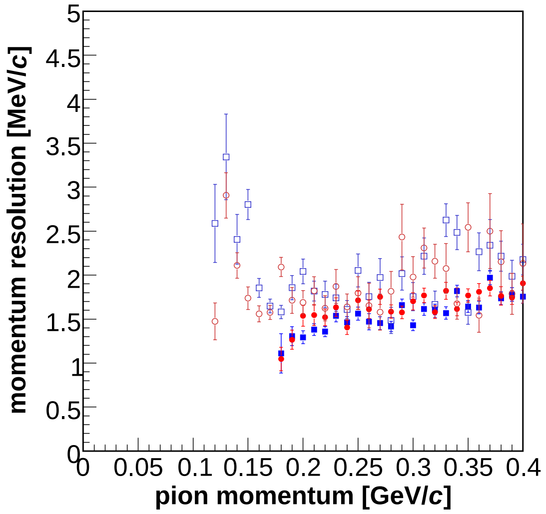

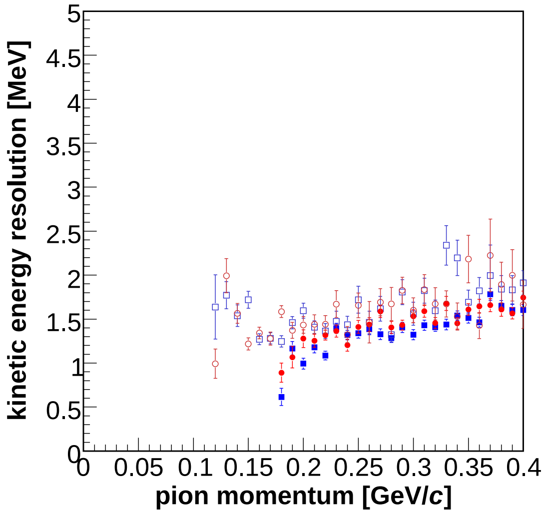

Figure 3.13: Momentum (left) and kinetic energy (right) resolution for charged pions. The usage of markers is the same as in Fig. 3.11.

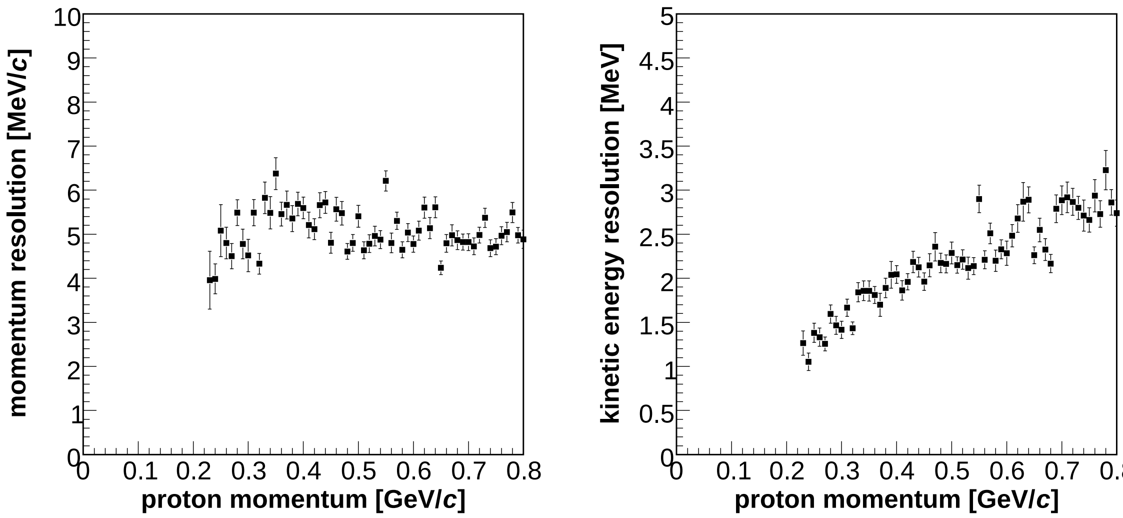

Figure 3.14: Momentum (left) and kinetic energy (right) resolution for protons.

Overall detection efficiency

The overall detection efficiency for a particle, which is the product of the efficiency of each detector where the particle crossed, was estimated in the following way.

In order to avoid the ambiguity on the trigger efficiency, events with pion(s) from K^- satisfying the multiplicity of TOFONE ≥ 2 were used for estimating the detection efficiency of a long-track μ^+ from K^+. The ratio of $N(\mu^+)/N(K^+_{\mathrm{stop}})$ was compared for the real data and the simulation. Then, the detection efficiency for a long track was obtained as $\epsilon^{(\mathrm{long})} = 0.555 \pm 0.023$.

For the detection efficiency for a short track ($\epsilon^{(\mathrm{short})}$), it was assumed that the detection efficiency of STRAW is written as $\epsilon^{\mathrm{STRAW}} = \epsilon^{(\mathrm{long})}/\epsilon^{(\mathrm{short})}$. Then, taking into account that a long track in a simulation is regarded as a short track with the probability of $(1 - \epsilon^{\mathrm{STRAW}})\epsilon^{(\mathrm{short})}$, the following relationship was obtained:

$$\frac{N^{(\mathrm{MC})}(\mu^{+(\mathrm{long})})(1-\epsilon^{\mathrm{STRAW}})\epsilon^{(\mathrm{short})} + N^{(\mathrm{MC})}(\mu^{+(\mathrm{short})})\epsilon^{(\mathrm{short})}}{N^{(\mathrm{MC})}(K^+)} = \frac{N(\mu^{+(\mathrm{short})})}{N(K^+)}, \tag{3.3}$$

where $N^{(\mathrm{MC})}$ is the number obtained from the Monte Carlo simulation. Substituting $\epsilon^{\mathrm{STRAW}} = \epsilon^{(\mathrm{long})}/\epsilon^{(\mathrm{short})}$, $\epsilon^{(\mathrm{short})} = 0.680 \pm 0.041$ was obtained.

3.3 Neutral particles

A neutron was identified with an isolated hit in TOFONE, unconnected to any tracks of charged particles. The straw tube detectors, within 34 cm from the hit point in TOFONE, serve as a veto counter for charged particles.

A neutron can be detected with plastic scintillator slabs of TOFONE. Because a charged particle generally enters a slab at an inclined angle and fires adjacent slabs due to the curvature of the trajectory, a neutron entering almost perpendicularly to the surface can be identified by an isolated hit.

The time-of-flight (TOF) of a neutron was defined as the time difference between TOFINO and TOFONE. Here, the hit in TOFINO was caused by a K^- before entering the target. The momentum of the kaon depends on the emission angle, because the ϕ meson is produced with $p_x \sim 15\,\mathrm{MeV}/c$ due to the finite crossing angle between the electron and positron beams. Therefore, the stopping time of kaons after passing through TOFINO is different target by target. It was calibrated by using the timing of prompt γ's, which are expected to be emitted soon after the K^- absorption.

The flight path (L) was obtained from the distance between a K^- vertex and a hit position in TOFONE. The hit position in the $r\phi$ plane was defined as the center of the fired slab, and the z-coordinate was estimated from the time difference between PMTs on both ends of the slab.

Figure 3.16 shows $1/\beta$ spectra for all the targets after correcting the peak of prompt γ's to be centered at $1/\beta = 1$. The $1/\beta$ resolution estimated from the peak was ~ 0.12, as summarized in Table 3.1. The obtained momentum distribution for each target is shown in Fig. 3.17. Neutrons with momentum larger than $200\,\mathrm{MeV}/c$ were used for the further analyses. The calculated energy/momentum resolutions are plotted in Fig. 3.18 as functions of neutron energy.

The detection efficiency was estimated using a hadronic interaction model of the GFMFIN (FLUKA for neutrons above 20 MeV and MICAP for neutrons below 20 MeV) simulation in the GEANT3 package. A pair of proton and neutron in back-to-back ($\cos\theta = -1$) was generated from the K^- vertex in the simulation so as to reduce background hits not caused by the generated neutron. In order to avoid the contribution from the K^+ decay mentioned later, the decay particles from K^+ were not generated. The detection efficiency was obtained by selecting back-to-back pn pairs ($\cos\theta(pn) < -0.999$ or $\theta(pn) > 177.4°$). The result is shown in Fig. 3.15. Here, the average threshold for each PMT was 3MeVee[1], which was estimated from the obtained ADC spectrum.

Not only neutral particles from K^- vertices but also γ's from K^+ vertices can fire a slab of TOFONE. Since the lifetime of K^+ (12.4 ns) is much longer than the time-of-flight of a photon, $\pi^0 \to 2\gamma$ from K^+ decay (such as Eq. (3.2)) can make a continuous background. Figure 3.19 shows the distribution of TOF $- L/c$ for all neutral particles in coincidence with π^+ or μ^+ from the K^+ vertex, where L is the flight length and c is the speed of light. In case of a photon, it should be the time when the photon is emitted. The distribution is

[1] 1 MeVee (MeV electron equivalent) corresponds to the light output by an 1MeV electron.

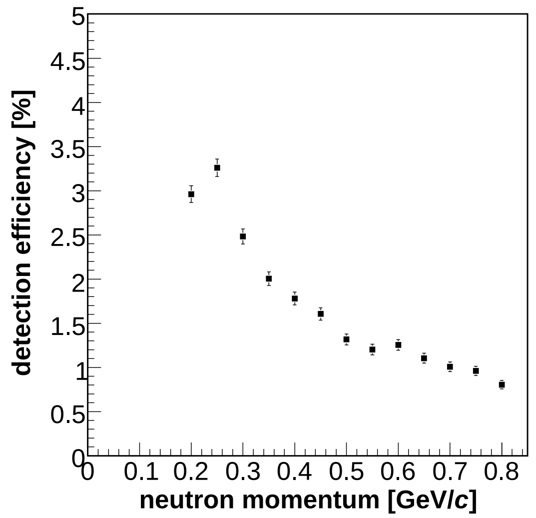

Figure 3.15: Detection efficiency of neutrons.

Table 3.1: $1/\beta$ resolution for neutral particles.

target	$1/\beta$ resolution (σ)
#1	0.120
#2	0.120
#3	0.121
#4	0.118
#5	0.122
#6	0.127
#7	0.119
#8	0.121

normalized by the total number of muons or pions observed. Clearly, the distribution with π^+ coincidence (associated with $\pi^0 \to 2\gamma$) has an excess over that with μ^+ coincidence. The difference between two distributions rises up at $\sim 0\,\mathrm{ns}$ and decreases slowly. This excess can be attributed to the delayed γ's originating from the decay of K^+.

This excess is also seen in the momentum distribution, as shown in Fig. 3.20. It overlaps with the signal in the momentum region of interest (0.2–$0.7\,\mathrm{GeV}/c$). Since delayed γ's are emitted randomly and irrelevant to particles from stopped K^- absorption, it is effective to apply an angular cut in back-to-back for a final state including neutrons, such as Λn or $\Sigma^- p$ pairs, as discussed in Chapter 4.

3.4 Estimation of number of stopped kaons

Because both K^+ and K^- are produced simultaneously from the ϕ decay, the number of stopped K^-'s can be assumed to be almost the same as that of stopped K^+'s. The total number of stopped K^+'s can be estimated by using the number of μ^+'s emitted from the stopped K^+'s. It is described as $N(K^+_{\mathrm{stop}}) = N^{(\mathrm{obs.})}(\mu^+_{\mathrm{trig}})/\epsilon(\mu^+_{\mathrm{trig}})$, where $N^{(\mathrm{obs.})}(\mu^+_{\mathrm{trig}})$ is the number of observed μ^+'s with TOFONE multiplicity ≥ 2 [2], and $\epsilon(\mu^+_{\mathrm{trig}})$ is the detection efficiency of μ^+_{trig} per stopped K^+. $N(K^+_{\mathrm{stop}})$ is not the number of stopped K^+'s supplied by DAΦNE, but the reconstruction efficiency of K^+K^- pairs with TOFINO and ISIM is

[2] Hereafter, a μ^+ with TOFONE multiplicity ≥ 2 is called as μ^+_{trig}. A single μ^+_{trig} is enough to satisfy the trigger condition of TOFONE multiplicity without any other particles from the K^- vertex.

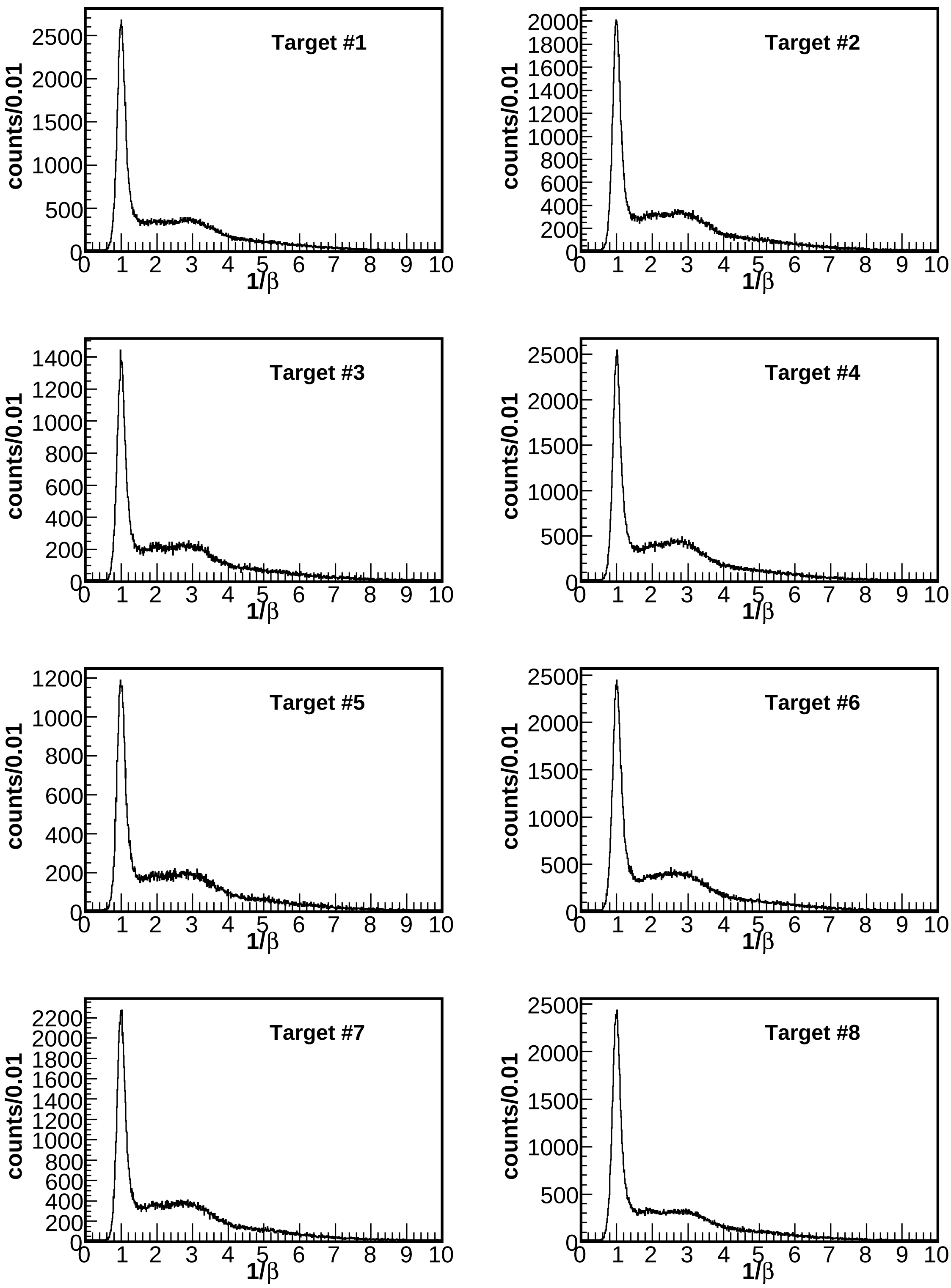

Figure 3.16: $1/\beta$ spectrum of neutral particles for each target.

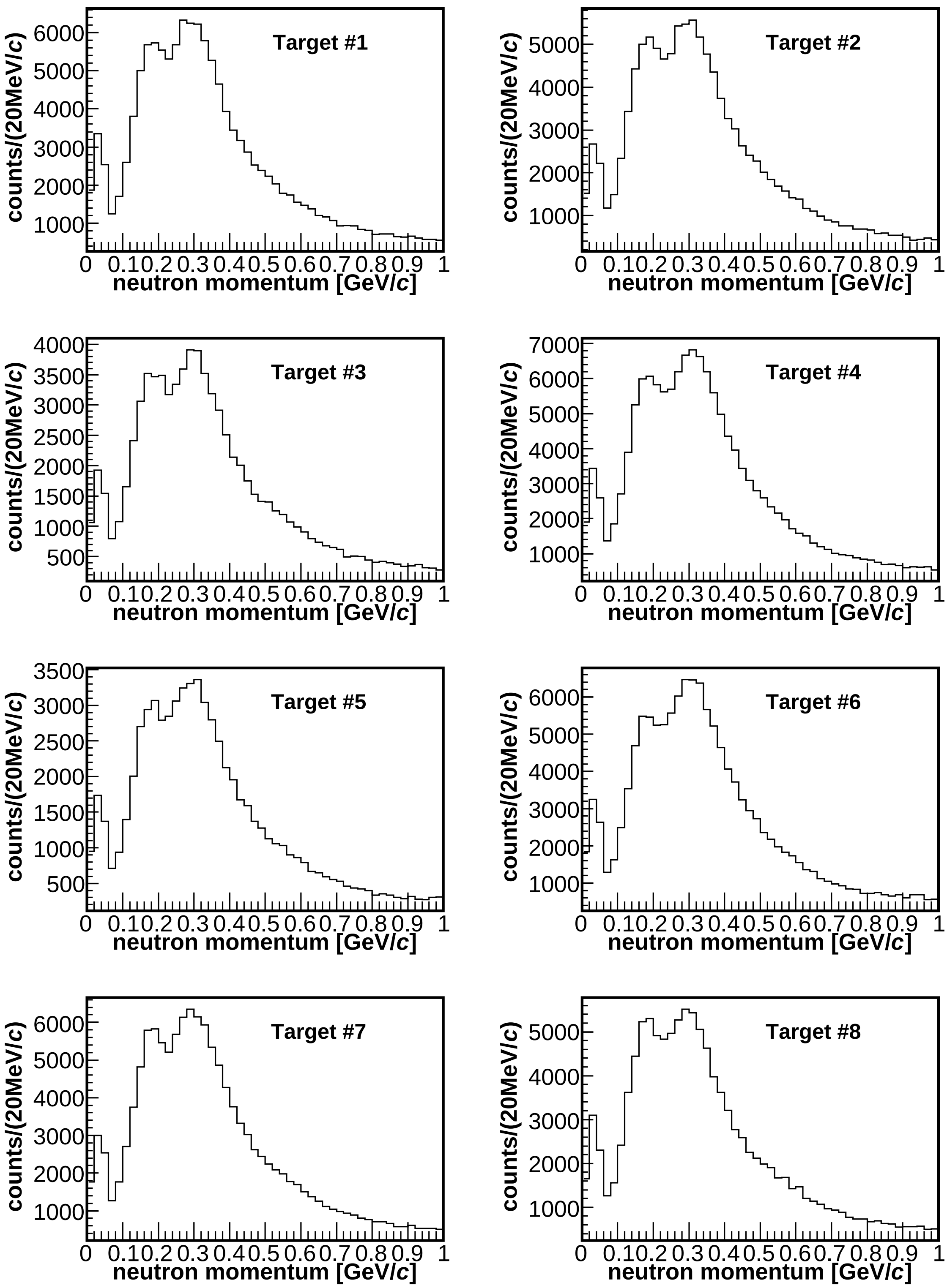

Figure 3.17: Momentum distribution of neutral particles for each target.

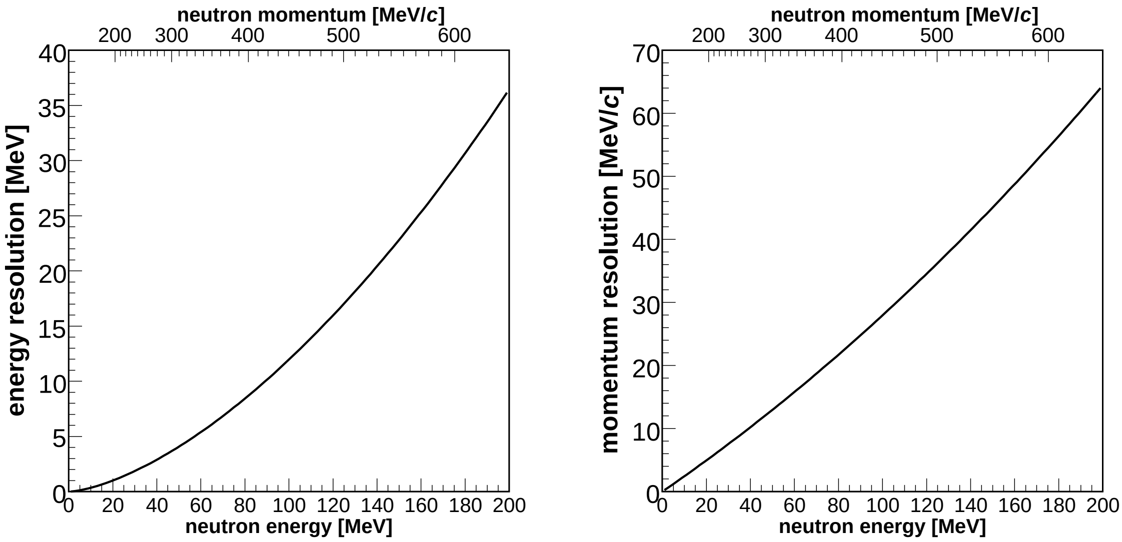

Figure 3.18: Energy resolution (left) and momentum resolution (right) for neutrons, assuming $\sigma(1/\beta) = 0.12$.

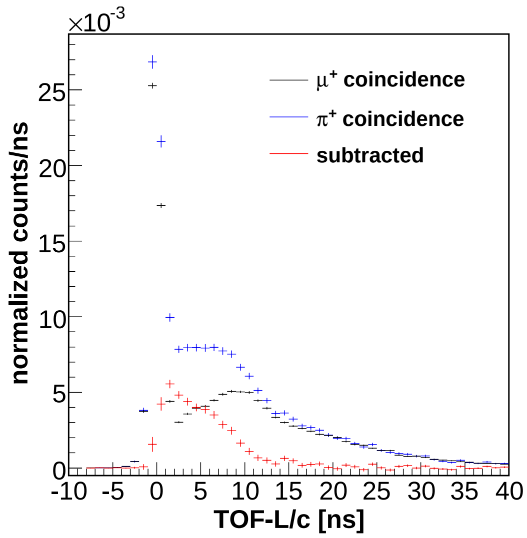

Figure 3.19: TOF-L/c distribution with μ^+ or π^+ coincidence.

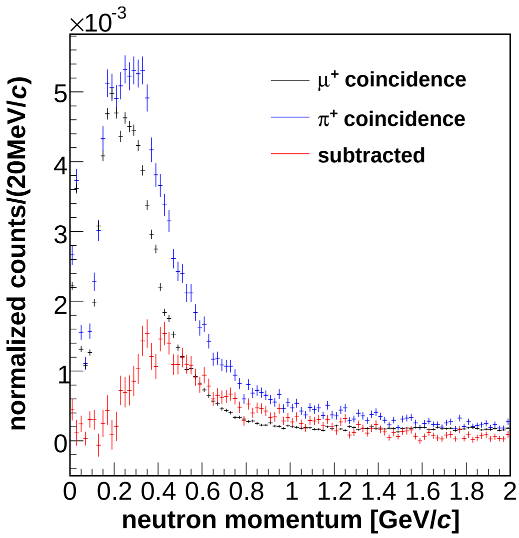

Figure 3.20: Neutron momentum distribution with μ^+ or π^+ coincidence.

Table 3.2: Estimation of the number of stopped $K^{\pm}$'s.

target	$N^{(\text{obs.})}(\mu^+_{\text{trig}})$	$\epsilon(\mu^+_{\text{trig}})$	$N(\text{stopped } K^+)$	$N(\text{stopped } K^-)$
#1	1.77×10^6	5.40×10^{-2}	3.16×10^7	$(3.16 \pm 0.41) \times 10^7$
#2	1.78×10^6	3.96×10^{-2}	4.49×10^7	$(4.49 \pm 0.58) \times 10^7$
#3	1.54×10^6	5.28×10^{-2}	2.92×10^7	$(2.92 \pm 0.99) \times 10^7$
#4	2.02×10^6	5.40×10^{-2}	3.74×10^7	$(3.74 \pm 0.49) \times 10^7$
#5	1.09×10^6	5.36×10^{-2}	2.03×10^7	$(2.03 \pm 0.26) \times 10^7$
#6	1.68×10^6	5.28×10^{-2}	3.17×10^7	$(3.17 \pm 0.41) \times 10^7$
#7	1.55×10^6	5.05×10^{-2}	3.07×10^7	$(3.07 \pm 0.40) \times 10^7$
#8	1.18×10^6	5.15×10^{-2}	3.44×10^7	$(3.44 \pm 0.45) \times 10^7$

multiplied. In other words, it is the number of reconstructed K^+'s stopping inside targets if the trigger condition in regard to TOFONE is removed.

The detection efficiency of μ^+_{trig} was not estimated from the total number of observed μ^+_{trig}'s, but the coincidence with at least one $\pi^{\pm}$ from a K^- vertex is required, so as to satisfy the trigger condition of TOFONE multiplicity, regardless of the existence of μ^+_{trig}. $\epsilon(\mu^+_{\text{trig}})$ was evaluated from the relationship $\epsilon(\mu^+_{\text{trig}}) = N^{(\text{obs.})}(\mu^+_{\text{trig}}\pi^{\pm})/N^{(\text{obs.})}(\pi^{\pm})$.

The estimated numbers of stopped $K^{\pm}$'s, together with $N^{(\text{obs.})}(\mu^+_{\text{trig}})$ and $\epsilon(\mu^+_{\text{trig}})$, are summarized in Table 3.2. While the numbers of stopped K^+'s and K^-'s in the same target are expected to be more or less similar, the recorded number was consistent within the error of $\pm 13\%$, except for target #3 (34%). This is partially because both K^+ and K^- are involved in the trigger conditions, and the distribution of secondary particles depends on the material where the K^- stopped. In addition, some of $K^{\pm}$'s can decay in flight before they stop. Therefore, the systematic error was estimated as $\pm 13\%$ except for target #3 and $\pm 34\%$ for target #3.

It is worthwhile to mention the capture rate of deuterium in heavy water target. According to the Fermi-Teller Z-law [87], the relative capture probability by an atom in the compound is proportional to its atomic number Z. On the contrary, a bubble chamber experiment measured the fraction of free hydrogen capture to be $3.2 \pm 0.4\%$ for propane (C_3H_8) [88], far from the prediction by the Z-law ($\sim 20\%$). A crude scaling leads the estimation of free deuterium absorption of $\sim 2\%$ for heavy water. This uncertainty is not considered in later discussions in deducing a branching ratio normalized to stopped K^- in ^{16}O, instead of heavy water, because it is much smaller than the systematic error on the number of stopped K^-'s in the target.

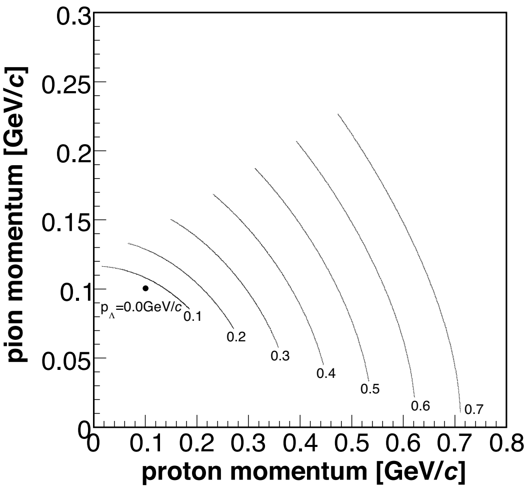

Figure 3.21: Momentum correlation for $\Lambda \to p + \pi^-$ decay with $p_\Lambda = 0.0$, 0.1, ..., 0.7 GeV/c.

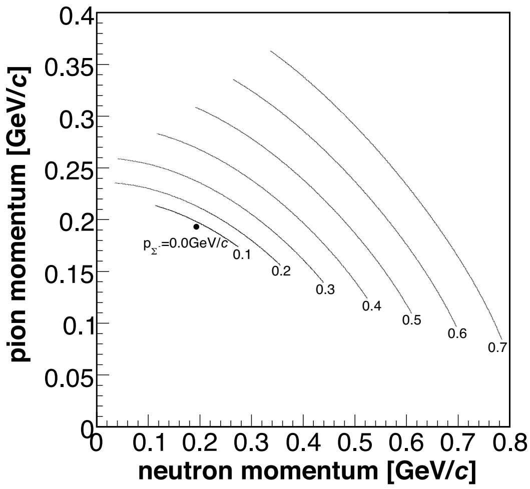

Figure 3.22: Momentum correlation for $\Sigma^- \to n + \pi^-$ decay with $p_{\Sigma^-} = 0.0$, 0.1, ..., 0.7 GeV/c.

3.5 Hyperon reconstruction

Hyperons were identified by reconstructing the invariant mass of its decay particles. Hyperons decay as [84]

$$\Lambda \to p + \pi^-, \quad (\text{B.R.} = 63.9 \pm 0.5\%) \tag{3.4}$$
$$\to n + \pi^0, \quad (\text{B.R.} = 35.8 \pm 0.5\%) \tag{3.5}$$
$$\Sigma^+ \to p + \pi^0, \quad (\text{B.R.} = 51.57 \pm 0.30\%) \tag{3.6}$$
$$\to n + \pi^+, \quad (\text{B.R.} = 48.31 \pm 0.30\%) \tag{3.7}$$
$$\Sigma^0 \to \Lambda + \gamma, \quad (\text{B.R.} = 100\%) \tag{3.8}$$
$$\Sigma^- \to n + \pi^-. \quad (\text{B.R.} = 99.848 \pm 0.005\%) \tag{3.9}$$

Because the FINUDA spectrometer can detect charged particles and neutrons, a Λ was identified in the decay mode of Eq. (3.4), in which all the decay particles are charged. A $\Sigma^\pm$ can be recognized by detecting a neutron and a $\pi^\pm$ in the decay mode of Eq. (3.7) and (3.9). A Σ^0, which decays in electromagnetic interaction (Eq. (3.8)), cannot be distinguished from a Λ in this approach.

3.5.1 Detection of Λ hyperons

Λ particles are to be emitted after either one-nucleon absorption ($K^- +$ "N" $\to \Lambda(\Sigma^0) + \pi$)

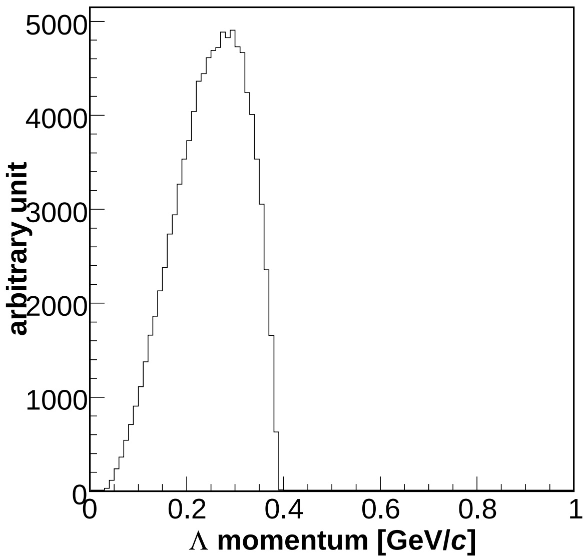

Figure 3.23: Λ momentum distribution from quasi-free one-nucleon absorption, estimated by a simulation.

or two-nucleon absorption ($K^- +$ "NN" $\rightarrow \Lambda(\Sigma^0) + N$). The momentum ($p_\Lambda$) of the emitted Λ distributes in two different regions; $p_\Lambda \lesssim 400\,\mathrm{MeV}/c$ for the former (see Fig. 3.23) and $400\,\mathrm{MeV}/c \lesssim p_\Lambda \lesssim 700\,\mathrm{MeV}/c$ for the latter (Fig. 4.22).

As seen in Fig. 3.21, the pions from the Λ decay are slower than $200\,\mathrm{MeV}/c$, and they were mainly detected as "short tracks" in the FINUDA spectrometer. The protons from the Λ decay were detected as "long tracks" in coincidence with "short track" π^-, except for those emitted from very slow Λ's below about $300\,\mathrm{MeV}/c$. Please note that the proton momentum is very close to the original Λ momentum because of the decay kinematics (cf. Fig. 3.21).

In this analysis, only the proton with a long track was used, while the pion can be either a long or short track, in order to have a good resolution of the invariant mass $\mathrm{IM}(p\pi^-)$ and the momentum p_Λ, As a result, we have less sensitivity for the Λ's from one-nucleon absorption due to the momentum threshold $\sim 300\,\mathrm{MeV}/c$, while we have good sensitivity for the Λ's from the two-nucleon absorption.

Invariant mass distribution and momentum distribution of Λ

The invariant mass distributions for all the detected $p\pi^-$ pairs from stopped K^- vertices are shown for all the targets in Fig. 3.24. The peaks centered at the right Λ mass (m_Λ) are clearly seen. The signal region was defined as $|\mathrm{IM}(p\pi^-) - m_\Lambda| < 4\,\mathrm{MeV}/c^2$, where $\mathrm{IM}(p\pi^-)$ is the invariant mass of a $p\pi^-$ pair.

For selected $p\pi^-$ pairs, the Λ momentum distribution for each target is shown in Fig. 3.25. A combinatorial background of $p\pi^-$ pairs was estimated by selecting the events in the side-band region $5\,\mathrm{MeV}/c^2 < |\mathrm{IM}(p\pi^-) - m_\Lambda| < 9\,\mathrm{MeV}/c^2$. The background subtracted spectrum is also shown in Fig. 3.25 in red.

Mass resolution, geometrical acceptance and momentum resolution

The mass resolution, geometrical acceptance, and momentum resolution for Λ were estimated with a Monte Carlo simulation, which takes accounts of all the detector geometry, track reconstruction, and momentum resolutions for pions and protons as described in Sec. 3.2.2. Figure 3.26 shows the obtained invariant mass resolution (in σ) of $p\pi^-$ pairs as a function of Λ momentum. It is almost constant ($\sim 2\,\mathrm{MeV}/c^2$), in this Λ momentum range, and is consistent with the observed resolution of $1.9\,\mathrm{MeV}/c^2$.

The geometrical acceptance of Λ is shown in Fig. 3.27. It is an increasing function of the Λ momentum, rising from $300\,\mathrm{MeV}/c$.

The resolution of the Λ momentum, obtained by the vector sum of the momentum of the proton and the pion, is shown in Fig. 3.28. Generally, the resolution of a pion with a "short track" is worse than that of a proton with a "long track", and it dominates the overall resolution. As plotted in Fig. 3.29, the kinetic energy resolution is almost independent of the Λ momentum, and is around $4\,\mathrm{MeV}$.

Λ vertex cut

A Λ vertex was first defined as the crossing point of proton and pion tracks in the $r\phi$-plane. Then, the z coordinate for each track at this Λ vertex is obtained. Figure 3.30 shows a distribution of distance in z direction between two z coordinates. The tolerance for Λ candidate ($|\mathrm{IM}(p\pi^-) - m_\Lambda| < 2\,\mathrm{MeV}/c^2$) is very close to 0, while that for an irrelevant pair ($|\mathrm{IM}(p\pi^-) - m_\Lambda| > 10\,\mathrm{MeV}/c^2$) is broadly distributed. Hereafter, the z-tolerance between 1 mm is accepted for the Λ vertex cut, in order to improve the signal-to-noise ratio. The survival rate after the Λ vertex cut was estimated to be 0.6 above $400\,\mathrm{MeV}/c$ from Fig. 3.27.

3.5.2 Detection of Σ^- hyperons

A fast Σ^- ($\sim 500\,\mathrm{MeV}/c$) is to be emitted from the following two-nucleon absorption process:

$$K^- + \text{“}pn\text{”} \rightarrow \Sigma^- + p. \tag{3.10}$$

with a proton with a similar momentum in back-to-back. The Σ^- was detected through the decay into $n + \pi^-$. Different from the Λ detection via $p + \pi^-$, we need to take accounts of neutron background as already discussed in Sec. 3.3. A selection of back-to-back pairs of a Σ^- and a proton would reduce accidental neutron backgrounds.

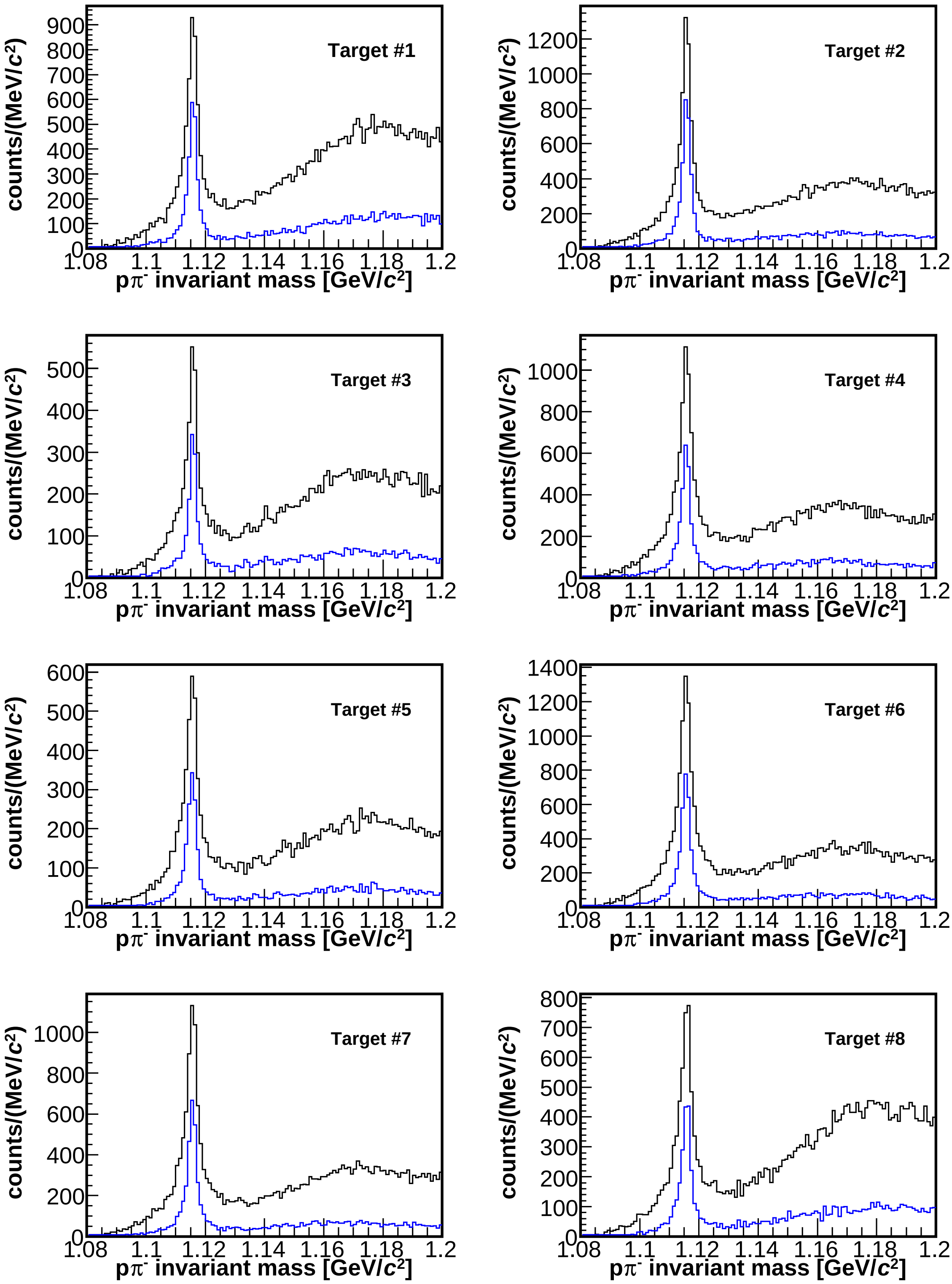

Figure 3.24: $p\pi^-$ invariant mass spectrum. The blue histogram is the result for the Λ vertex cut.

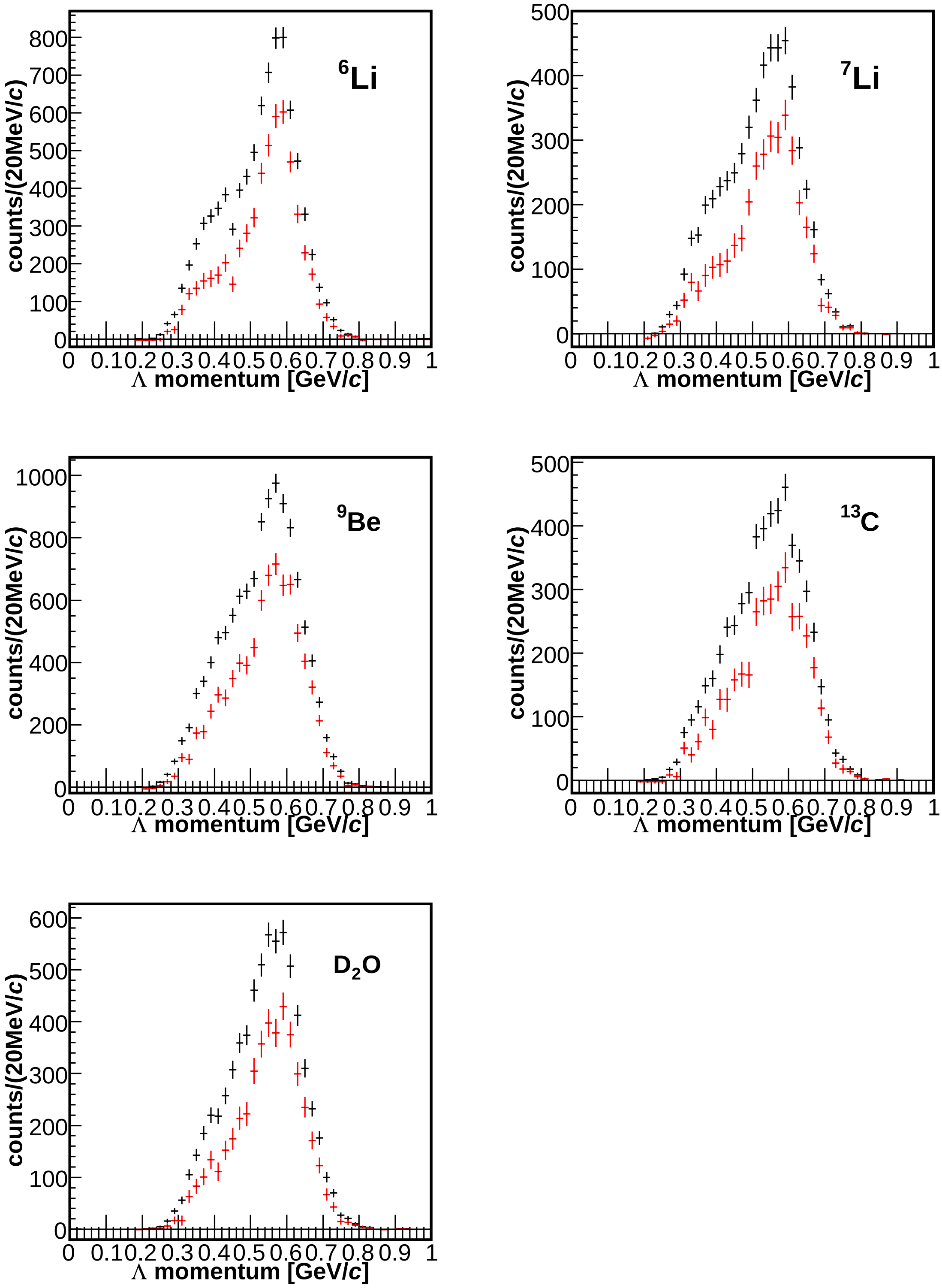

Figure 3.25: Momentum distribution of Λ. Sideband-subtracted one is shown in the red histogram.

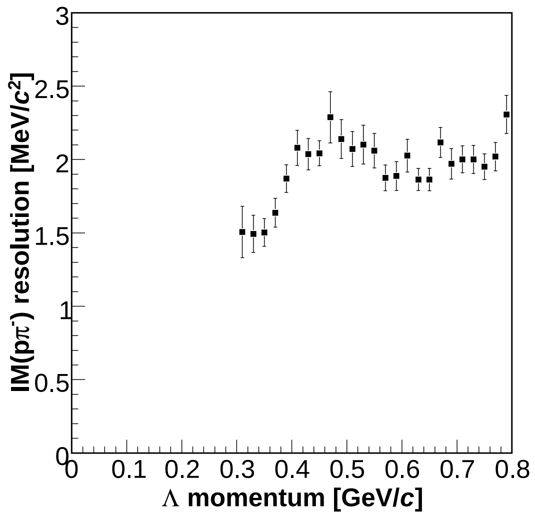

Figure 3.26: Invariant-mass resolution of $p\pi^-$ pairs from Λ decay versus Λ momentum.

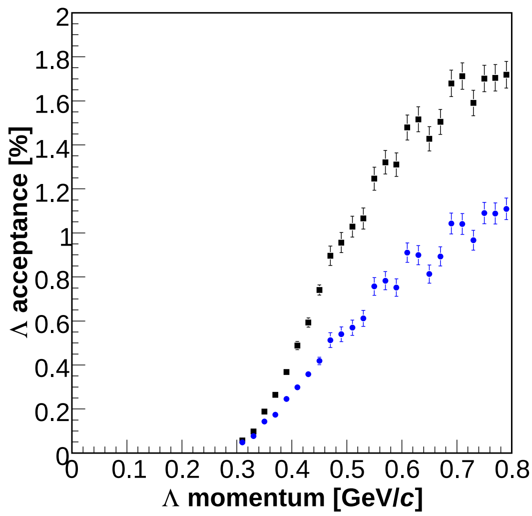

Figure 3.27: Geometrical acceptance of Λ. The acceptance with Λ vertex cut applied is shown in the blue graph.

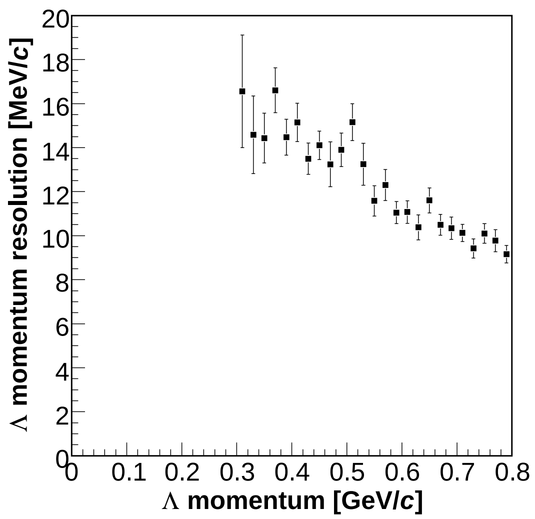

Figure 3.28: Momentum resolution for Λ.

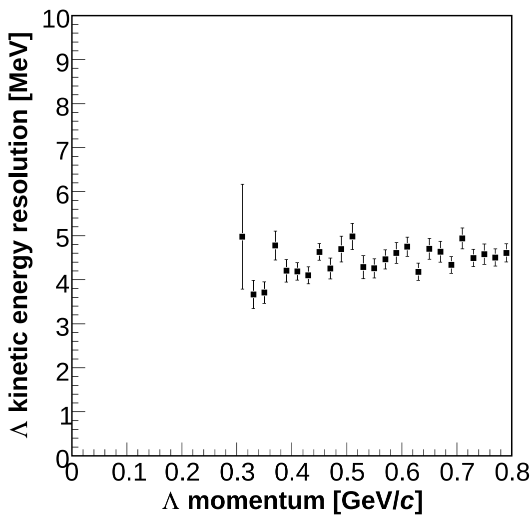

Figure 3.29: Kinetic energy resolution for Λ.

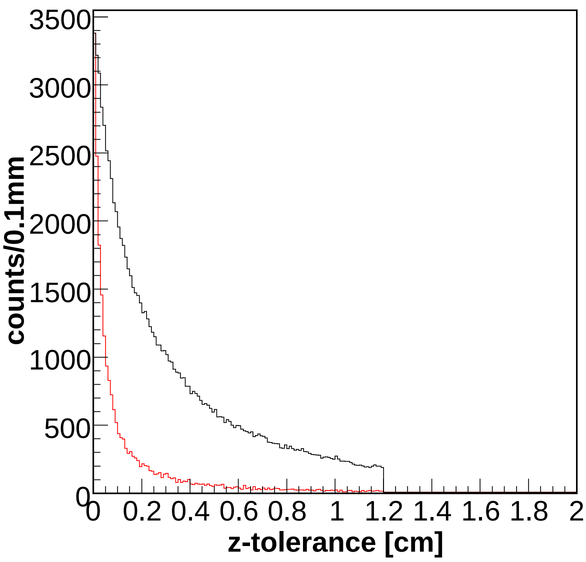

Figure 3.30: z-tolerance for Λ vertex candidates of $p\pi^-$ pairs. The red histogram is for the signal region in the $p\pi^-$ invariant mass spectrum ($|\mathrm{IM}(p\pi^-) - m_\Lambda| < 2\,\mathrm{MeV}/c^2$) and the black histogram is for the background region ($|\mathrm{IM}(p\pi^-) - m_\Lambda| > 10\,\mathrm{MeV}/c^2$), normalized to the signal distribution. Note that a candidate with the tolerance $> 1.2\,\mathrm{cm}$ is discarded.

Invariant mass distribution of Σ^-

Figure 3.31 shows the target-by-target invariant mass spectra for $n\pi^-$ pairs, in coincidence with fast protons ($> 400\,\mathrm{MeV}/c$) in the opposite direction to the pair ($\cos\theta(p\Sigma^-) < -0.9$). The Σ^- peaks are clearly observed around its PDG mass ($1.197\,\mathrm{GeV}/c^2$). The mass resolution was evaluated for a histogram summed over all the targets (Fig. 3.32) as $\sigma = 3.4\pm0.3\,\mathrm{MeV}/c^2$.

Mass resolution, geometrical acceptance and momentum resolution

The mass resolution, geometrical acceptance, and momentum resolution for Σ^- were estimated with the same Monte Carlo simulation as for Λ. In order to identify Σ^- hyperons with as less background as possible, completely back-to-back pairs of a Σ^- and a proton were generated. Then, the direction of a Σ^- candidate, as a pair of a neutron and a negative pion, could be restricted very tightly ($\cos\theta(\Sigma^- p) < -0.998$ or $\theta > 176.4°$).

After the angular cut, the invariant mass resolution was obtained as shown in Fig. 3.33 as a function of Σ^- momentum. It should be noted that it is just slightly worse than that for Λ. This is because the neutrons from Σ^- are moderately slow (see Fig. 3.22), and the resolution for a slow neutron is much better than that for a fast neutron. The geometrical acceptance of Σ^- hyperons, taking into account the detection efficiency of neutrons by TOFONE and

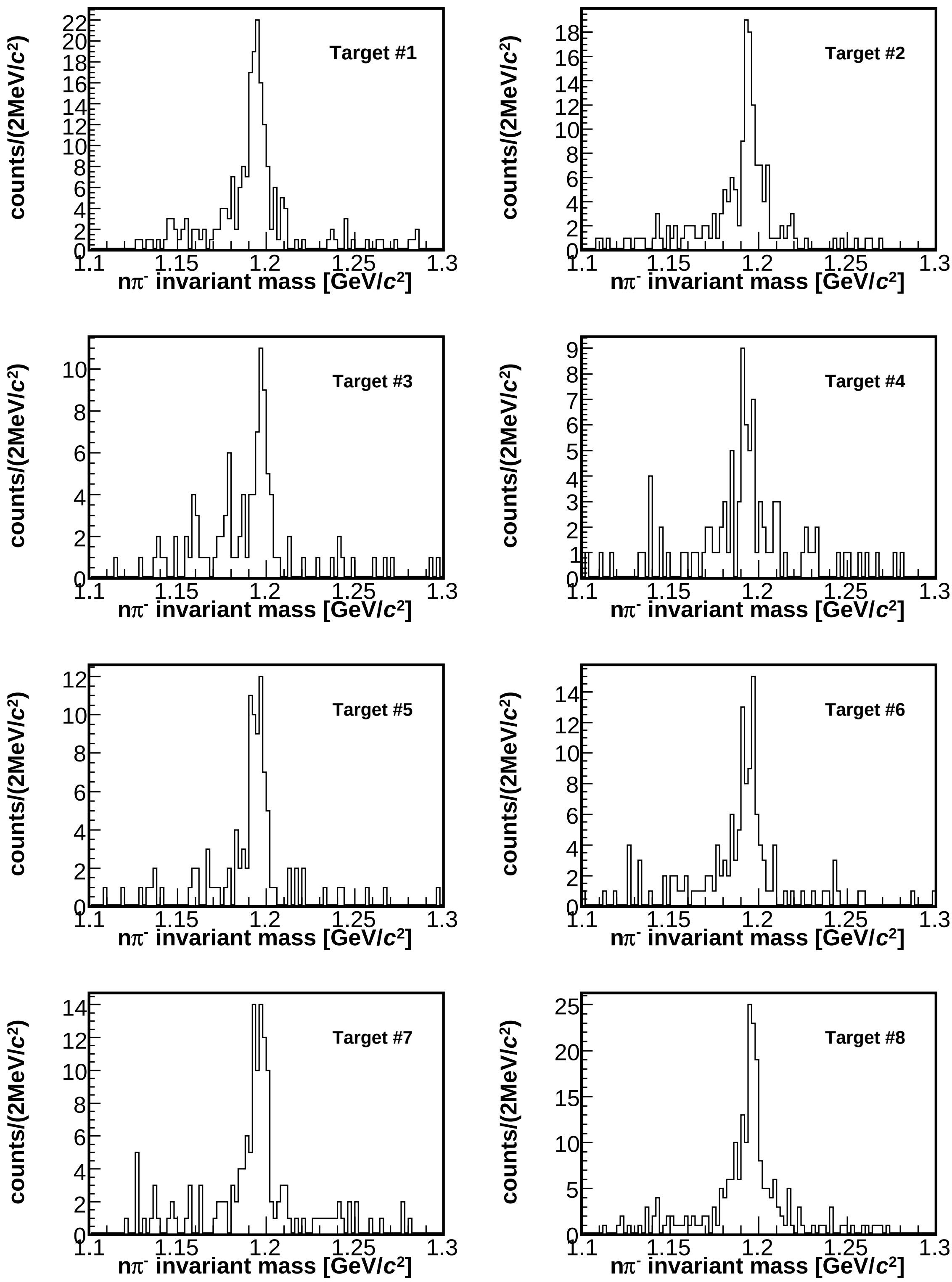

Figure 3.31: Invariant mass spectrum of $n\pi^-$ pairs for each target, in coincidence with a back-to-back proton.

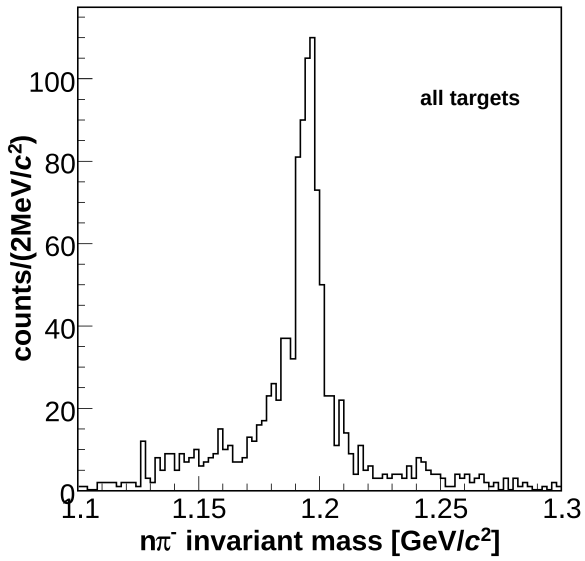

Figure 3.32: Invariant mass spectrum of $n\pi^-$ pairs for all the targets, in coincidence with a back-to-back proton.

the reconstruction efficiency of pions, is shown in Fig. 3.34. The momentum resolution and kinetic energy resolution are also shown in Figs. 3.35 and 3.36.

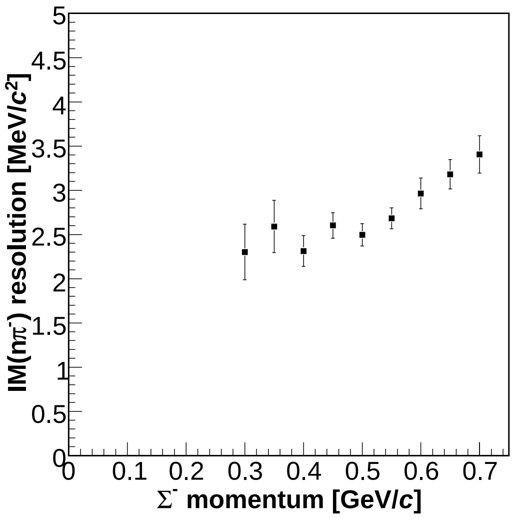

Figure 3.33: Invariant-mass resolution of $n\pi^-$ pairs from Σ^- decay versus Σ^- momentum.

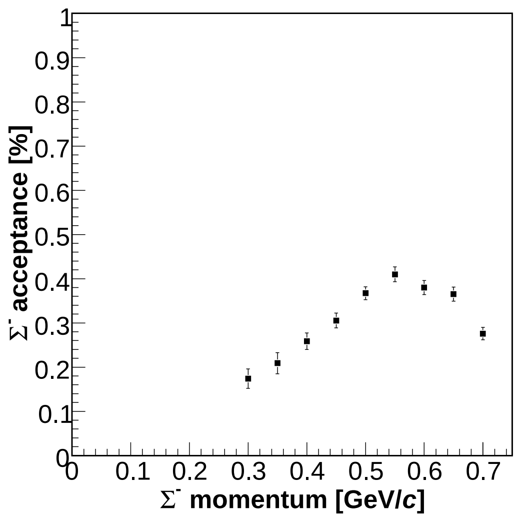

Figure 3.34: Geometrical acceptance of Σ^-.

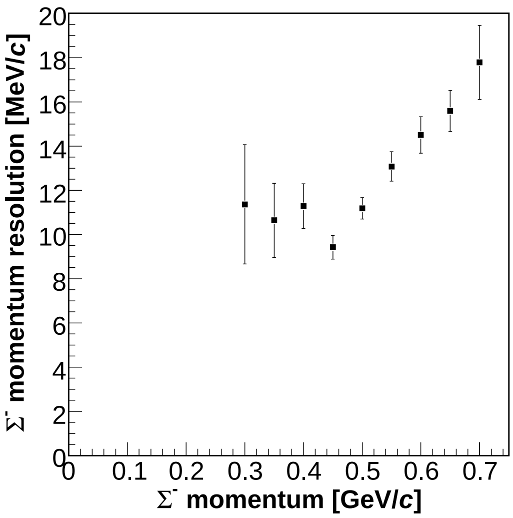

Figure 3.35: Momentum resolution for Σ^-.

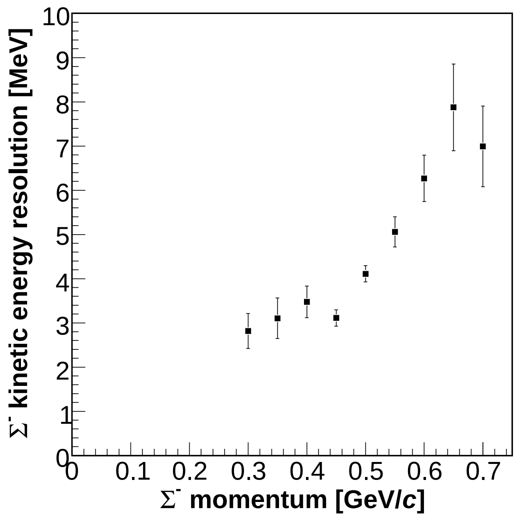

Figure 3.36: Kinetic energy resolution for Σ^-.

Chapter 4

Results

4.1 Fast Λ hyperon from kaon absorption

As shown in Sec. 3.5.1, Λ's above $\sim 300\,\mathrm{MeV}/c$ could be detected. The acceptance-corrected momentum distribution can be obtained by dividing the number of observed Λ's by the acceptance at the corresponding momentum. In order to avoid the ambiguity on the trigger efficiency, which strongly depends on the existence of other particles both from K^- and K^+ vertices, the μ^+_{trig} coincidence was required. Then, the yield as a function of momentum p_Λ is described as:

$$R(p_\Lambda) = \frac{N_{\Lambda\mu^+_{\mathrm{trig}}}(p_\Lambda)}{\epsilon_\Lambda(p_\Lambda)\epsilon_p^{(\mathrm{long})}\epsilon_{\pi^-}^{(\mathrm{short})}N_{\mu^+_{\mathrm{trig}}}}, \tag{4.1}$$

where $N_{\Lambda\mu^+_{\mathrm{trig}}}(p_\Lambda)$ is the number of Λ's with the momentum p_Λ in coincidence with μ^+_{trig}, ϵ_Λ is the geometrical acceptance discussed in Sec. 3.5.1, and $N_{\mu^+_{\mathrm{trig}}}$ is the number of observed μ^+_{trig}'s.

From the momentum distribution in coincidence with μ^+ (Fig. 4.1), the acceptance-corrected distribution was obtained as shown in Fig. 4.2. The yield above $p_\Lambda > 400\,\mathrm{MeV}/c$ for each target is summarized in Table 4.1. The yield, together with the yields of Λp and Λn, is discussed in Sec. 4.5.

They can be compared with the bubble chamber data for ^{4}He by Katz *et al.* [67] (Table. 1.1), where the branching ratio of the final states $\Lambda(pnn)$[1] and $\Sigma^0(pnn)$ was measured to be $11.7 \pm 2.4\%$. They also showed the Λ momentum distribution for the $\Lambda(pnn)$ or $\Sigma^0(pnn)$ final state, as shown in Fig. 4.3. Although the statistics was poor, the histogram shows that only the half (11/22) of observed Λ's was above $400\,\mathrm{MeV}/c$. The yield of fast Λ's in the present FINUDA experiment is consistent with their result. While the absolute calibration of a yield with a well-known process is difficult in case of the FINUDA experiment, the validity of the calibration could be checked by comparison with the ^{4}He data.

[1] (pnn) indicates the three particles are either bound ($d+n$ or t) or unbound ($p+n+n$).

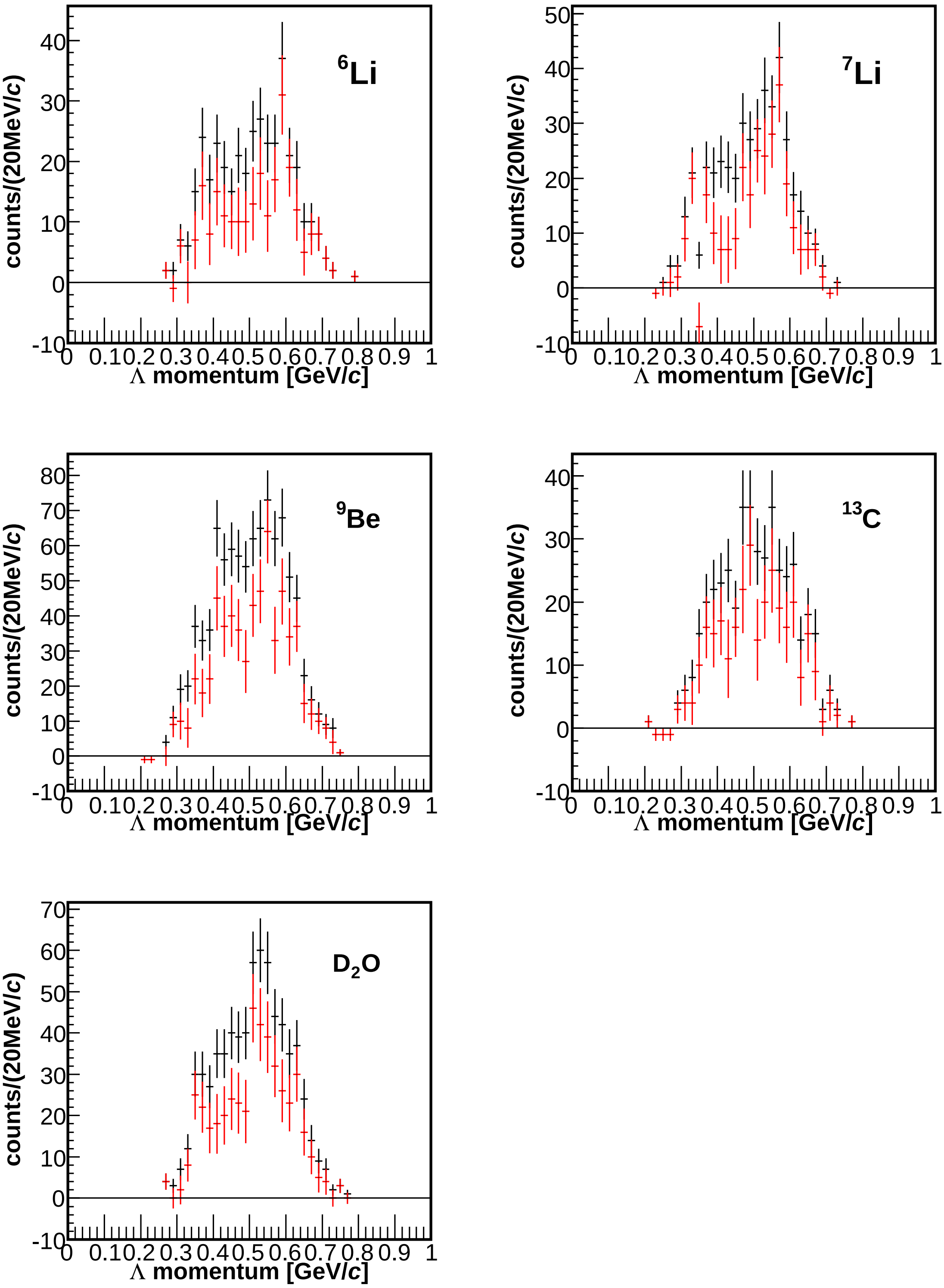

Figure 4.1: Momentum distribution of Λ, in coincidence with μ^+. Sideband-subtracted one is shown in the red histogram.

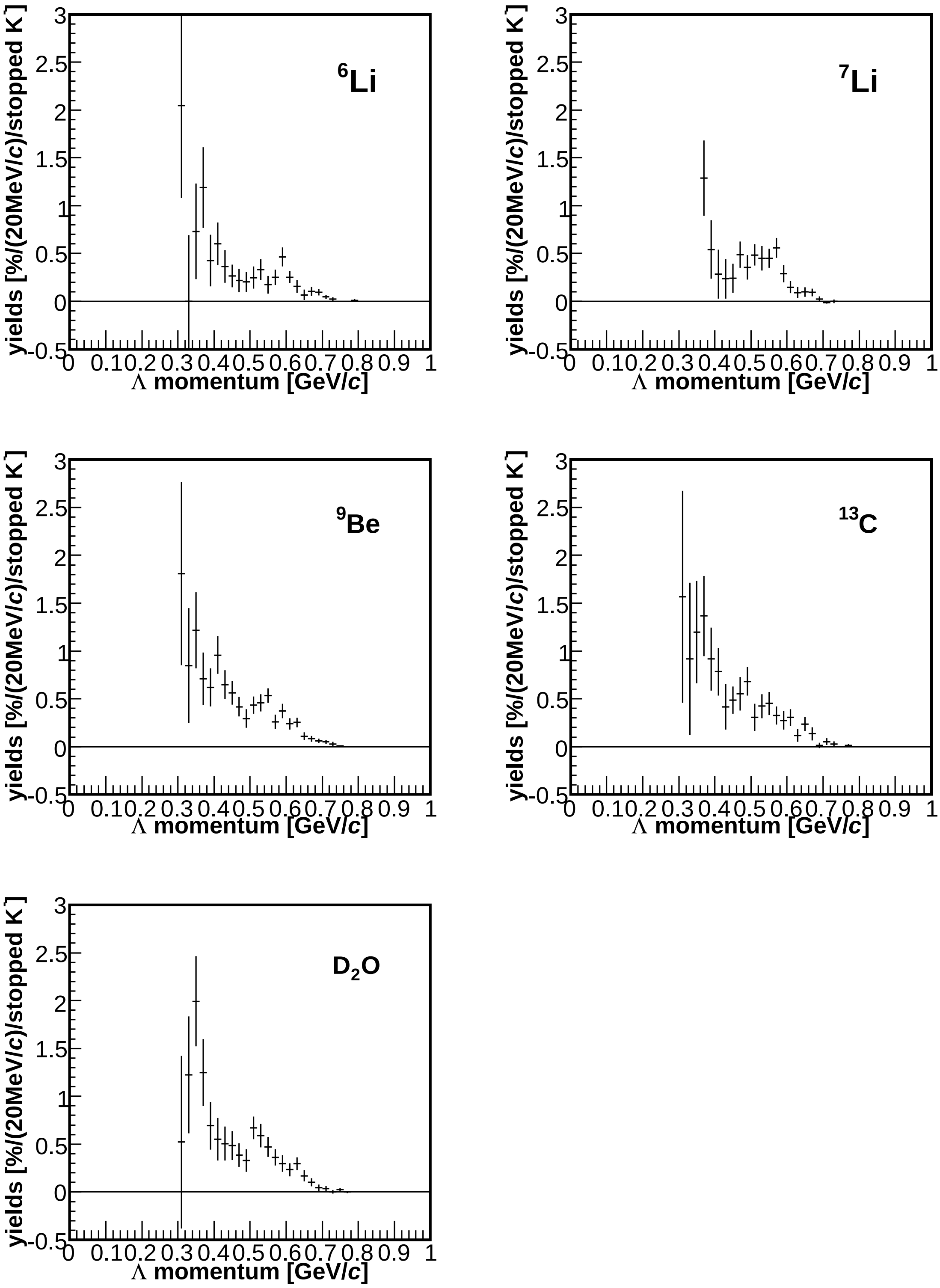

Figure 4.2: Acceptance-corrected momentum distribution of Λ.

Table 4.1: Yield of Λ from K^- absorption above 400 MeV/c.

target	yield (%)
^{6}Li	$3.9 \pm 0.4_{\mathrm{stat}} \pm 0.3_{\mathrm{syst}}$
^{7}Li	$4.3 \pm 0.5_{\mathrm{stat}} \pm 0.3_{\mathrm{syst}}$
^{9}Be	$5.8 \pm 0.4_{\mathrm{stat}} \pm 0.4_{\mathrm{syst}}$
^{13}C	$5.6 \pm 0.5_{\mathrm{stat}} \pm 0.4_{\mathrm{syst}}$
^{16}O	$5.5 \pm 0.5_{\mathrm{stat}} \pm 0.4_{\mathrm{syst}}$

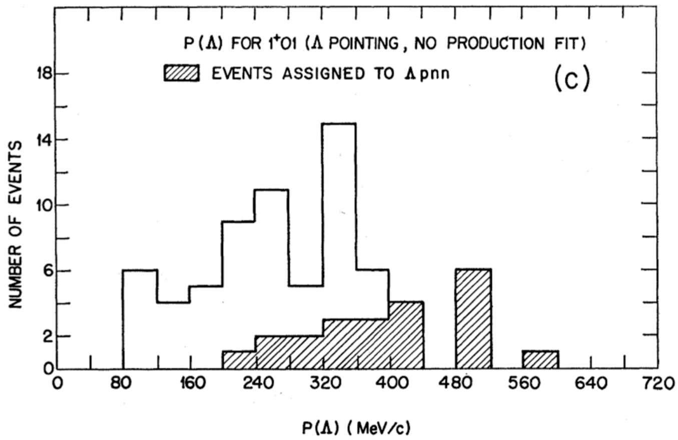

Figure 4.3: Λ momentum distribution for $\pi^0\Lambda(pnn)$ (white) and $\Lambda(pnn)$ (hatched) final state after kaon absorption in ^{4}He. Taken from [67].

4.2 Observation of correlated YN pairs

As shown in the previous section, a number of Λ's with their momenta larger than 400 MeV/c were observed. It is hard to assume that they would come from one-nucleon absorption ($K^- +$ "N" $\rightarrow Y + \pi$), whose Q value is only ~ 170 MeV for $Y = \Lambda$, and ~ 100 MeV for $Y = \Sigma$. Then it is naturally explained if they would originate from non-mesonic absorption with the Q value increased by the mass of a pion. As described in Chapter 1, the existence of such non-mesonic absorption had been known in 1960's, with the branching ratio of $\sim 20\%$, almost constant for various kinds of nuclei.

The simplest process among non-mesonic absorption would be two-nucleon absorption, where a kaon is absorbed by a pair of nucleons in a nucleus. This process yields a characteristic back-to-back pair of hyperon and nucleon with high momenta. There may exist three-nucleon (or more) absorption processes. In this case, the emitted hyperon shares kinetic energy with many nucleons, and a hyperon and a nucleon in the final state may show a weaker back-to-back correlation.

Three kinds of final states from the following absorption processes were investigated in this thesis:

$$K^- + \text{"}pp\text{"} \to \Lambda + p, \tag{4.2}$$

$$K^- + \text{"}pn\text{"} \to \Lambda + n, \tag{4.3}$$

$$K^- + \text{"}pn\text{"} \to \Sigma^- + p. \tag{4.4}$$

4.2.1 Correlation between hyperon and nucleon

Angular correlations between a hyperon and a nucleon were analyzed first. A back-to-back correlation was expected for the YN pairs ($\Sigma^- p$, Λn, and Λp) from two-nucleon absorption.

Next, the kinematics of quasi-free two-nucleon absorption (QF-TNA) was examined. The energy conservation law for the QF-TNA:

$$K^- + {}^{A}Z \to Y + N + {}^{A-2}Z', \tag{4.5}$$

where $Z' = Z - 2$ for Λp pairs, and $Z' = Z - 1$ for Λn or $\Sigma^- p$ pairs, can be expressed as

$$M(K^-)c^2 + M({}^{A}Z)c^2 = E_Y + E_N + E({}^{A-2}Z'). \tag{4.6}$$

Since the momentum of the recoil nucleus is very small (a few hundred MeV/c, see Fig. 4.19, 4.20, and 4.21), its kinetic energy can be neglected. Then, the following relationship should be hold:

$$\begin{aligned} E_Y + E_N &\simeq M(K^-)c^2 + M({}^{A}Z)c^2 - M({}^{A-2}Z')c^2 \\ &= M(K^-)c^2 + M(NN)c^2 - S_{NN}({}^{A}Z) - Ex({}^{A-2}Z'), \end{aligned} \tag{4.7}$$

where NN denotes two protons (a proton and a neutron) for Λp (Λn or $\Sigma^- p$) pairs, S_{NN} means the separation energy of two nucleons, and Ex is the excitation energy of the residual nucleus. The energy sum $E_{\text{sum}} = E_Y + E_N$ is largest when the residual nucleus is in the ground state. The kinematical threshold is listed for each nucleus in Table 4.2.

In this thesis, the energy sum region between 2.30 and 2.38 GeV/c is regarded as “quasi-free”, independent of the target and the final state.

4.3 Correlated Λp pairs

First of all the three combinations, the correlation of Λp pairs was investigated.

Table 4.2: Kinematical threshold for energy sum of hyperon and nucleon.

	$\Lambda + p$		$\Lambda + n$ and $\Sigma^- + p$	
target nucleus	residual nucleus	threshold [GeV]	residual nucleus	threshold [GeV]
^{6}Li	^{4}H	2.345	^{4}He	2.368
^{7}Li	^{5}H	2.335	^{5}He	2.360
^{9}Be	^{7}He	2.342	^{7}Li	2.353
^{13}C	^{11}Be	2.340	^{11}B	2.351
^{16}O	^{14}C	2.349	^{14}N	2.349

4.3.1 Opening angle distribution

Figure 4.4 shows the opening angle distribution between observed pairs of Λ and proton. A back-to-back component was found to be dominant for every target, with a very few non-back-to-back events. Back-to-back events with $\cos\theta(\Lambda p) < -0.80$ were selected for the correlated Λp pairs. For comparison, the dependence of the angular cut was studied by changing the cut as $\cos\theta(\Lambda p) < -0.90$ and -0.95, which are applied for $\Sigma^- p$ and Λn pairs as described later.

4.3.2 Energy sum distribution and momentum distribution

The energy sum distribution for the correlated Λp pairs is shown in Fig. 4.5. The distribution does not show any narrow peak structure near the threshold. Because the energy resolution is as good as $\sim 5\,\mathrm{MeV}$, a narrow enhancement is expected to be observed experimentally if exists.

The present data are consistent with the results of the first data taking, and the energy sum distribution does not exhibit an apparent contribution of QF-TNA as a narrow peak.

The momentum correlation of Λ and proton (Fig. 4.6) is also distributed broadly. No concentration in the region of QF-TNA, indicated by two dashed lines ($E_\Lambda + E_p = 2.30$, $2.38\,\mathrm{GeV}$), is seen.

4.3.3 Acceptance-corrected energy sum distribution

The acceptance correction was carried out event by event. The acceptance of each Λp pair was estimated from a Monte Carlo simulation where a pair of Λp with the same momenta and opening angle from the K^- vertex was generated isotropically.

The corrected energy sum distribution is shown in Fig. 4.7. A further constraint of $p_p > 300\,\mathrm{MeV}/c$, $p_\Lambda > 400\,\mathrm{MeV}/c$, in addition to the angular cut of $\cos\theta(\Lambda p) < -0.80$, was

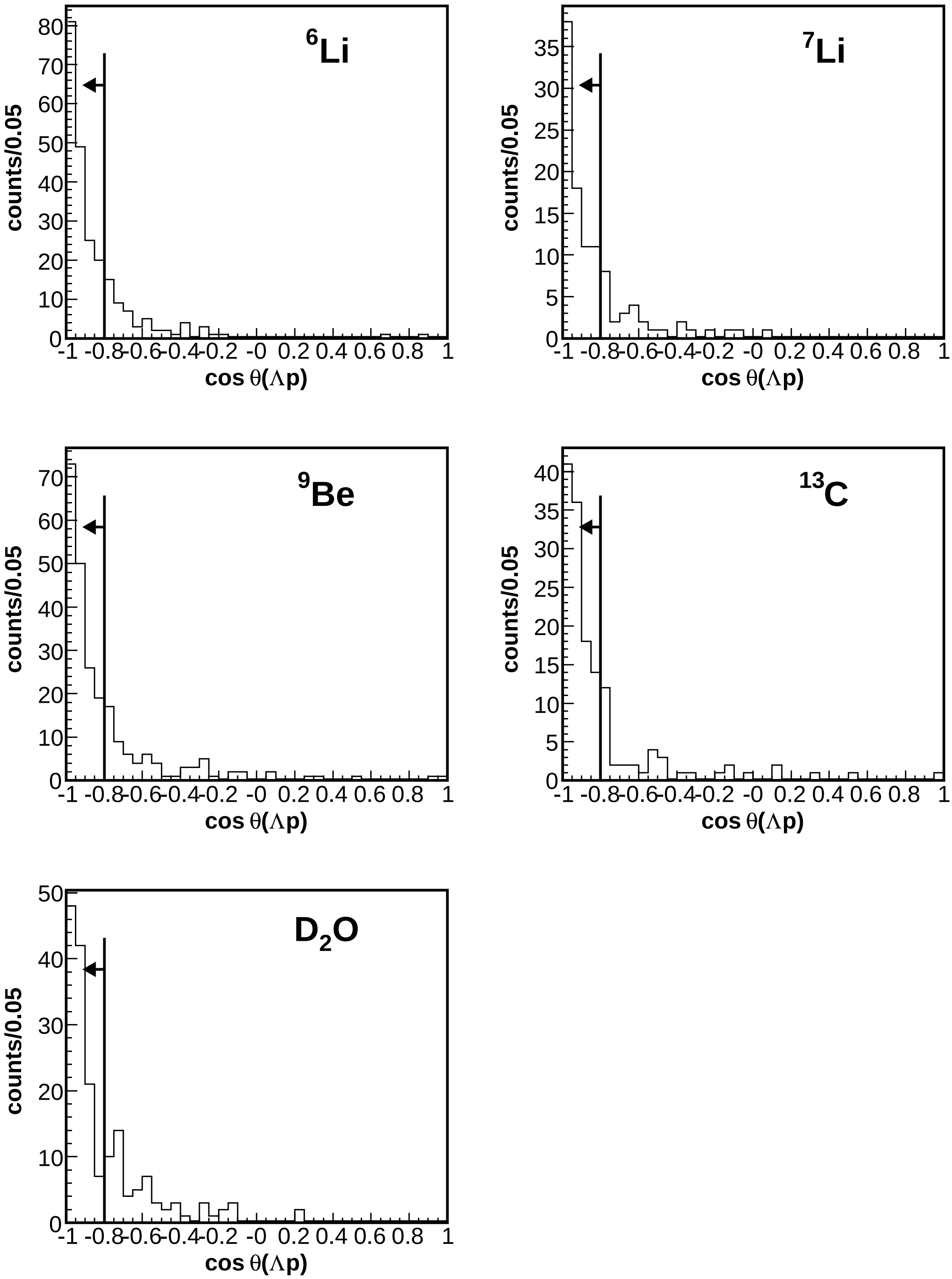

Figure 4.4: Opening angle between a Λ and a proton.

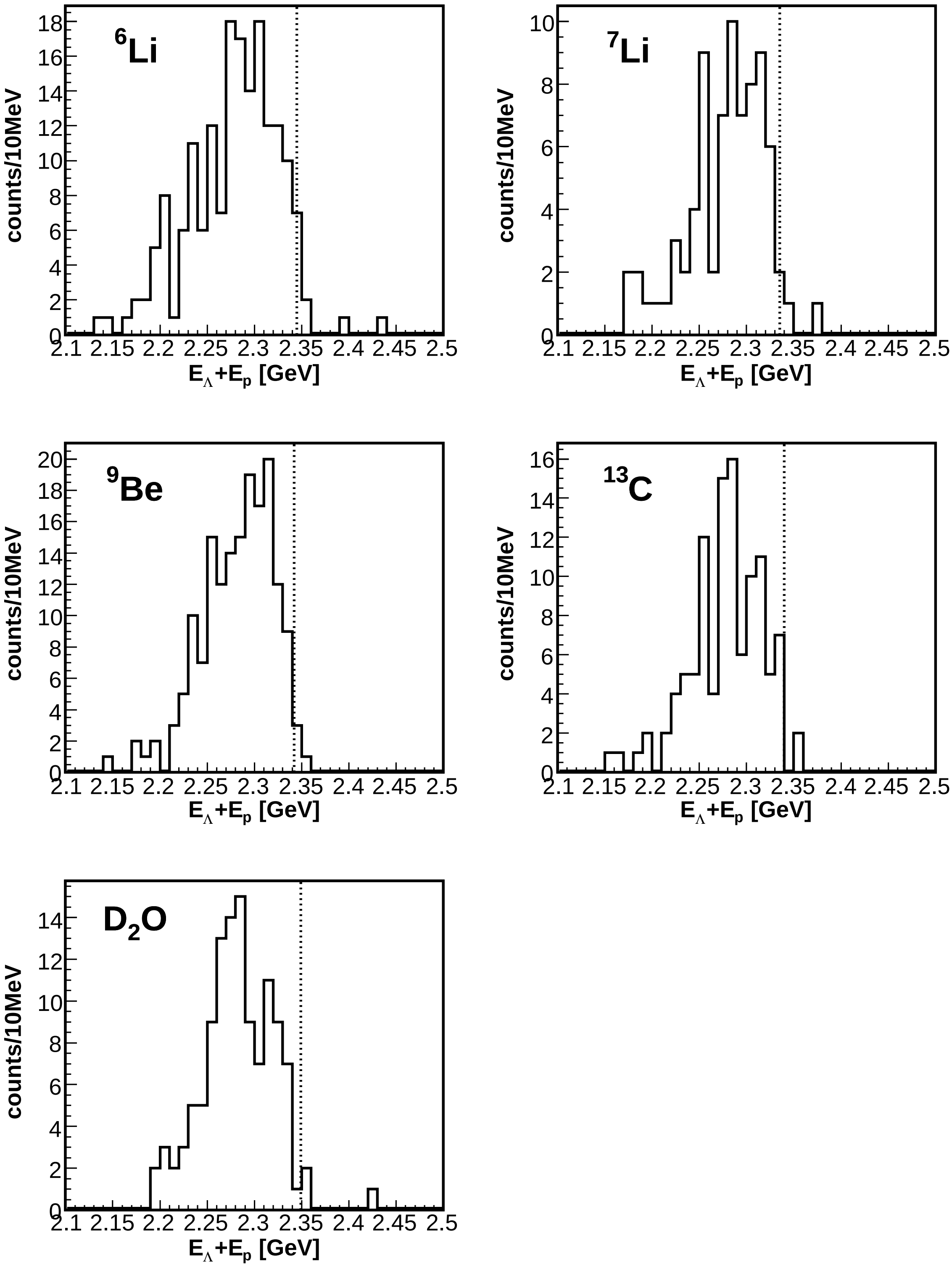

Figure 4.5: Energy sum of back-to-back Λ and proton. The kinematical threshold is indicated by a vertical line.

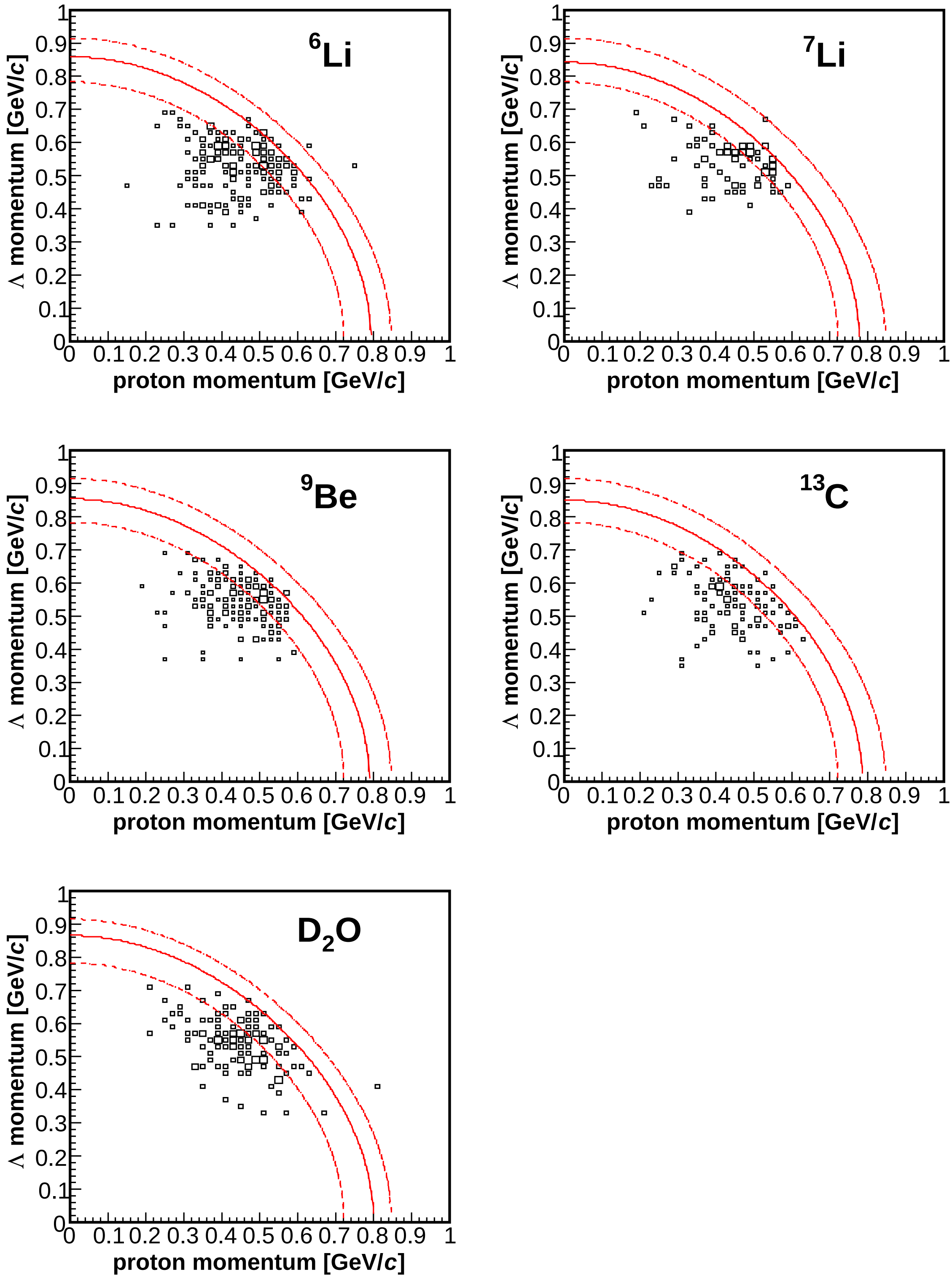

Figure 4.6: Momentum correlation for back-to-back Λ and proton pairs. The solid line is the threshold, and the dashed lines corresponds to the energy sum of 2.30 and 2.38 GeV.

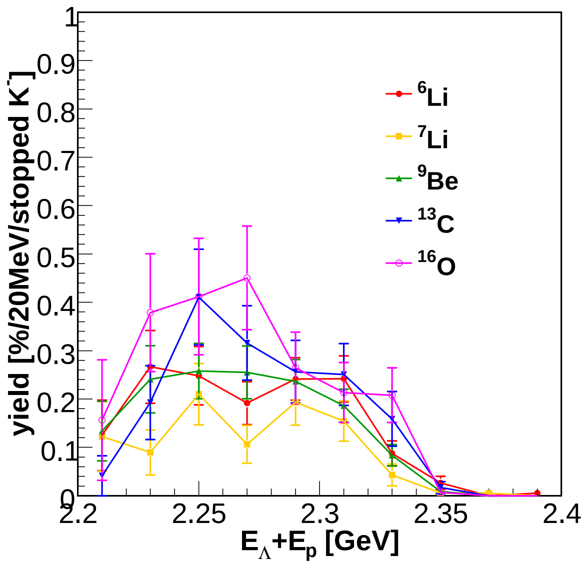

Figure 4.7: Energy sum distribution of back-to-back Λp pairs, corrected for acceptance. Events with $p_p > 300\,\mathrm{MeV}/c$, $p_\Lambda > 400\,\mathrm{MeV}/c$, and $\cos\theta(\Lambda p) < -0.80$ are selected.

applied to reduce the systematic error.

Table 4.3 summarizes the integrated yield for the back-to-back Λp events with the event selection shown above. The yield in the near-threshold region between 2.30 and 2.38 GeV is also shown and are compared with those for Λn and $\Sigma^- p$ in Sec. 4.4.5.

The energy sum distribution for a different opening angular cut has been examined, in order to check whether the distribution has a strong dependence on the cut or not. Figure 4.8 shows the energy sum distributions for $\cos\theta < -0.90$ and -0.95. While an event with a smaller recoil is enhanced by a tight angular cut, the observed energy sum distribution does not exhibit a remarkable difference from Fig. 4.7. The integrated yield was also estimated in the same way, as summarized in Tables 4.4 and 4.5. It also shows the ratio of the yield in the near-threshold region to the total yield is almost constant within errors, independent of the angular cut. Note that the systematic error on the ratio is almost cancelled out, because that for a yield is related to the normalization, mainly from the uncertainty of the number of stopped K^-'s.

It was also found that the energy sum distribution and the ratio of the near-threshold yield ($R_{\mathrm{QF}}/R_{\mathrm{total}}$) have little A-dependence.

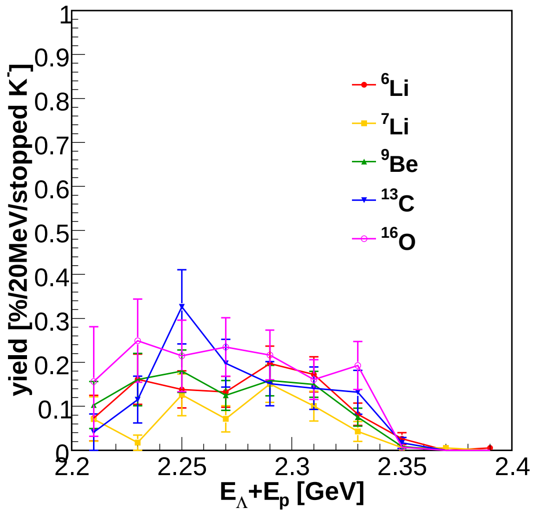

Figure 4.8: Energy sum distribution of back-to-back Λp pairs, corrected for acceptance. Events with $p_p > 300\,\mathrm{MeV}/c$, $p_\Lambda > 400\,\mathrm{MeV}/c$, and $\cos\theta(\Lambda p) < -0.90$ (left) or -0.95 (right) are selected.

Table 4.4: Yield of correlated Λp events within the event selection ($\cos\theta < -0.90$).

target	total yield (R_{total}) (%)	yield near threshold (R_{QF})(%)	$R_{\mathrm{QF}}/R_{\mathrm{total}}$
^{6}Li	$1.2 \pm 0.1_{\mathrm{stat}} \pm 0.2_{\mathrm{syst}}$	$0.28 \pm 0.05_{\mathrm{stat}} \pm 0.04_{\mathrm{syst}}$	0.23 ± 0.05
^{7}Li	$0.6 \pm 0.1_{\mathrm{stat}} \pm 0.1_{\mathrm{syst}}$	$0.16 \pm 0.04_{\mathrm{stat}} \pm 0.04_{\mathrm{syst}}$	0.26 ± 0.08
^{9}Be	$1.0 \pm 0.1_{\mathrm{stat}} \pm 0.1_{\mathrm{syst}}$	$0.23 \pm 0.04_{\mathrm{stat}} \pm 0.03_{\mathrm{syst}}$	0.24 ± 0.05
^{13}C	$1.1 \pm 0.2_{\mathrm{stat}} \pm 0.2_{\mathrm{syst}}$	$0.29 \pm 0.07_{\mathrm{stat}} \pm 0.05_{\mathrm{syst}}$	0.26 ± 0.07
^{16}O	$1.6 \pm 0.3_{\mathrm{stat}} \pm 0.3_{\mathrm{syst}}$	$0.36 \pm 0.07_{\mathrm{stat}} \pm 0.06_{\mathrm{syst}}$	0.23 ± 0.06

Table 4.5: Yield of correlated Λp events within the event selection ($\cos\theta < -0.95$).

target	total yield (R_{total}) (%)	yield near threshold (R_{QF})(%)	$R_{\mathrm{QF}}/R_{\mathrm{total}}$
^{6}Li	$0.72 \pm 0.11_{\mathrm{stat}} \pm 0.10_{\mathrm{syst}}$	$0.18 \pm 0.04_{\mathrm{stat}} \pm 0.03_{\mathrm{syst}}$	0.25 ± 0.07
^{7}Li	$0.43 \pm 0.09_{\mathrm{stat}} \pm 0.10_{\mathrm{syst}}$	$0.13 \pm 0.04_{\mathrm{stat}} \pm 0.03_{\mathrm{syst}}$	0.30 ± 0.11
^{9}Be	$0.51 \pm 0.07_{\mathrm{stat}} \pm 0.07_{\mathrm{syst}}$	$0.15 \pm 0.03_{\mathrm{stat}} \pm 0.02_{\mathrm{syst}}$	0.29 ± 0.07
^{13}C	$0.55 \pm 0.10_{\mathrm{stat}} \pm 0.09_{\mathrm{syst}}$	$0.15 \pm 0.05_{\mathrm{stat}} \pm 0.02_{\mathrm{syst}}$	0.27 ± 0.10
^{16}O	$0.86 \pm 0.21_{\mathrm{stat}} \pm 0.14_{\mathrm{syst}}$	$0.17 \pm 0.05_{\mathrm{stat}} \pm 0.03_{\mathrm{syst}}$	0.19 ± 0.08

Table 4.3: Yield of correlated Λp events within the event selection ($\cos\theta < -0.80$).

target	total yield (R_{total}) (%)	yield near threshold (R_{QF})(%)	$R_{\mathrm{QF}}/R_{\mathrm{total}}$
^{6}Li	$1.8 \pm 0.2_{\mathrm{stat}} \pm 0.2_{\mathrm{syst}}$	$0.36 \pm 0.06_{\mathrm{stat}} \pm 0.05_{\mathrm{syst}}$	0.20 ± 0.04
^{7}Li	$0.9 \pm 0.1_{\mathrm{stat}} \pm 0.2_{\mathrm{syst}}$	$0.20 \pm 0.05_{\mathrm{stat}} \pm 0.05_{\mathrm{syst}}$	0.22 ± 0.06
^{9}Be	$1.4 \pm 0.1_{\mathrm{stat}} \pm 0.2_{\mathrm{syst}}$	$0.28 \pm 0.04_{\mathrm{stat}} \pm 0.04_{\mathrm{syst}}$	0.20 ± 0.04
^{13}C	$1.6 \pm 0.2_{\mathrm{stat}} \pm 0.3_{\mathrm{syst}}$	$0.43 \pm 0.09_{\mathrm{stat}} \pm 0.07_{\mathrm{syst}}$	0.25 ± 0.06
^{16}O	$2.4 \pm 0.3_{\mathrm{stat}} \pm 0.4_{\mathrm{syst}}$	$0.43 \pm 0.08_{\mathrm{stat}} \pm 0.07_{\mathrm{syst}}$	0.18 ± 0.04

4.4 $\Sigma^- p$ and Λn pairs

4.4.1 $\Sigma^- p$ pairs

Opening angle distribution

Figure 4.9 shows the opening angle distribution of $\Sigma^- p$ pairs for each target, together with the sideband contribution ($15\,\mathrm{MeV}/c^2 < |\mathrm{IM}(n\pi^-) - M(\Sigma^-)| < 25\,\mathrm{MeV}/c^2$). A clear back-to-back correlation is observed, while the sideband spectra show a very weak back-to-back correlation.

The back-to-back region of $\cos\theta(\Sigma^- p) < -0.90$ was selected as the correlated $\Sigma^- p$ pairs in the following analysis.

Energy sum distribution

The energy sum distribution for the correlated $\Sigma^- p$ pairs is shown in Fig. 4.10 for each target. A prominent enhancement is seen around the kinematical threshold, while the sideband contribution is distributed in a wide region. The enhancement suggests the contribution from QF-TNA. The resolution for the energy sum is dependent slightly on the momentum of a Σ^- and a proton. For example, the resolution of a back-to-back pair of a Σ^- and a proton ($500\,\mathrm{MeV}/c$), whose energy sum is 2.361 GeV, is

$$\sigma(E_{\mathrm{sum}}) = \sqrt{\sigma(E_{\Sigma^-})^2 + \sigma(E_p)^2} \sim 5\,\mathrm{MeV}. \tag{4.8}$$

The observed peak is rather broader than the detector resolution. This is probably because the residue can be not only in the ground state but also in excited states.

Momentum correlation between Σ^- and proton

The momentum distribution of Σ^- and proton, whose energy sum is in the near-threshold region (between 2.30 GeV and 2.38 GeV), are shown in Fig. 4.11. A two-dimensional plot

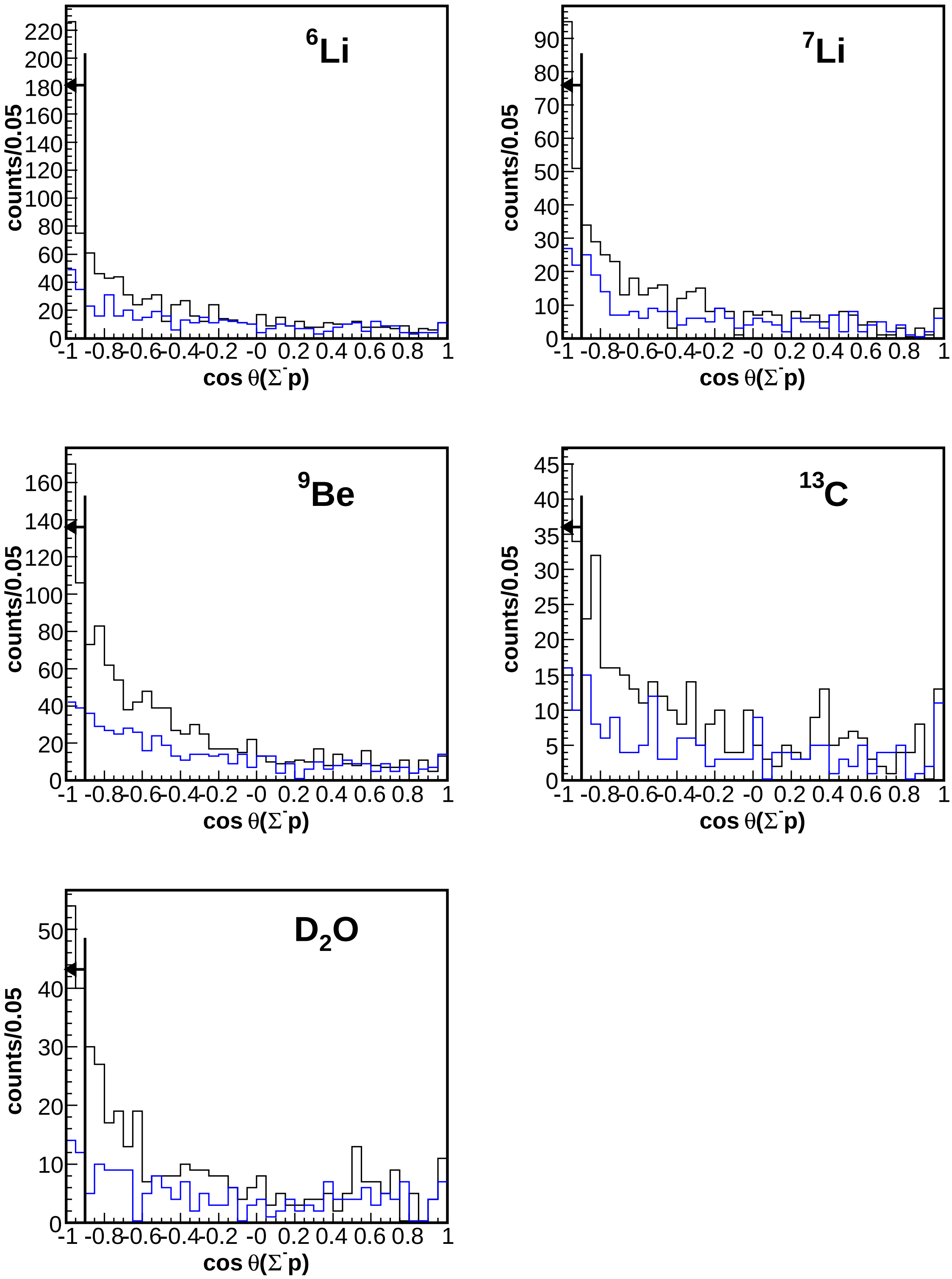

Figure 4.9: Opening angle between a Σ^- and a proton. The black histogram denotes the sideband contribution for the Σ^- peak in the $n\pi^-$ invariant mass spectrum.

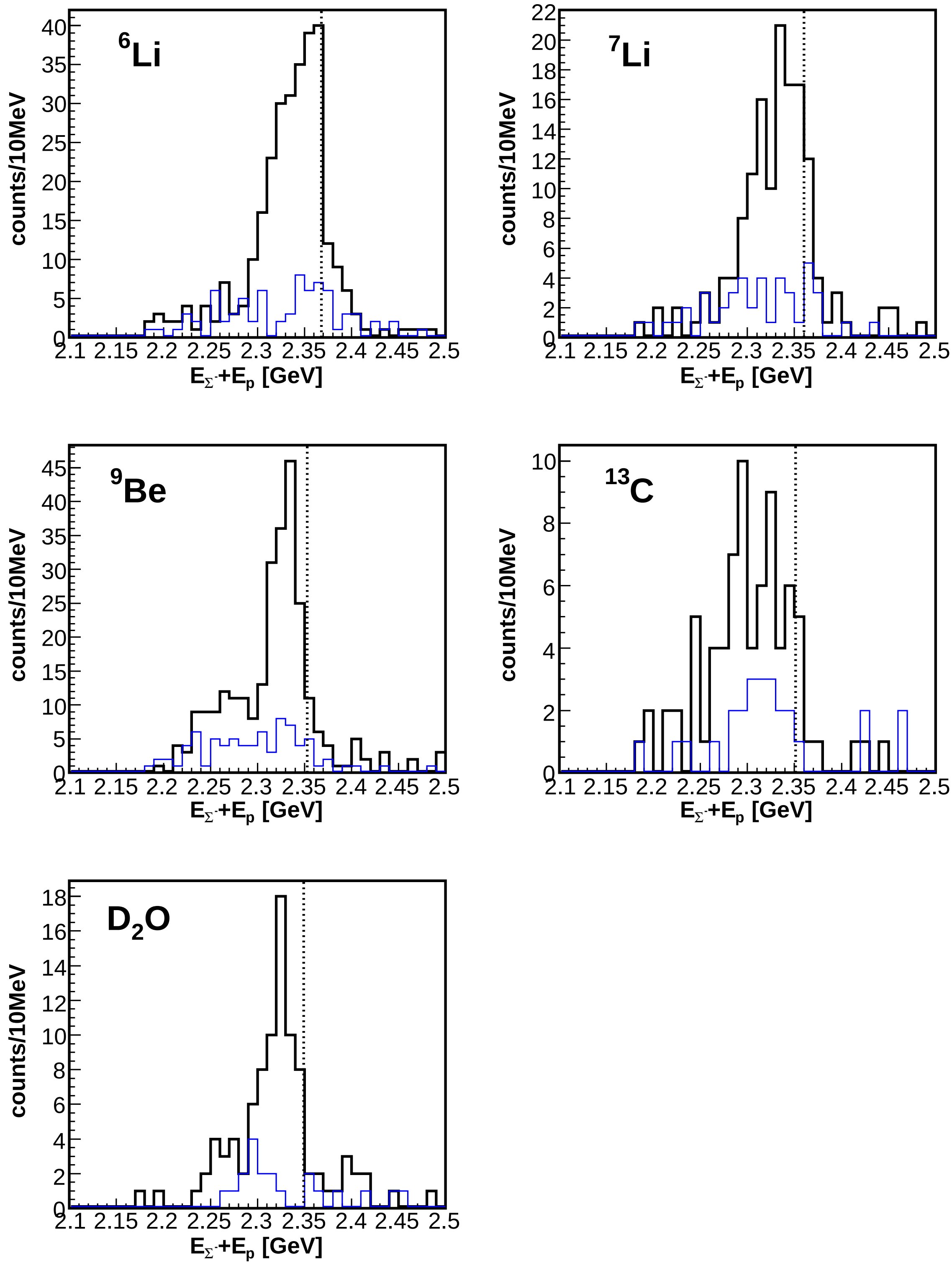

Figure 4.10: Energy sum of back-to-back Σ^- and proton. The blue histogram is the sideband contribution. The kinematical threshold is indicated by a vertical line.

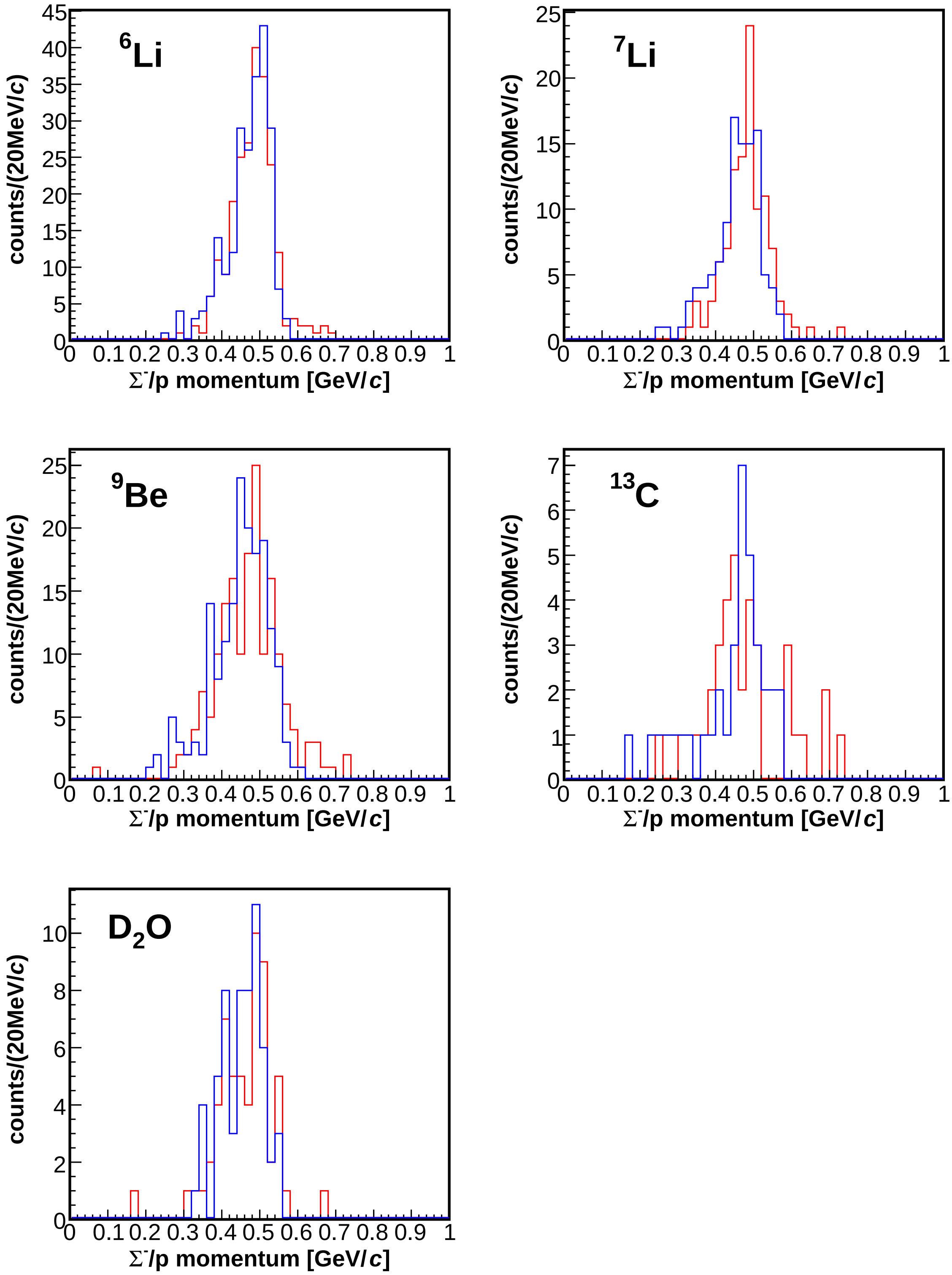

Figure 4.11: Momentum distribution of back-to-back Σ^- (red) and proton (blue) for $2.30\,\mathrm{GeV} < E_{\mathrm{sum}} < 2.38\,\mathrm{GeV}$.

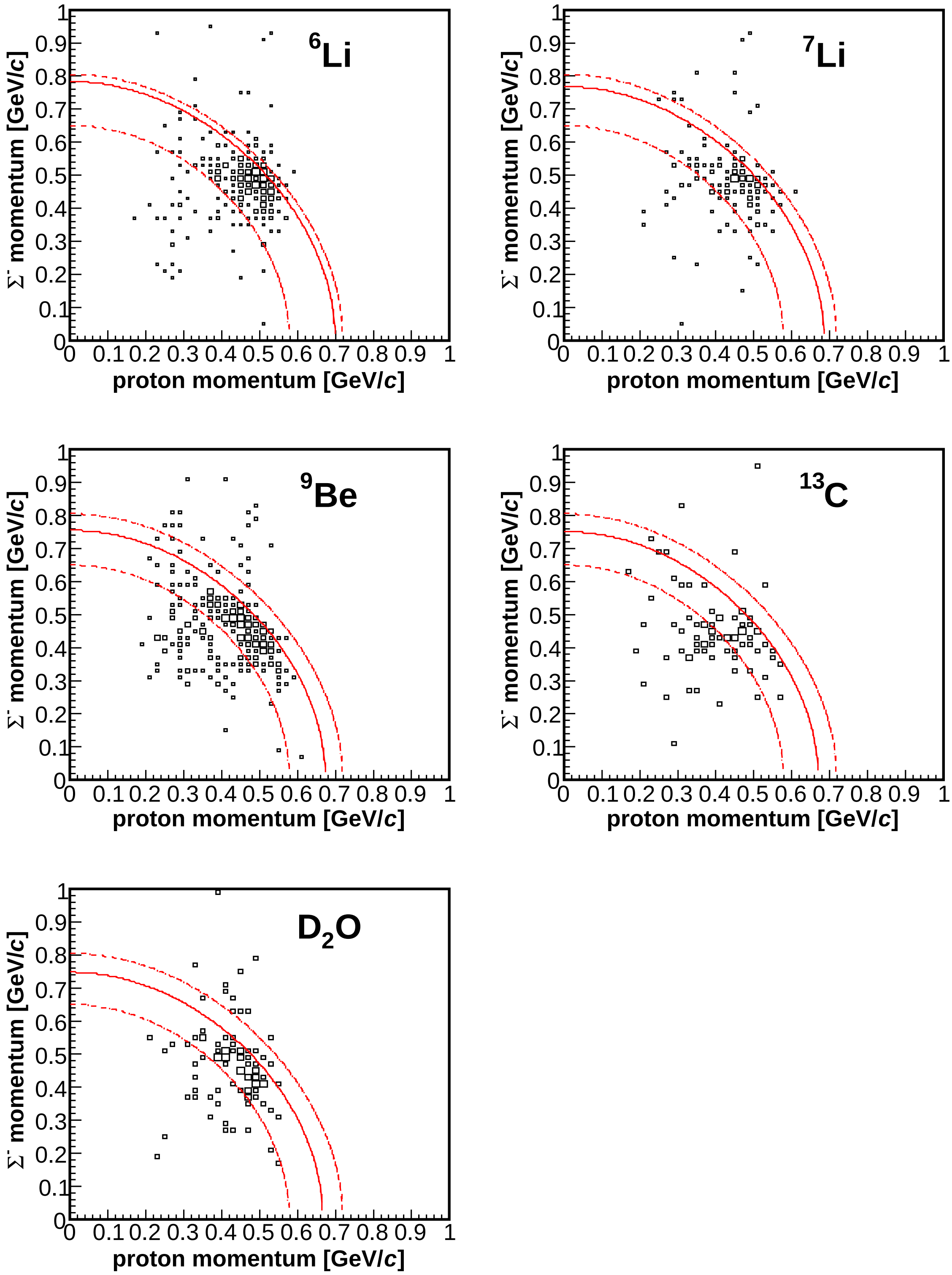

Figure 4.12: Momentum correlation for back-to-back Σ^- and proton pairs. The solid line is the threshold, and the dashed lines corresponds to the energy sum of 2.30 and 2.38 GeV.

is also shown in Fig. 4.12. The distributions for both Σ^- and proton are centered at $\sim$ 500 MeV/c, and the shapes are similar to each other.

4.4.2 Λn pairs

Opening angle distribution

The opening angle distribution for Λn pairs for each target is shown in Fig. 4.13. While the contribution of background neutrons is seen as an almost flat component, a narrow back-to-back component is prominent. A tight cut of $\cos\theta(\Lambda n) < -0.95$ was applied to select the correlated Λn pairs. A small enhancement near $\cos\theta = 1$ may be attributed to a fake neutron hit associated with the decay particles of the Λ itself.

A level of contamination of background neutrons was estimated in the region between -0.50 and $+0.50$ in $\cos\theta(\Lambda n)$.

Energy sum distribution

The energy sum distribution for the correlated Λn pairs is shown in Fig. 4.14 for each target. The energy resolution is much poorer for the Λn pairs compared with the $\Sigma^- p$ pairs. For example, the resolution for a pair with both momenta at 580 MeV/c, corresponding to the energy sum of 2.362 GeV, was estimated as:

$$\sigma(E_{\text{sum}}) = \sqrt{\sigma(E_\Lambda)^2 + \sigma(E_n)^2} \sim 27\,\text{MeV}. \tag{4.9}$$

If the resolution is taken into account, it can be concluded that an enhancement around the kinematical threshold is seen in Fig. 4.14.

Momentum correlation between Λ and neutron

Figure 4.15 is the momentum distributions of Λ and neutron in the near-threshold region, in the same way as for the $\Sigma^- p$ pairs. A two-dimensional plot of momenta of Λ and neutron is shown in Fig. 4.16.

4.4.3 Λn and $\Sigma^- p$ pairs from QF-TNA

Assuming both Λn and $\Sigma^- p$ pairs are the products of the kaon absorption with a pn-pair, their energy sum distribution should be almost the same. The observed spectra are consistent with this expectation.

The yield (R) of back-to-back Λn and $\Sigma^- p$ in the near-threshold region (QF-TNA) was

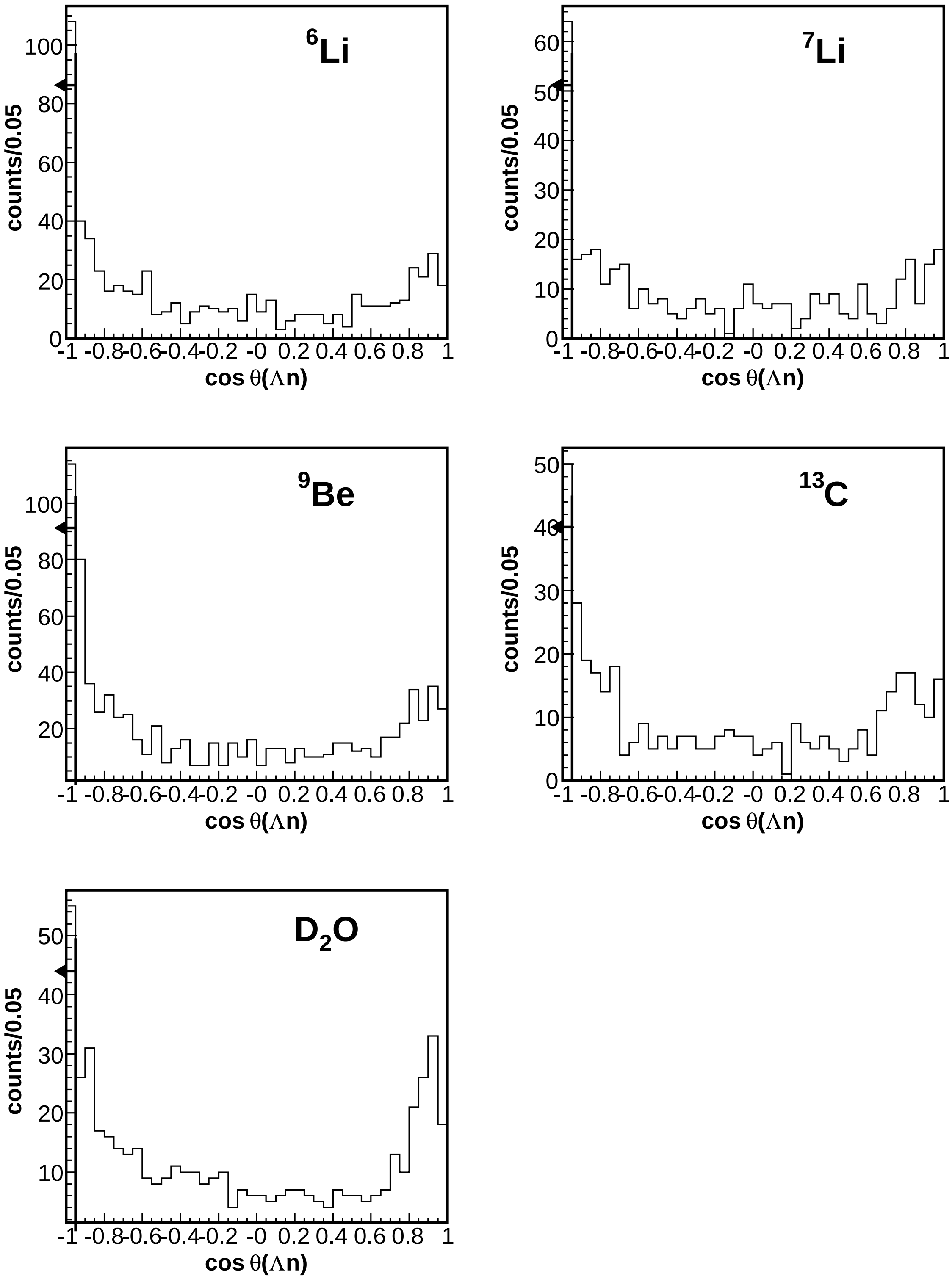

Figure 4.13: Opening angle between a Λ and a neutron.

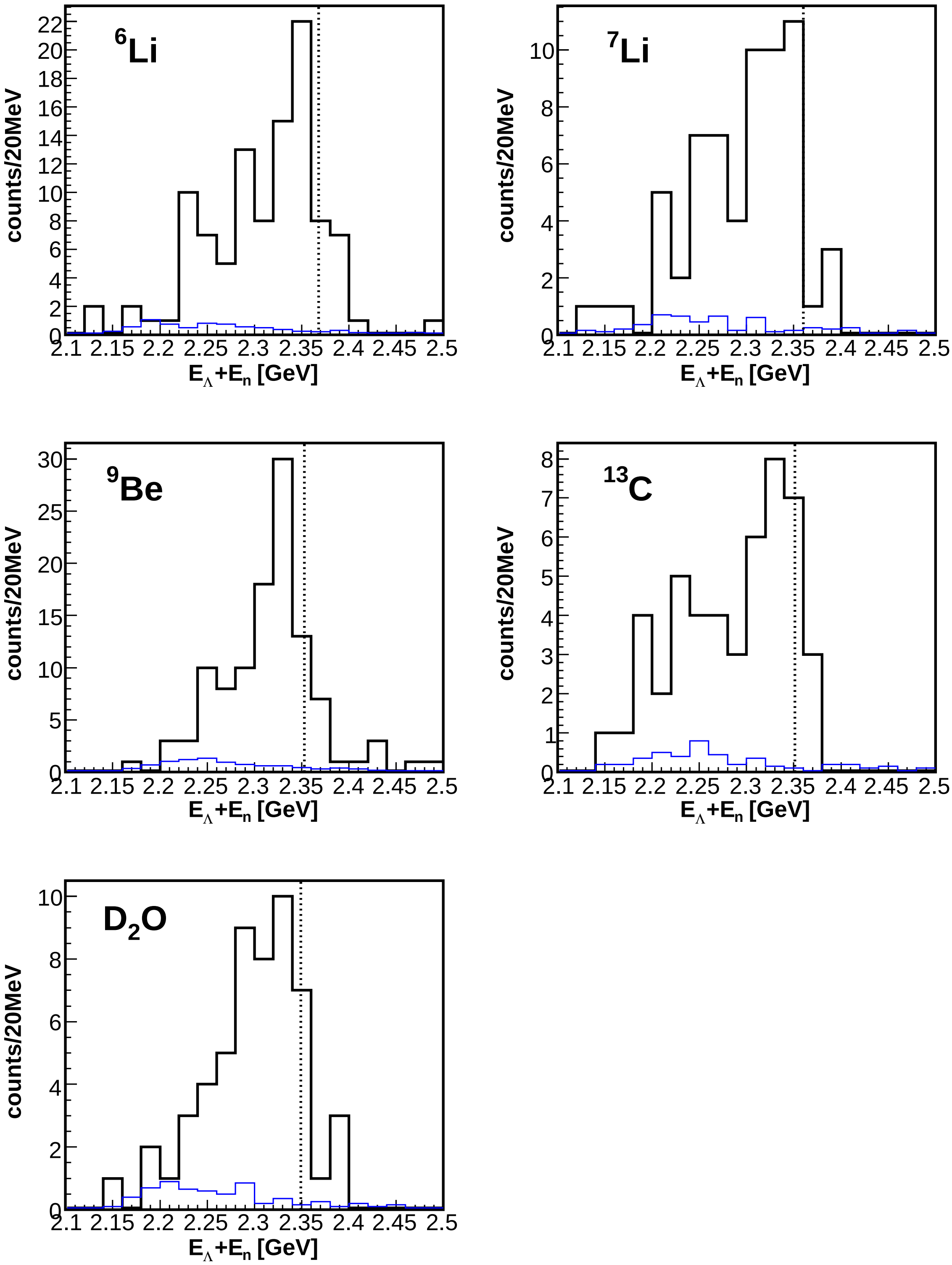

Figure 4.14: Energy sum of back-to-back Λ and neutron. The blue histogram is the scaled contribution of non-back-to-back events. The kinematical threshold is indicated by a vertical line.

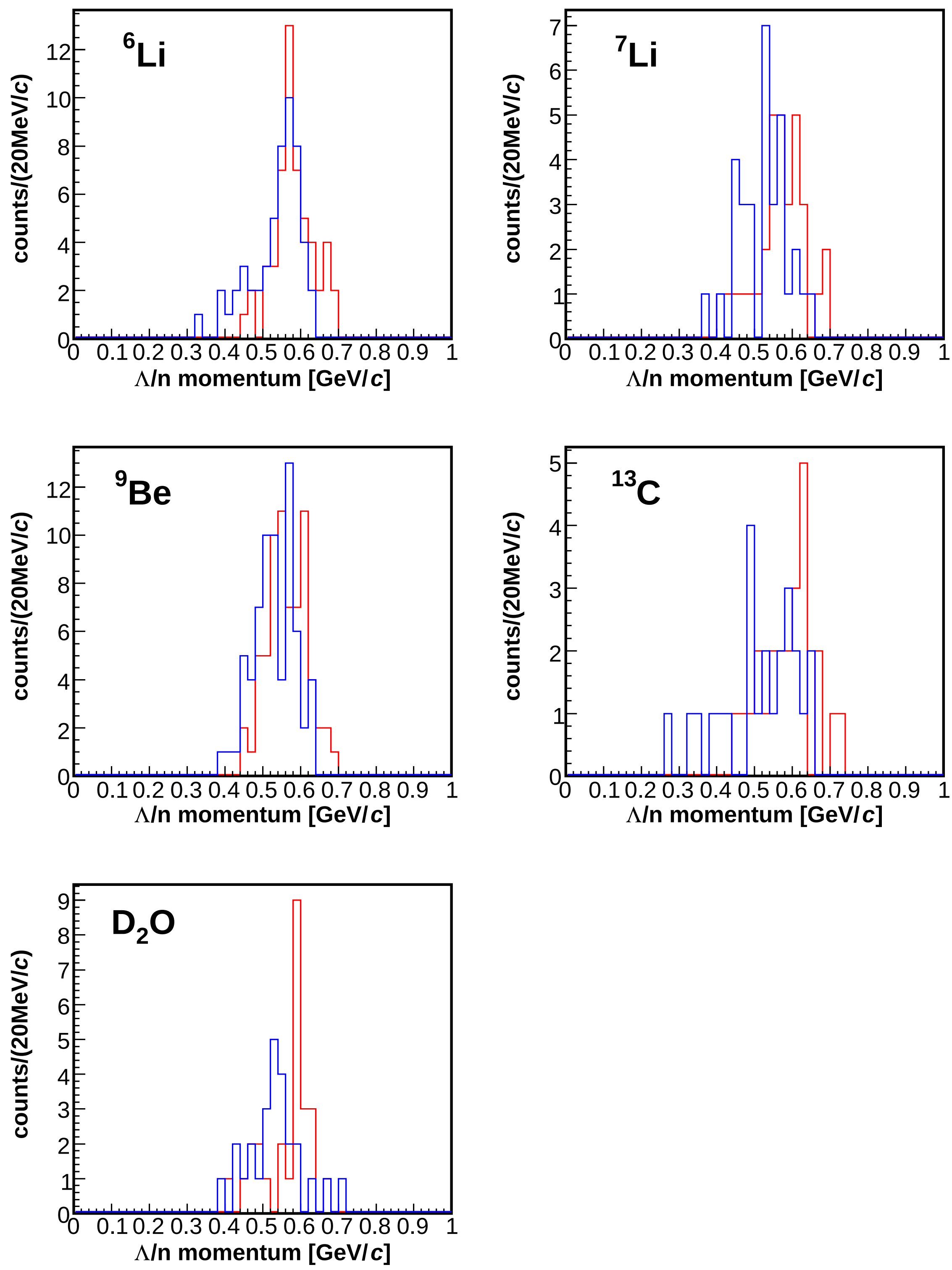

Figure 4.15: Momentum distribution of back-to-back Λ (red) and neutron (blue) for $2.30\,\mathrm{GeV} < E_{\mathrm{sum}} < 2.38\,\mathrm{GeV}$.

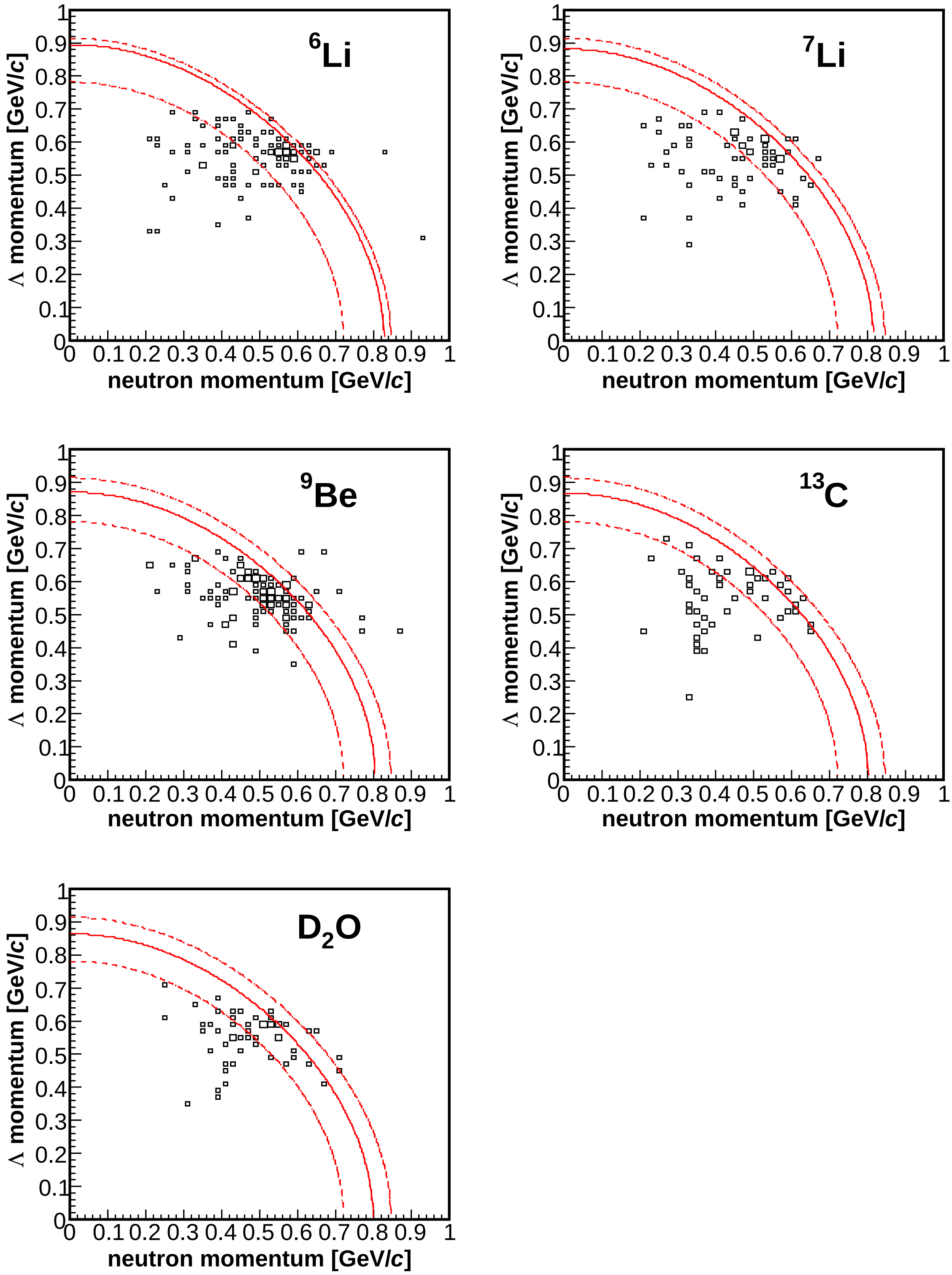

Figure 4.16: Momentum correlation for back-to-back Λ and neutron pairs. The solid line is the threshold, and the dashed lines corresponds to the energy sum of 2.30 and 2.38 GeV.

estimated from the following relationship:

$$R(\Lambda n) = \frac{N(\Lambda n)}{\overline{\epsilon(\Lambda n)}\epsilon_p^{(\mathrm{long})}\epsilon_{\pi^-}^{(\mathrm{short})}N(K^-_{\mathrm{stop}})}, \tag{4.10}$$

$$R(\Sigma^- p) = \frac{N(\Sigma^- p)}{\overline{\epsilon(\Sigma^- p)}[\epsilon_{p,\pi^-}^{(\mathrm{long})}]^2 N(K^-_{\mathrm{stop}})}, \tag{4.11}$$

where $\overline{\epsilon(YN)}$ is the averaged acceptance of hyperon and nucleon. Here, in order to deduce $\bar{\epsilon}$, the momentum distribution of hyperon and nucleon was derived from a model simulation by assuming a recoil momentum distribution as described in Sec. 4.4.4. This is because the statistics of the observed pairs was not enough large to determine the actual distribution precisely, and the momentum resolution of a fast neutron was poor.

4.4.4 Toy model simulation with two-nucleon absorption model

We assume a kaon at zero momentum is absorbed by a quasi-deuteron inside a ^{12}C nucleus. The quasi-deuteron mass is artificially decreased from the deuteron mass, to satisfy the energy conservation law for the reaction $K^- + {}^{12}\mathrm{C} \to Y + N + {}^{10}\mathrm{B}$, where the residual nucleus is assumed to be in its ground state. Three kinds of quasi-deuteron momentum distribution in ^{12}C are used as inputs: Hulthén wavefunction, cluster model calculation, and Fermi gas model.

Hulthén wavefunction

The Hulthén wavefunction for quasi-deuteron is expressed in the momentum space as a simple Gaussian,

$$\rho(p) \propto \exp(-p^2/\gamma^2), \tag{4.12}$$

where p is the momentum of quasi-deuteron, γ is a parameter. Here, $\gamma = 160\,\mathrm{MeV}/c$ was taken from [77].

Cluster model calculation

Yamazaki and Akaishi calculated the quasi-deuteron momentum distribution in a d-core cluster model with the orthogonality condition for ^{4}He, ^{6}Li and ^{12}C [89]. The momentum distribution has two components. The component below (above) $\sim 200\,\mathrm{MeV}/c$ corresponds to the deuteron in the p-shell (s-shell). While the reaction rate for each component is assumed to be equal in this toy model simulation, the back-to-back pair of hyperon and nucleon are mainly attributed to slow quasi-deuterons in the lower component.

Fermi gas model

In a simple Fermi gas model, a nucleon is uniformly distributed in a Fermi sphere in its momentum space. Picking up two nucleons randomly in the Fermi sphere with the radius $p_F = 221\,\mathrm{MeV}/c$ for ^{12}C, the momentum of a quasi-deuteron is assumed to be described as the sum of the momenta of the two nucleons.

Figure 4.17 shows the quasi-deuteron momentum distribution for each model.

For two kinds of reactions:

$$K^- + "d" \rightarrow \Lambda + n, \tag{4.13}$$

$$K^- + "d" \rightarrow \Sigma^- + p, \tag{4.14}$$

the opening angle distributions are shown in Fig. 4.18. As expected, they have a back-to-back correlation. However, the tail distribution depends on the assumed quasi-deuteron momentum distribution. The quasi-deuteron momentum distribution after the same angular cut as that for the real data, is overlaid in Fig. 4.17. A slower quasi-deuteron momentum component is likely to result in strongly back-to-back pairs.

For comparison, the observed recoil momentum distributions for $\Sigma^- p$ and Λn pairs are shown in Figs. 4.19 and 4.20[2]. In this model, the recoil momentum corresponds to the quasi-deuteron momentum. Each of the quasi-deuteron momentum distributions introduced above resembles the data, and it is hard to distinguish the models with the present statistics and resolution.

The calculated momentum distributions for Λn and $\Sigma^- p$ pairs with the angular cut are shown in Figs. 4.22 and 4.23, respectively. The momentum distribution for each of Λn ($\Sigma^- p$) is centered at $\sim 560\,\mathrm{MeV/c}$ ($\sim 480\,\mathrm{MeV/c}$), independent of the quasi-deuteron momentum distribution. The momentum distributions of hyperon and nucleon are broadly distributed.

For other channels, such as:

$$K^- + \text{“}pp\text{”} \rightarrow \Lambda + p, \tag{4.15}$$

$$K^- + \text{“}pp\text{”} \rightarrow \Sigma^0 + p, \tag{4.16}$$

$$K^- + \text{“}pp\text{”} \rightarrow \Sigma^+ + n, \tag{4.17}$$

$$K^- + \text{“}pn\text{”} \rightarrow \Sigma^0 + n, \tag{4.18}$$

$$K^- + \text{“}nn\text{”} \rightarrow \Sigma^- + n, \tag{4.19}$$

similar momentum distributions are anticipated as far as the same assumption (e.g. the correlated two-nucleon momentum distribution) is applied.

4.4.5 Yield of QF-TNA Λn and $\Sigma^- p$ pairs

From three kinds of momentum distributions of hyperon and nucleon, $\overline{\epsilon(\Lambda n)}$ and $\overline{\epsilon(\Sigma^- p)}$ were estimated to be $(0.915 \pm 0.065) \times 10^{-4}$ and $(0.866 \pm 0.052) \times 10^{-3}$, respectively. Then,

[2]The recoil momentum distribution for back-to-back Λp pairs (Fig. 4.21) is broader than those of Λn and $\Sigma^- p$ pairs. It is related to the different angular cuts among them. When a stronger cut is applied for Λp pairs, events with larger recoil momentum are reduced.

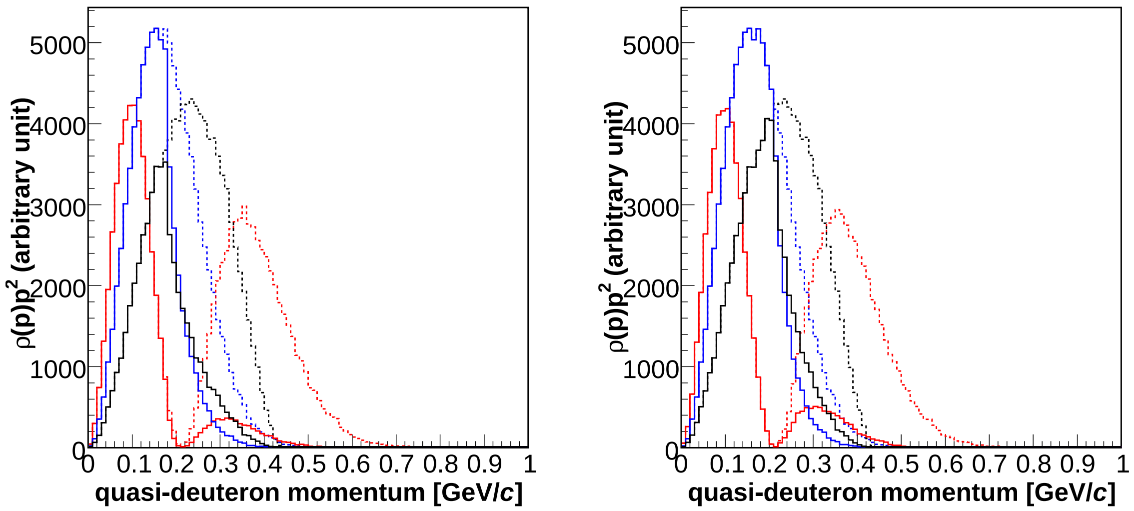

Figure 4.17: Simulated quasi-deuteron momentum distribution with Hulthén distribution (blue), cluster model calculation (red), and Fermi gas model (black), indicated by the dashed lines (the same for the two figures). The bold lines show the result of the cut for a back-to-back hyperon and nucleon (Λn in the left figure and $\Sigma^- p$ in the right figure).

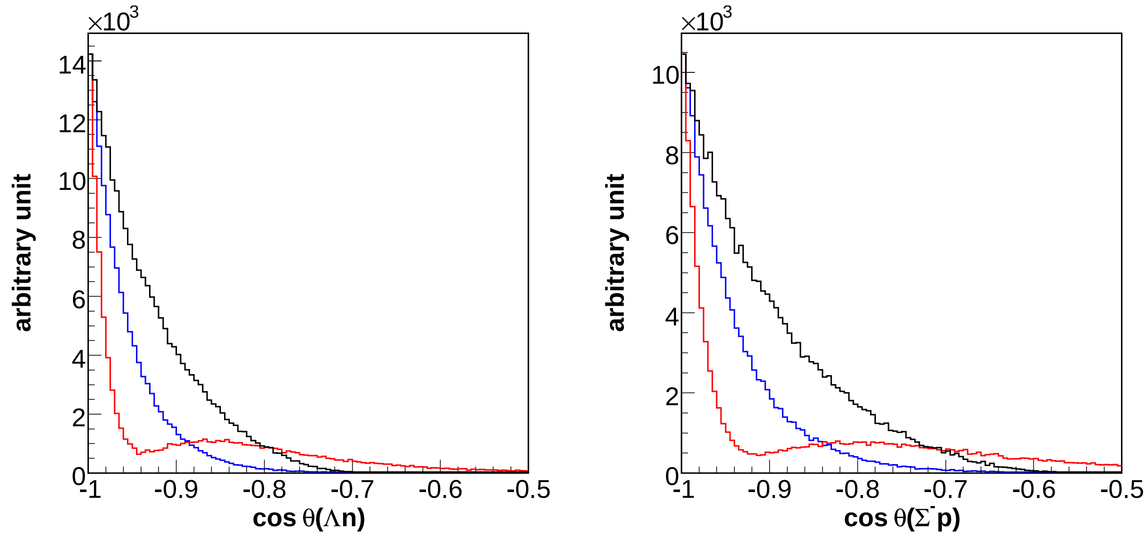

Figure 4.18: Simulated opening angle distribution of Λn (left) and $\Sigma^- p$ (right). The maximum of the histogram for each quasi-deuteron distribution is normalized to be equal. The meaning of the colors is the same as Fig. 4.17.

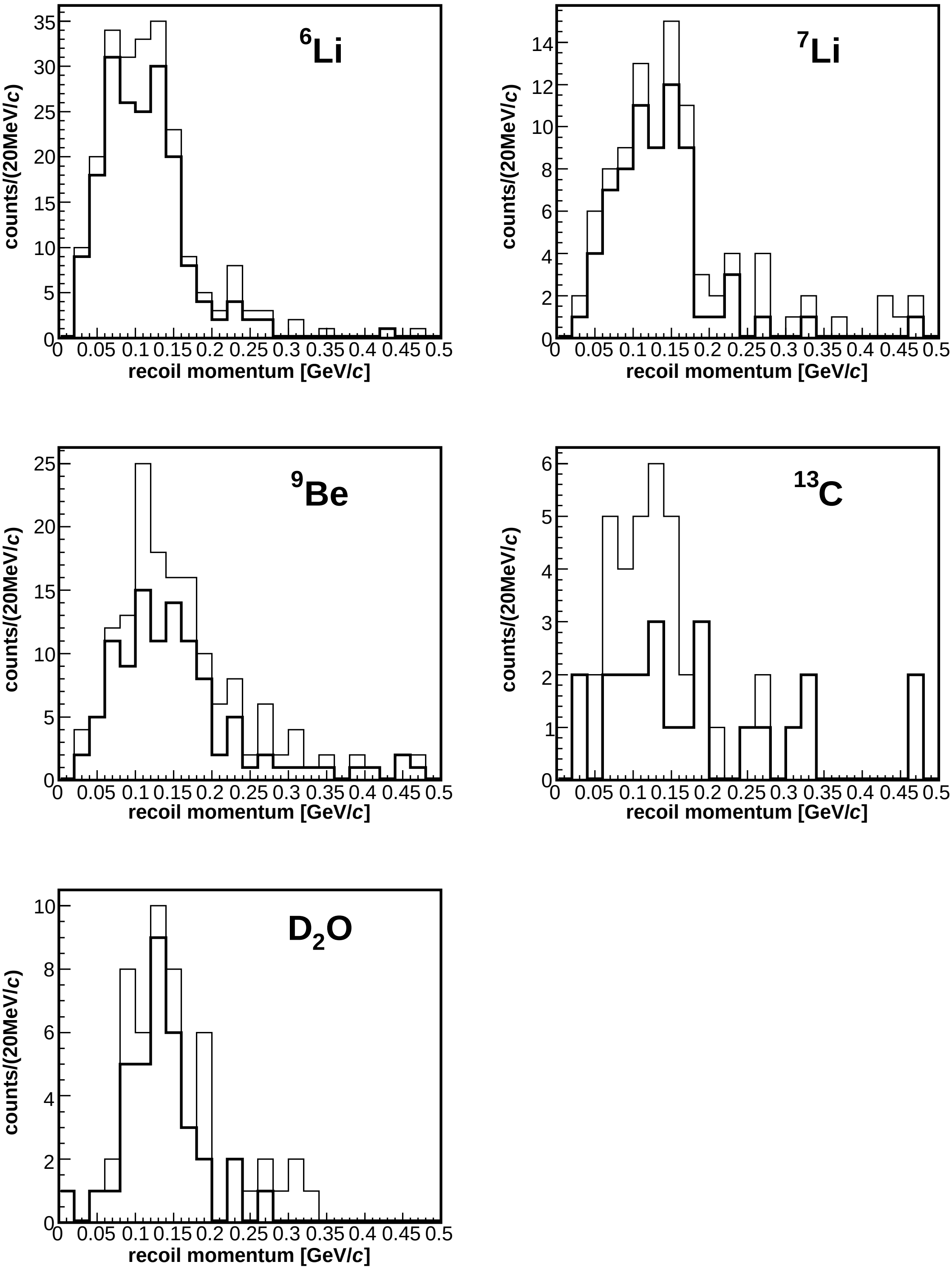

Figure 4.19: Recoil momentum distribution for back-to-back $\Sigma^- p$ pairs. The bold line corresponds to the near-threshold region.

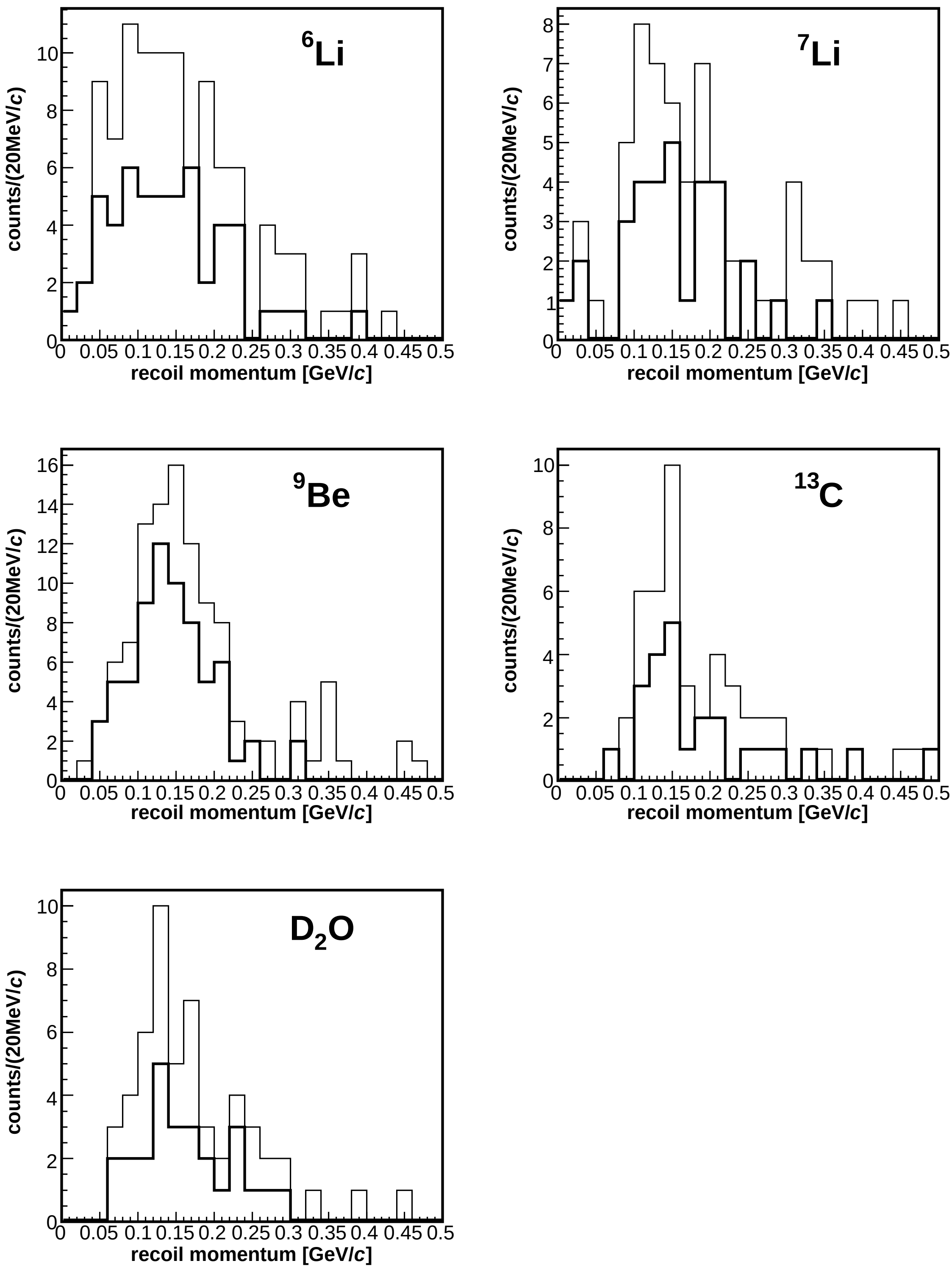

Figure 4.20: Recoil momentum distribution for back-to-back Λn pairs. The bold line corresponds to the near-threshold region.

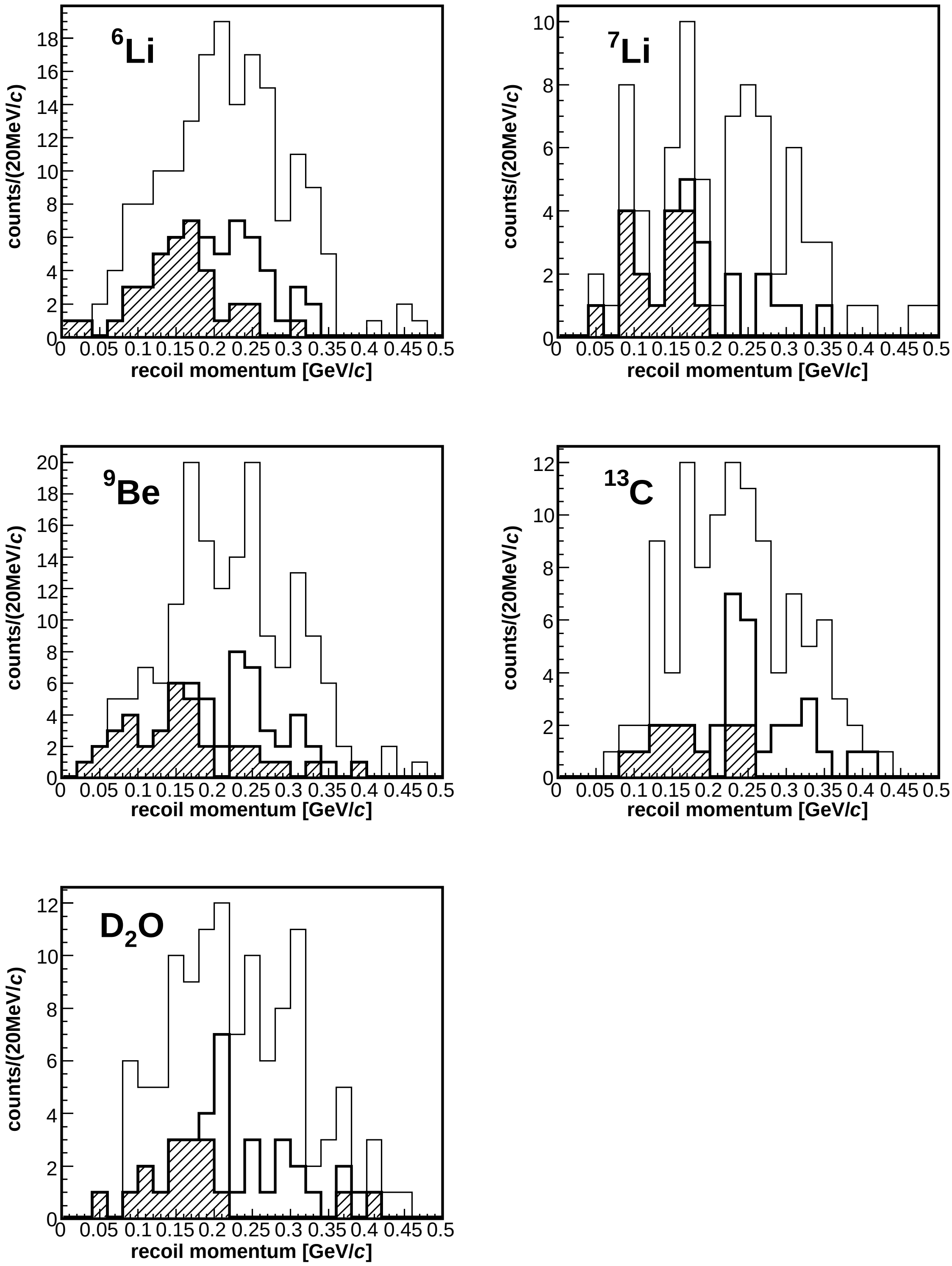

Figure 4.21: Recoil momentum distribution for back-to-back Λp pairs. The bold line corresponds to the near-threshold region (between 2.30 GeV and 2.38 GeV). The result with a tight angular cut $\cos\theta(\Lambda p) < -0.95$ is also shown in the hatched histogram.

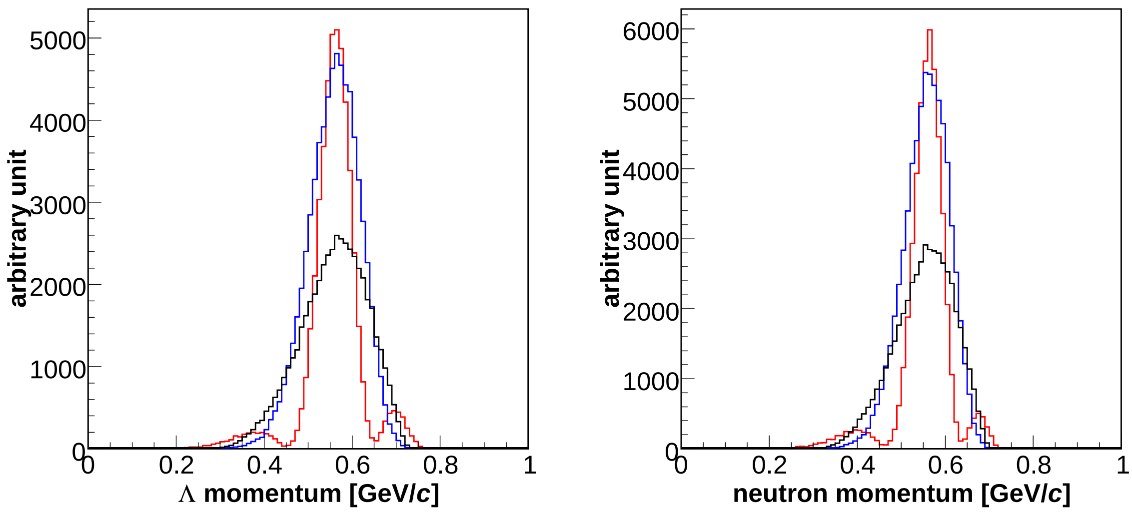

Figure 4.22: Simulated momentum distributions of Λ (left) and neutron (right) after quasi-free two-nucleon absorption. The meaning of the colors is the same as Fig. 4.17.

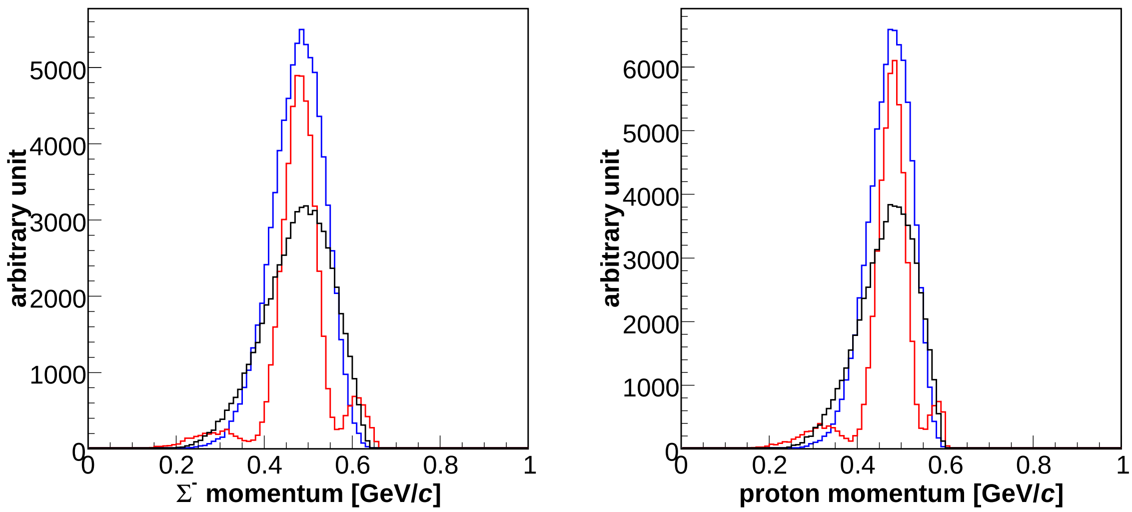

Figure 4.23: Simulated momentum distributions of Σ^- (left) and proton (right) after quasi-free two-nucleon absorption. The meaning of the colors is the same as Fig. 4.17.

Table 4.6: Yield of back-to-back Λn and $\Sigma^- p$ events near the kinematical threshold.

target	Λn yield (%)	$\Sigma^- p$ yield (%)
^{6}Li	$2.3 \pm 0.3_{\mathrm{stat}} \pm 0.3_{\mathrm{syst}}$	$1.07 \pm 0.09_{\mathrm{stat}} \pm 0.18_{\mathrm{syst}}$
^{7}Li	$1.9 \pm 0.3_{\mathrm{stat}} \pm 0.4_{\mathrm{syst}}$	$0.64 \pm 0.09_{\mathrm{stat}} \pm 0.16_{\mathrm{syst}}$
^{9}Be	$2.6 \pm 0.3_{\mathrm{stat}} \pm 0.4_{\mathrm{syst}}$	$0.68 \pm 0.07_{\mathrm{stat}} \pm 0.11_{\mathrm{syst}}$
^{13}C	$1.9 \pm 0.4_{\mathrm{stat}} \pm 0.3_{\mathrm{syst}}$	$0.22 \pm 0.07_{\mathrm{stat}} \pm 0.04_{\mathrm{syst}}$
^{16}O	$2.4 \pm 0.5_{\mathrm{stat}} \pm 0.4_{\mathrm{syst}}$	$0.60 \pm 0.10_{\mathrm{stat}} \pm 0.11_{\mathrm{syst}}$

the obtained yields are summarized in Table 4.6. Note that the total yield for each pair from two-nucleon absorption could be larger than the values in Table 4.6 for QF-TNA defined in this analysis, because some tail parts, cut away from the selection, are strongly dependent on the model of the quasi-deuteron momentum distribution and the reaction mechanism of the two-nucleon absorption process.

4.5 Summary of the observed hyperon-nucleon pairs

Figure 4.24 is the summary of the obtained yields of QF-TNA hyperon-nucleon pairs, the integrated yield of Λp pairs, together with the fast Λ's above 400 MeV/c (Table 4.1).

The yield of fast Λ's (black line) is about 1/4 of that of multi-nucleon absorption (Table 1.2). A large part of them were found to be associated with a proton or a neutron in back-to-back (magenta line for Λp and green line for Λn). Most of the Λp pairs have the energy sum below the near-threshold region, and only $\sim 1/5$ of the Λp pairs (red line) are in the near-threshold region.

On the other hand, the yield of QF-TNA Λn pairs is as large as the yield of Λp pairs. Comparing with the QF-TNA yield for the Λn pairs, it indicates that the Λn pairs from QF-TNA dominates over the Λp pairs from QF-TNA by the factor of $\gtrsim 5$.

Recently, the KEK-PS E549 experiment studied the ΛN correlation from stopped K^- absorption on ^{4}He, and reported the yield of "quasi-free"[3] Λp and Λn pairs as $\sim 0.2\%$ and $\sim 2\%$, respectively [90]. Similar results in the two experiments infer a small A-dependence of the yield.

[3] Their definition of "quasi-free" is different from this thesis. They define the missing mass of $^4\mathrm{He}(K^-_{\mathrm{stop}}, \Lambda N)$ to be less than $2m_n + 40\,\mathrm{MeV}/c^2$ for Λp pairs and $m_d + 25\,\mathrm{MeV}/c^2$ for Λn pairs, where m_n and m_d are the neutron mass and the deuteron mass, respectively. However, the energy sum for an event satisfying this criterion almost distributes above 2.30 GeV, which is the definition of "quasi-free" in this thesis.

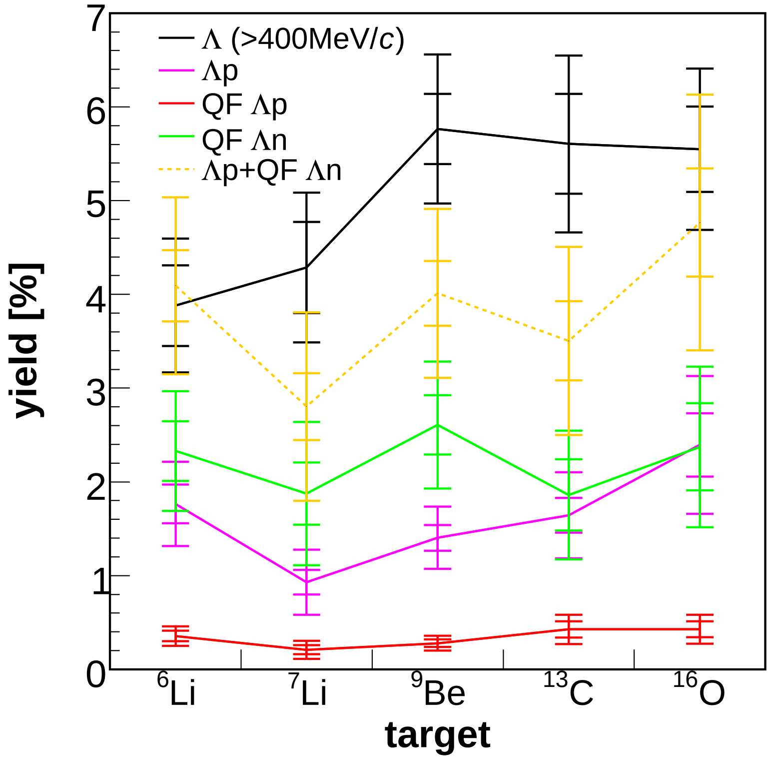

Figure 4.24: Yield of fast Λ's, correlated Λp, and correlated QF-TNA ΛN pairs. Both the statistical and systematic errors are indicated.

4.5.1 Yield of Λn pairs below near-threshold region

The estimation of the yield of Λn pairs below the near-threshold region was difficult because of the poor statistics and the contamination of background neutrons. Nevertheless, its contribution could be estimated by the comparison of the yield of fast Λ's (black line) and the sum of the yield of Λp pairs and QF-TNA Λn pairs (orange line). Because the Λ in a ΛN pair, whose yield was already obtained, has a momentum above $400\,\mathrm{MeV}/c$, the difference of $\lesssim 2\%$ gives an upper limit of a pair of fast Λ and neutron below the near-threshold region. It is comparable at most to the yield of quasi-free Λn pairs, or even smaller. In other words, the ratio of QF-TNA Λn pairs to the total ΛN pairs ($R_{\mathrm{QF}}/R_{\mathrm{total}}$) is at least 1/2, compared with that for Λp pairs as shown in Table 4.3.

Chapter 5

Discussion

While the QF-TNA components are apparently seen for the correlated Λn and $\Sigma^- p$, the dominant component in the correlated Λp pairs is far below the threshold, not in the near-threshold region. In this chapter, interpretations of the different distributions for pn-absorption (into $\Sigma^- p$ and Λn) and pp-absorption (into Λp) are discussed.

5.1 Two-nucleon absorption in kaon absorption

As already discussed in Chapter 4, the energy sum of the correlated Λn and $\Sigma^- p$ pairs distribute in the near-threshold regions, and they can be attributed to the QF-TNA, like pion absorption by a pn pair. On the other hand, a QF-TNA component of the correlated Λp pairs was not observed in the energy sum distribution for any of the targets from ^{6}Li to ^{16}O, contrary to pion absorption.

Figure 5.1 is a kinetic energy spectrum for correlated hyperon-nucleon pairs for ^{6}Li, ^{9}Be, and ^{16}O targets. The corresponding momentum spectra are also shown in Fig. 5.2. The near-threshold enhancement of the $\Sigma^- p$ pairs is seen for the three targets, and can be understood as quasi-free pn-absorption. Moreover, the Λn distribution looks to have a similar enhancement, which is reinforced by the assumption that both $\Sigma^- p$ and Λn pairs have the same origin of (quasi-free) pn-absorption. On the contrary, the Λp distribution is broadly distributed, even for a heavier target, reminded that pion quasi-free pp-absorption was observed for ^{12}C target (Fig. 1.7).

The following three features need to be explained.

(A) channel dependence among the three modes (especially between Λn and Λp pairs)

The Λn and $\Sigma^- p$ pairs from pn-absorption have an enhancement in the near-threshold region. For the Λn pairs, the contribution below this region was found to be small compared with that in the region, as discussed in Sec. 4.5.1. On the contrary, the energy sum of the Λp pairs are broadly distributed, and the yield in the near-threshold region is only about 1/5 of the total yield.

(B) little QF-TNA contribution in the observed Λp pairs
As described just above, only $\sim$ 1/5 of the Λp pairs in the event selection ($p_\Lambda >$ 400 MeV/c and $p_p >$ 300 MeV) are populated in the near-threshold region, where a Λp pair from QF-TNA is expected to distribute. It can never be explained by a simple assumption of QF-TNA without any further secondary process.

(C) small A-dependence in the correlation of the Λp pairs
The energy sum distribution of the Λp pair for different targets resembles each other, as shown in Sec. 4.3. The momentum distribution of the two particles is broadly distributed for every target.

In the following sections, we will examine several possible interpretations with respect to these three features.

5.2 Assumption of K^-pp bound states

As described in Sec. 1.3, we gave an interpretation that the observed Λp pair was the decay product of K^-pp bound state, in the analysis of the first data taking. In this section, this interpretation is reconsidered with the new information obtained for one order of magnitude more statistics in the second data taking.

This interpretation brings strong channel dependence [(A) and (B)] because of strong isospin dependence of $\overline{K}N$ interaction: while the K^-pp system may be deeply bound below the $K^- + p + p$ threshold, the K^-d system is not expected to be bound, around $\Lambda(1405) + n$ at most [46]. This is because the fraction of a strongly attractive $\overline{K}N$ pair with isospin 0 is much smaller in the K^-d system than that in the K^-pp system[1]. Therefore, the K^- + "pp" system is notable as an entrance channel to form a bound state.

After the FINUDA Collaboration reported the invariant mass distribution of back-to-back Λp pairs in 2005 [66], few-body calculations with various methods have been carried out for the K^-pp system. Here, some of them are briefly described.

[1]If the NN isospin is a good quantum number, a $\overline{K}NN$ system with the NN isospin 0 (K^-d, for instance) has 1/2 isospin-0 $\overline{K}N$ pair and 3/2 isospin-1 $\overline{K}N$ pairs. To the contrary, a $\overline{K}NN$ system with the NN isospin 1 and the total isospin 1/2 (K^-pp, for instance) has 3/2 isospin-0 $\overline{K}N$ pairs and 1/2 isospin-1 $\overline{K}N$ pair.

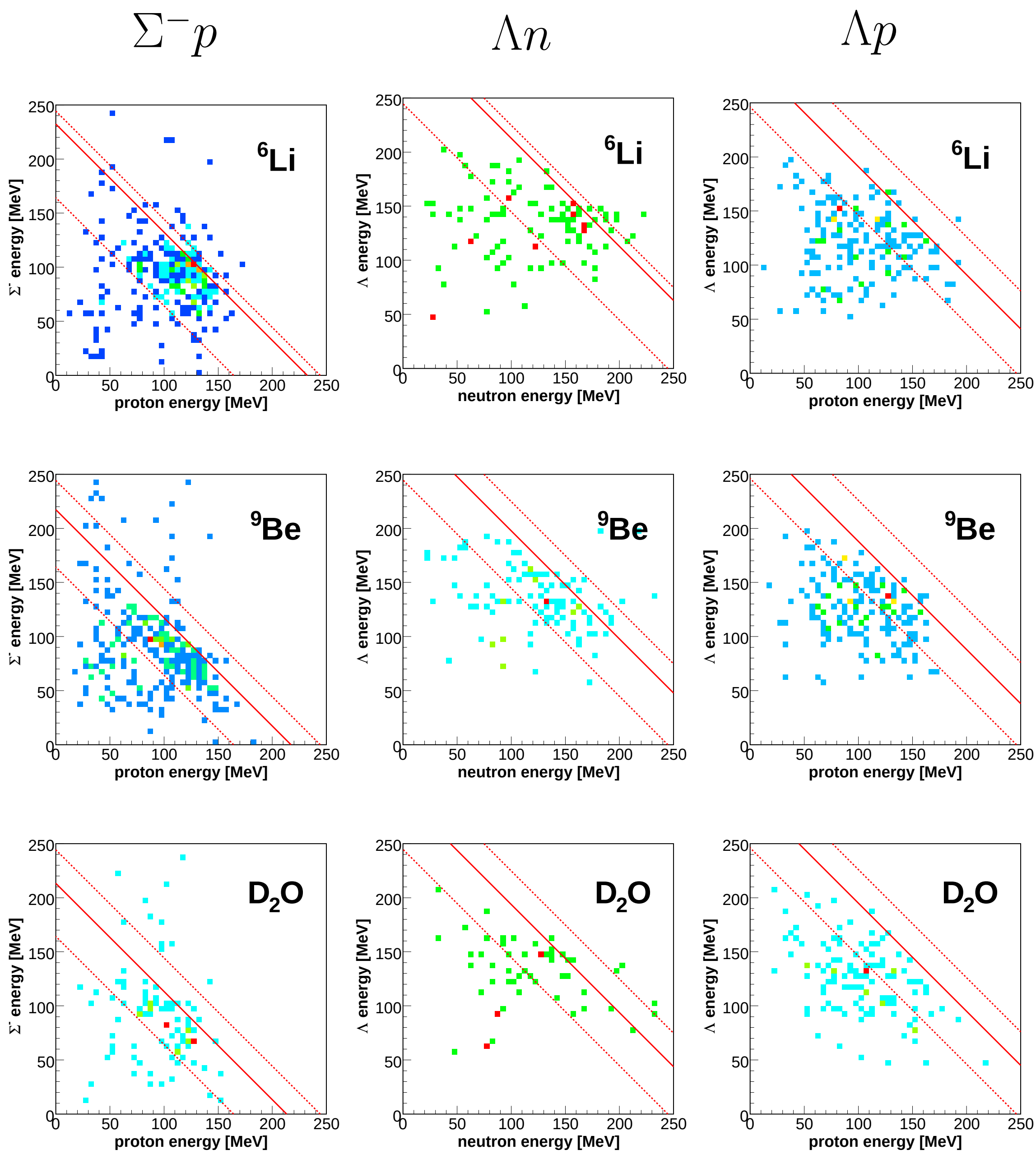

Figure 5.1: Two-dimensional energy spectra of correlated $\Sigma^- p$ (left), Λn (middle), and Λp (right) pairs, for ^{6}Li (top), ^{9}Be (middle), and ^{16}O targets (bottom). The kinematical threshold and the near-threshold region are shown in red lines.

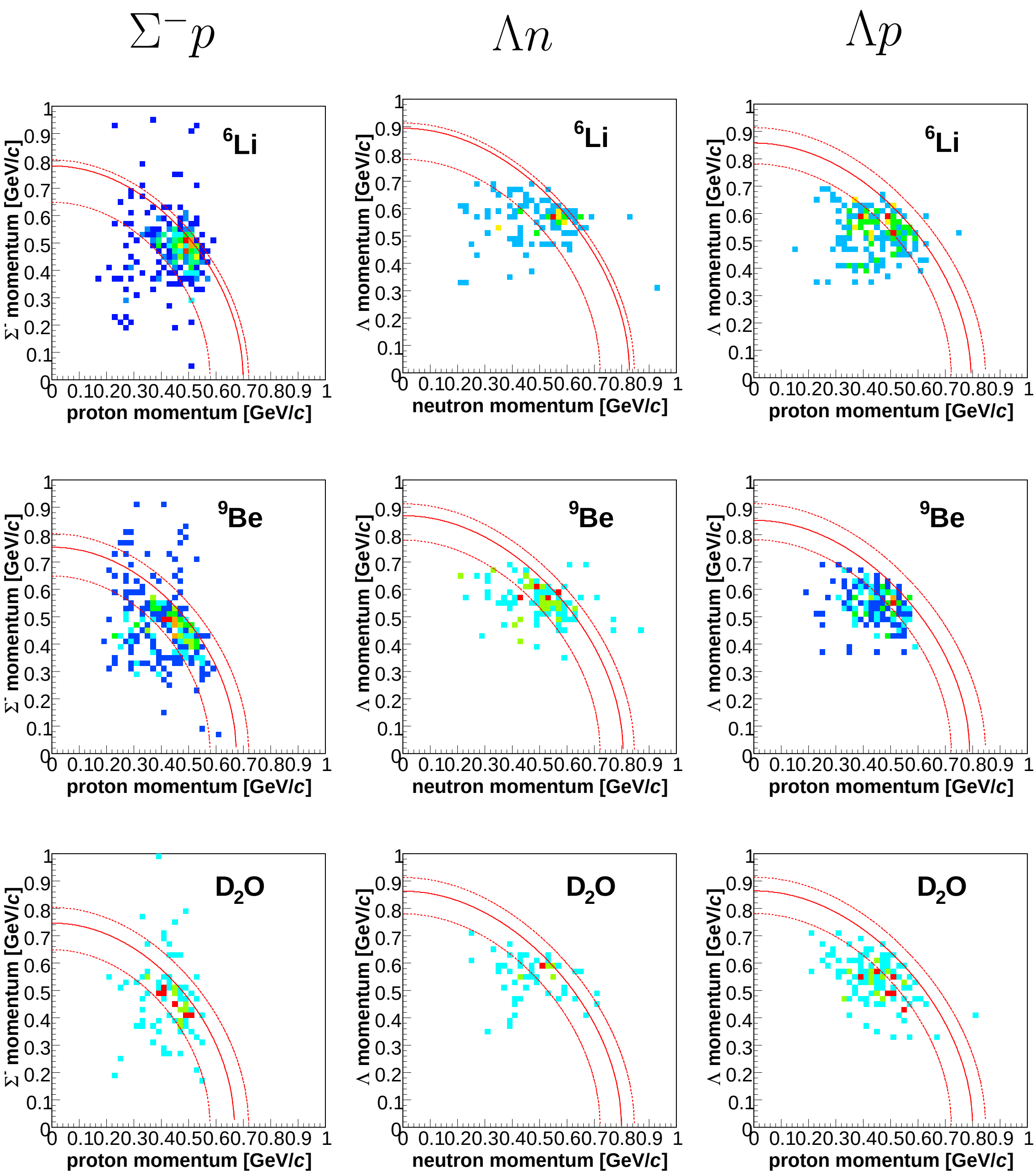

Figure 5.2: Two-dimensional momentum spectra of correlated $\Sigma^- p$ (left), Λn (middle), and Λp (right) pairs, for ^{6}Li (top), ^{9}Be (middle), and ^{16}O targets (bottom). The kinematical threshold and the near-threshold region are shown in red lines.

5.2.1 Few-body calculation on the K^-pp system

ATMS method

Yamazaki and Akaishi applied a variational ATMS method and obtained the binding energy (B) of 48 MeV and the decay width (Γ) of 61 MeV [46] (see Fig. 1.5). The average distance between the nucleons is 1.90 fm, which is much smaller than that for a deuteron (3.90 fm).

Phenomenological model

A phenomenological model using oscillator wave functions, whose frequencies were defined so as to reproduce the experimental mass and width of $\Lambda(1405)$ in the same framework, was used for the calculation. According to their calculation, the binding energy is $B = 118$ MeV, and the partial width of non-pionic decay channels is $\Gamma^{(\mathrm{non-pion.})} = 58$ MeV [91].

Coupled-channel approach

Shevchenko *et al.* [92,93] performed a coupled-channel Faddeev calculation of $\overline{K}NN$–$\pi\Sigma N$. A quasibound state was found in the range of $B \sim 55$–70 MeV and $\Gamma \sim 90$–110 MeV, depending on the scattering length of K^-p interaction.

Similarly, Ikeda *et al.* [94] obtained the energy of the $\overline{K}NN$ resonance by the $\overline{K}NN$–πYN coupled-channel Faddeev calculation, both in non-relativistic and relativistic models. Again, the result is strongly dependent especially on $I = 0$ $\overline{K}N$–$\pi\Sigma$ interaction; the binding energy is 60–95 MeV and the width is 45–80 MeV in case of the relativistic one.

Skyrme model

The bound kaon approach has been used for describing hyperons and $\Lambda(1405)$ in the Skyrme model [95]. In this approach, two Skyrmions are fixed and the kaon field is fluctuating around them. By changing the relative distance between two Skyrmions, they found the s-wave K^- has stronger binding than p-wave K^- and the numerical result of the binding energy is more than 200 MeV even if the distance between two protons is rather large (~ 2.0 fm). An updated calculation taking into account the radial motions of two protons shows the total binding energy of ~ 126 MeV, with the mean square radius of two protons ~ 1.6 fm [96].

AMD calculation

Doté *et al.* applied Antisymmetrized Molecular Dynamics (AMD) calculation, with s- and p-wave $\overline{K}N$ interactions. p-wave interaction may assist further binding because of the existence of the $\Sigma(1385)$ resonance. A preliminary result is shown in Ref. [97].

$\Lambda(1405)$-hypernuclei

Arai *et al.* assumed "kaon bound states" as Λ^*-hypernuclear states and investigated Λ^*N interaction in one-boson exchange picture [98]. Then, the K^-pp system was regarded as the two-body Λ^*N system. The coupling constant $g_{\Lambda^*\Lambda^*\sigma}$ was taken as a free parameter since there is no experimental information about it. The σ-exchange potential is attractive in medium range, cancelling the repulsion of the ω-exchange one. In the short range, the ω-exchange potential is strongly attractive, especially for the spin triplet. Therefore, the lowest Λ^*N state has its spin 1, while the assumption of K^-pp naturally gives a different result of the spin 0 because of the strong attraction in $I = 0$ $\overline{K}N$ pairs.

5.2.2 Production of K^-pp subsystem via kaon absorption

Figure 5.3 shows the invariant mass distribution, corrected for acceptance event by event, as described in the previous section. The invariant mass of a Λ and a proton is expressed as:

$$M = \sqrt{(E_\Lambda + E_p)^2 - (\vec{p}_\Lambda + \vec{p}_p)^2}, \tag{5.1}$$

where $\vec{p}$ denotes the three-dimensional momentum of each particle. The distribution obtained for each target of a Λ and a proton is consistent with that obtained in the first data taking (^{6}Li+^{7}Li+^{12}C) [66], and an obvious difference among five targets was not observed. However, it is not possible to definitely conclude whether the distribution is target-dependent or not with the present statistics. If the main contribution in the bound region is the two-body decay of K^-pp into Λp, the distribution should be independent of the target. The small A-dependence of the distribution (C) infers the production of K^-pp subsystem.

Even if we assume the existence of the K^-pp bound state, the fitting to this invariant mass distribution is not simple. Since the invariant mass distribution crosses the $\Sigma\pi$ decay threshold, the distribution may not be a simple Breit-Wigner form [99]. Moreover, if there exists another decay mode of $K^-pp \to \Sigma^0 p$, it would modify the Λp invariant mass distribution, because the FINUDA spectrometer can not discriminate the Λ from $\Sigma^0 \to \Lambda\gamma$ with the directly produced Λ. If we know the branching ratio into Λp and $\Sigma^0 p$, we could estimate this effect. However, at this moment we have no experimental and theoretical information, except for a phenomenological model by Ivanov *et al.* [91]. Nevertheless, the strength in the bound region is significantly larger than the near-threshold region, and the interpretation of a K^-pp state with $B_{\overline{K}} \gtrsim 50$MeV and moderately large decay width, as indicated by several theoretical calculations, does not contradict the experimental result.

5.3 Alternative interpretations of correlated Λp pairs

Several alternative interpretations against the existence of K^-pp bound state are proposed such as

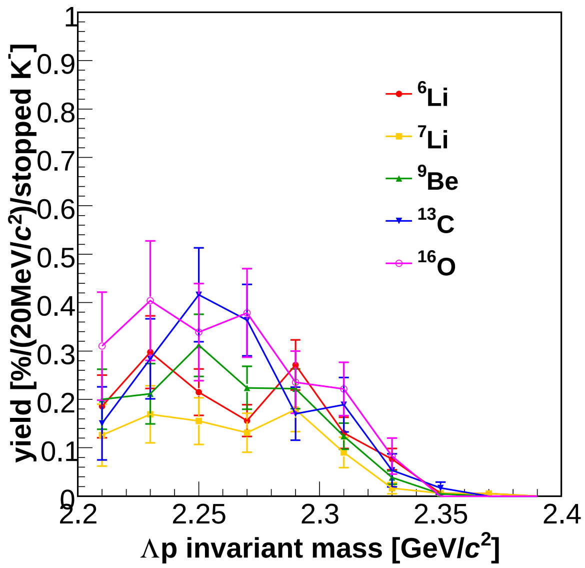

Figure 5.3: Invariant mass distribution of back-to-back Λp pairs, corrected for acceptance. Events with $p_p > 300\,\mathrm{MeV}/c$, $p_\Lambda > 400\,\mathrm{MeV}/c$, and $\cos\theta(\Lambda p) < -0.80$ are selected.

- final state interaction, followed by quasi-free two-nucleon absorption,
- dominance of $\Sigma^0 + p$ channel over $\Lambda + p$ channel for quasi-free two-proton absorption,
- ΣN-ΛN conversion for Σ hyperon produced with two-nucleon absorption,
- non-mesonic decay of heavier kaonic nuclei.

In the following, I will discuss whether these interpretations are consistent with the observations obtained for Λn and $\Sigma^- p$, and Λp pairs.

5.3.1 Final state interaction

Magas *et al.* pointed out that the invariant mass spectrum of the back-to-back Λp pairs could be explained by assuming final state interaction (FSI) after QF-TNA [80, 100]. The rescattering of hyperons and/or nucleons with the residual nucleus changes their directions as well as their momenta. Due to this momentum loss, the invariant mass of the Λp is reduced as shown in Fig. 5.4. Their calculation also suggests a weaker back-to-back correlation of Λ and proton due to final state interaction (Fig. 5.5).

Of course, final state interaction should exist with a certain fraction and distort the invariant mass spectrum partially. However, the "survival probability", defined in [80], which is the probability that both Λ and proton escape from the daughter nucleus (in the ground state) without any collision, is definitively important in discussing the whole structure. They

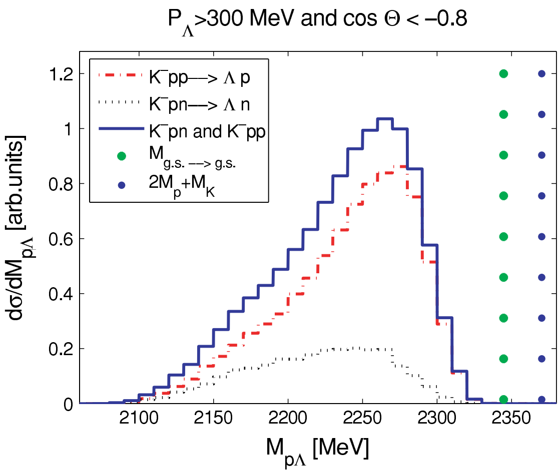

Figure 5.4: Invariant mass distribution of back-to-back Λp pairs with $p_\Lambda > 300\,\mathrm{MeV}/c$ and $\cos\Theta < -0.8$, from kaon absorption into ^{12}C. The contributions of quasi-free pp-absorption into Λp and pn-absorption into Λn with at least one collision (FSI) are indicated in red and black lines, respectively. Taken from Fig. 7 in [80].

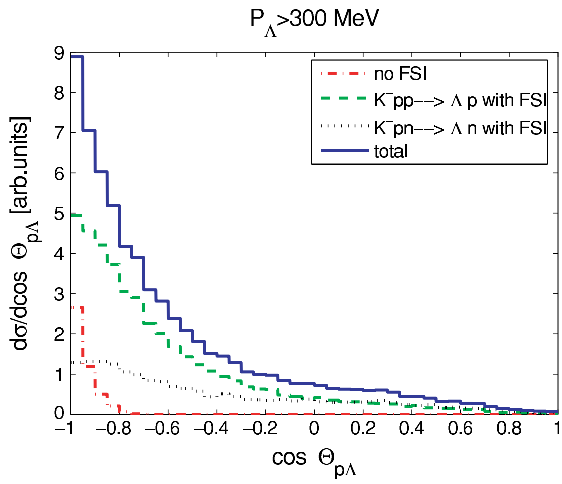

Figure 5.5: Opening angle distribution between a Λ and a proton from ^{12}C. The probability for no FSI events was assumed to be 10% and their contribution was shown in a red line. The contributions of quasi-free pp-absorption into Λp and pn-absorption into Λn are indicated in green and black lines, respectively. Taken from Fig. 8 in [80].

estimated the probability as ~ 0.4 for ^{12}C, for example. However, in order to explain the experimental result, they, at the end, fitted the whole spectrum with the distribution assuming one or more collisions. It means the survived probability is negligibly small, which seems to be unrealistic.

In their paper they discussed only the final state of Λ and proton. However, their model should be applied to the Λn pairs, resulting in a similar result, because the cross sections of $pN \to p'N'$ and $nN \to n'N'$ are almost the same.

The energy sum of the back-to-back Λn pairs has an enhancement near the kinematical threshold, as shown in Fig. 4.14. This enhancement together with the strong back-to-back correlation were well reproduced with a toy model of QF-TNA without any final state interaction. Therefore, the effect of the final state interaction seems to be negligible.

As for $\Sigma^- p$ pairs, either a proton and a Σ^- should looses its momentum after secondary collisions in their model. However, the momentum distributions are centered at the right momentum expected for the QF-TNA simulation as shown in Fig. 4.23. The strong angular correlation shown in Fig. 4.9, which is consistent to the simulation (Fig. 4.18), reinforces the interpretation that the contribution of final state interaction is not significantly large.

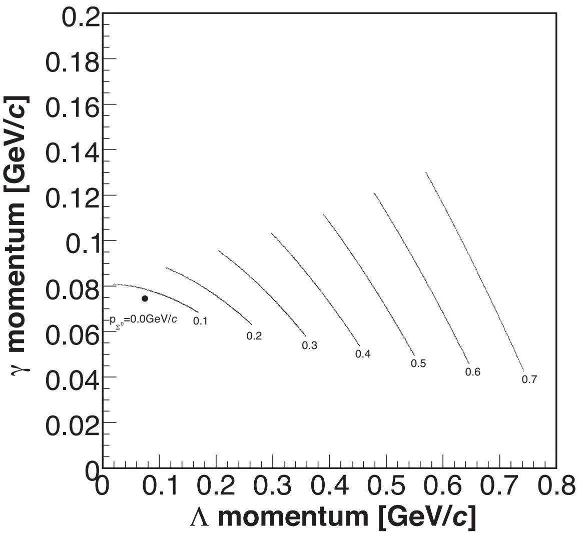

Figure 5.6: Momentum correlation for $\Sigma^0 \to \Lambda + \gamma$ decay with $p_{\Sigma^0} = 0.0, 0.1, \ldots, 0.7\,\mathrm{GeV}/c$.

Back again to the Λp pairs, it seems to be unrealistic that almost all the Λp pairs are suffered from the final state interaction after QF-TNA, while almost all the Λn and $\Sigma^- p$ pairs are not suffered from the final state interaction after QF-TNA. The observed channel dependence (A) can be hardly explained by the FSI assumption.

5.3.2 Dominance of $\Sigma^0 p$ channel

The final state of a (quasi-free) two-proton absorption process can be Λp or $\Sigma^0 p$. Because a Σ^0 hyperon decay into $\Lambda + \gamma$ with electromagnetic interaction, the final states are observed as Λp pairs for both. The energy sum of Λp is decreased from that of $\Sigma^0 p$ by the energy of missing γ. As shown in Fig. 5.6, the energy of γ from the decay of $500\,\mathrm{MeV}/c$ Σ^0, which is expected to be emitted from QF-TNA, distributes between $\sim 50\,\mathrm{MeV}$ and $\sim 110\,\mathrm{MeV}$. If we assume that the $\Sigma^0 p$ final state dominates over the Λp final state after the quasi-free two-nucleon absorption, the energy sum distribution may be explained qualitatively.

Nevertheless, this assumption contradicts an old experimental result of kaon absorption in ^{4}He by Katz *et al.* [67] They obtained the branching ratios of non-pionic Σ^+ and Σ^- events as $1.0 \pm 0.4\%$ and $(1.6 \pm 0.6) + (2.0 \pm 0.7)\%$ per stopped K^-. Assuming the isospin symmetry, the branching ratio of non-pionic Σ^0 events was estimated as $2.3 \pm 1.0\%$. To the contrary, the branching ratio of non-pionic Λ or Σ^0 events was found to be $11.7 \pm 2.4\%$. By subtraction, the non-pionic Λ fraction was deduced as $9.4 \pm 2.6\%$. It means the dominance of Λ over Σ^0. However, it is uncertain whether we can trust the isospin symmetry for two-nucleon absorption processes.

Recently, Oset and Toki recalculated the Σ^0 yield without assuming the isospin symmetry [49]. They assumed the Σ^0-to-Λ ratio for quasi-free absorption or for in-flight reaction ($p_{K^-} = 100\,\mathrm{MeV}/c$) to be the same also as that for two-nucleon absorption. They obtained two corresponding results; 3.7% for Σp and 3.1% for Λp with the former case, and 4.88% and 1.95% with the latter case. Here, Σ indicates not only Σ^0 but also Σ^-. Reminded of the experimental Σ^- fraction of 3.6%, their result also shows the Λ dominance over Σ^0 by factor of more than 2 [80].

Therefore, it is not reasonable to assume the branching ratio into $\Sigma^0 p$ is much larger than that into Λp. In other words, so as to explain the channel dependence (A), the fraction of Σ^0 contribution over Λ contribution must be extremely different between Λp and Λn.

5.3.3 ΣN-ΛN conversion

It is known that most of slow Σ's ($\lesssim 300\,\mathrm{MeV}/c$) produced with quasi-free one-nucleon absorption undergo so-called ΣN-ΛN conversion. For ^{4}He, a conversion probability as large as $50 \pm 10\%$ was estimated [67]. This is because of a large cross section of the elementary reaction $\Sigma N \to \Lambda N$ in this momentum range. For faster Σ ($\sim 500\,\mathrm{MeV}/c$) from two-nucleon absorption, the measured cross section of $\Sigma^- + p \to \Lambda + n$ [101] indicates somewhat lower probability. Magas *et al.* estimated the conversion probability for ^{12}C to be 37% [80]. As discussed in their paper, this conversion breaks the angular correlation between hyperon and nucleon.

If the forward cross section in the laboratory system is predominantly large, the back-to-back correlation may be held as before. The difference of the energy sum after the conversion is defined as:

$$\Delta E = (E_\Sigma + E_N) - (E_{\Lambda'} + E_N) = E_\Sigma - E_{\Lambda'}, \tag{5.2}$$

where Λ' indicates the converted Λ. Assuming the reaction is uniformly distributed in the center-of-mass system, the correlation between the scattering angle and the energy difference was obtained as Fig. 5.7. This result shows a forward scattering ($\cos\theta^{\mathrm{Lab}}(\Sigma\Lambda) \sim 1$) causes a small shift ($< 50\,\mathrm{MeV}$). If the initial state ΣN distributes near the threshold, the energy sum of the converted Λ and N distributes still near the threshold. Therefore, it is difficult to explain the back-to-back correlation and the decrease of the energy sum for Λp pairs simultaneously.

Furthermore, if the ΣN-ΛN conversion is important in the observed Λp pairs, the same should hold for the observed Λn pairs. The conversion itself does not explain the difference between observed distributions for the Λp and Λn pairs (A).

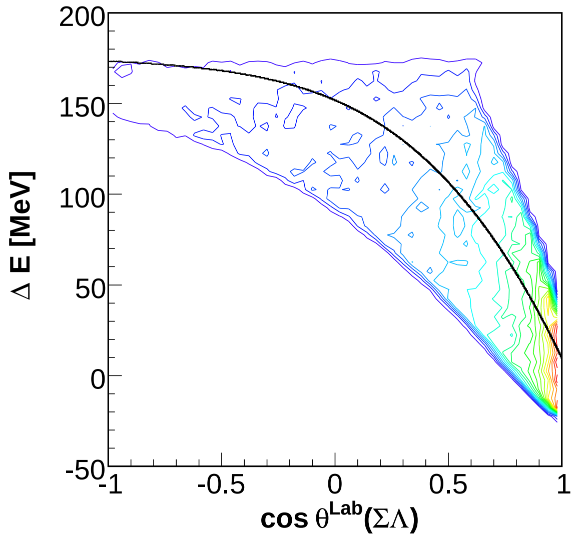

Figure 5.7: Correlation between the scattering angle ($\theta^{\mathrm{Lab}}(\Sigma\Lambda)$) and the energy difference (ΔE) for the reaction $\Sigma N \rightarrow \Lambda N'$. The black line is the result for $p_N = 0\,\mathrm{MeV}/c$, and the contour map is for $p_N = 200\,\mathrm{MeV}/c$.

5.3.4 Decay of heavier kaon bound states

Mareš *et al.* suggested a different interpretation from QF-TNA [28]. According to their interpretation, Λ and proton are the decay products of heavier kaon bound states produced with the (K^-_{stop}, N) reaction. Similar to non-mesonic weak decay of Λ-hypernuclei ($\Lambda + N \rightarrow N + N$), a back-to-back correlation between Λ and proton from a non-mesonic decay ($K^- + pp \rightarrow \Lambda + p$) is expected in the center-of-mass system of the bound state.

The binding energy of the kaon inside a bound state of ${}^{A}_{K^-}[Z-1](= {}^{A}Z \otimes K^-)$ can be related to the energy sum:

$$E_\Lambda + E_p + M({}^{A-2}(Z-2)^*) + T({}^{A-2}(Z-2)^*) = M({}^{A}Z) + M(K^-) - B_{K^-} + T({}^{A}_{K^-}[Z-1]), \tag{5.3}$$

where T is the kinetic energy. Then, the binding energy is expressed as:

$$B_{K^-} = \{M(K^-)c^2 + 2M(p)c^2 - S_{2p}({}^{A}Z) - Ex({}^{A-2}(Z-2)^*) + T({}^{A}_{K^-}[Z-1]) - T({}^{A-2}(Z-2)^*)\} - (E_\Lambda + E_p). \tag{5.4}$$

Because the kinetic energy of the initial state or the residue is small if Z is large enough and they cancel each other, the binding energy is approximately the same as the difference between the kinematical threshold and the energy sum. In this picture, the acceptance-corrected energy sum distribution (Fig. 4.7) should exhibit the strength in the bound region.

The distribution may be dependent on the target, because the produced kaon bound states are different from each other. However, a clear target dependence was not observed (C). Moreover, it may be difficult to explain the observed difference in the shapes of angular correlation and energy sum distribution between the Λp and Λn pairs (A), as far as the decay modes of both Λp and Λn occur.

Chapter 6

Conclusion

We performed the second data taking of the FINUDA experiment at the ϕ-factory DAΦNE to investigate the kaon absorption processes on p-shell nuclei (^{6}Li, ^{7}Li, ^{9}Be, ^{13}C, and ^{16}O). The total integrated luminosity of $966\,\mathrm{pb}^{-1}$ was accumulated, and about 10 times better statistics of data with the main trigger mode were obtained compared with that in the first data taking.

Non-mesonic absorption reactions of K^- at rest were studied by observing high momentum hyperons with their momenta $\gtrsim 400\,\mathrm{MeV}/c$. The hyperons, Λ and Σ^-, were identified with their invariant mass of a proton and a π^- for Λ, and a neutron and a π^- for Σ^-. It was found that these hyperons are emitted with a correlated nucleon in the opposite direction. We observed, for the first time, these correlated hyperon-nucleon pairs in three combinations: a Λn pair and $\Sigma^- p$ pair which comes from K^- absorption on a pn pair, and a Λp pair which comes from K^- absorption on a pp pair. The exclusive measurement of hyperon-nucleon pairs with the large-acceptance spectrometer allowed us to evaluate their yields directly.

For the K^- absorption on a pp pair, we found no enhancement of the energy sum distribution of Λp pairs near the energy threshold. The total yield of events with $p_\Lambda > 400\,\mathrm{MeV}/c$, $p_p > 300\,\mathrm{MeV}/c$ and $\cos\theta(\Lambda p) < -0.80$ was 0.9–2.4%. If we selected the energy sum between 2.30 and 2.38 GeV as a near-threshold region, the yield in the near-threshold region was estimated to be 0.2–0.4%, which is about 1/5 of the total yield, almost independent of the target.

On the other hand, for the K^- absorption on a pn pair, the energy sum and the angular correlation of two particles show the distributions consistent with a simple quasi-free K^- absorption on a quasi-deuteron in a target nucleus. The yields of the quasi-free two-nucleon absorption, by selecting the energy sum region between 2.30 and 2.38 GeV and the back-to-back region of $\cos\theta(\Lambda n) < -0.95$ and $\cos\theta(\Sigma^- p) < -0.90$, were obtained to be 2–3% per stopped K^- for Λn and 0.2–1.1% for $\Sigma^- p$, slightly depending on the targets. The yield below the near-threshold region was estimated by using the inclusive yield of Λ's above $400\,\mathrm{MeV}/c$, and it is $\sim 2\%$ per stopped K^- at most.

From the obtained yields of Λp and Λn, it was found that their energy sum distributions are largely different in the concentration in the near-threshold region. The energy sum of the Λp pairs mainly distribute far below the threshold, which is common to all the targets. It indicates a small A-dependence of the distribution.

As an explanation to the emission of the Λp pairs, a $K^- pp$ bound state formation in the K^- two-nucleon absorption on a pp pair was examined. The angular correlations and the invariant mass spectra of the Λp pairs were obtained target by target. We found a small target dependence of the distributions, and they agree with those obtained in the first data taking for light nuclei (^{6}Li+^{7}Li+^{12}C). This is consistent with the $K^- pp$ assumption. Various alternative interpretations were discussed; for example, final state interaction, Σ^0 decay, or ΣN-ΛN conversion, after the quasi-free two-nucleon absorption, and the existence of heavier kaonic nuclei. However, none of them could hardly explain the experimental observation, especially the channel dependence between the Λp and Λn pairs.

In conclusion, the energy sum distribution of the Λp pairs might be possible evidence of the formation of antikaon-nuclear bound states $K^- pp$, in the stopped K^- absorption reactions for p-shell nuclei. It would be extended to an experiment with a light nuclear target, such as liquid helium-3 or helium-4, by which an exclusive measurement of all the final state particles might be possible. Not only stopped K^- absorption but also the in-flight K^- reaction might be applicable to produce the light kaon bound states.

Acknowledgments

First of all, I would like to express my sincere gratitude to Prof. Tomofumi Nagae, who had been my supervisor until he moved to Kyoto University in July 2007. Five years ago when I entered the graduate school, he suggested me to join the FINUDA experiment, which was about to start the data taking with the aim of hypernuclear physics. I had discussed with him the possibility to study K^--nuclear bound states, which had been already predicted by Akaishi and Yamazaki. There are very few guidelines on this topic, because we are the first to succeed in the direct observation of a pair of hyperon and nucleon in kaon absorption. Without his warm words of encouragement and shrewd adivces, it would be difficult to bring the data analysis to a conclusion.

I would like to express my appreciation to Prof. Tullio Bressani, who is the former spokesperson of the FINUDA experiment. He accepted my proposal to study a completely new topic related to K^--nuclear bound states and two-nucleon absorption processes. His continuous encouragement stimulated my research.

I am deeply grateful to Dr. Vincenzo Lucherini, who was the run coordinator for the first and second data taking, and is the new spokesperson for the coming data taking. I could have useful discussions with him during my stay in Frascati, and he also assisted my daily life in Frascati.

I am really indebted to the offline analysis members, especially Dr. Alessandra Fillippi and Dr. Stefano Piano. I could develop the simulation and reconstruction codes so as to study two-nucleon absorption with their help. Elaborate discussions with them are invaluable to me.

I would like to show my sincere thanks to Prof. Luigi Busso, Dr. Michiko Sekimoto, Dr. Diego Faso, and Dr. Tomofumi Maruta. I learned a lot from the experience of the assemby and performance check of the TOFINO detector system with them.

I am greatly thankful to Dr. Haruhiko Outa. He has a longstanding experience of experiments with the stopped K^- method from 1980's. I learned the basic of the absorption reaction as well as general experimental techniques from him.

I acknowledge Dr. Akihisa Toyoda, Mr. Daisuke Nakajima, and Mr. Tomonori Takahashi. While they have their own tasks elsewhere, they spent time taking experimental shifts during data taking.

I would like to thank all the members of the FINUDA collaboration and the DAΦNE accelelerator division. I could not complete my thesis without the success of the data taking. I am really respectful to sustained efforts from the beginning of the construction of the spectrometer more than a decade ago, and to the stable operation of the DAΦNE accelerator for more than a half year.

I want to address my gratitude to Prof. Yoshinori Akaishi, Prof. Toshimitsu Yamazaki, and Dr. Akinobu Doté. Their stimulating theoretical calculations triggered my interest. I had extensive discussions with them from the structure of kaon bound states to interpretations of our observations.

I had a chance to join the KEK-PS E559 experiment in the interval of the data taking of the FINUDA experiment. The E559 experiment searched for the Θ^+ pentaquark by the $p(K^+, \pi^+)$ reaction. I would like to express my thanks to the spokesperson Prof. Ken'ichi Imai for giving me an opportunity to experience a different experiment from FINUDA. I am thankful also to the all the members of the experiment, including the core members of Prof. Toshiyuki Takahashi, Dr. Koji Miwa, Mr. Masashi Hayata, Mr. Seishi Dairaku, and Mr. Daisuke Nakajima.

I owe my deep gratitude to Prof. Naohito Saito, my present supervisor. He continuously encouraged me from time to time when I was writing this thesis.

I sincerely express my gratefulness to the referees of my thesis: Prof. Tomohiro Uesaka (chief), Prof. Satoru Yamashita, Prof. Tetsuo Hatsuda, Prof. Eiji Ideguchi, and Prof. Hiroari Miyatake. This thesis would be never completed without their sharp comments and advices. Especially Prof. Uesaka devoted lots of time for the revision of my thesis.

Last but not least, I express my deep appreciation to my family and friends for their continuous supports and encouragements.

Bibliography

[1] A. D. Martin, Nucl. Phys. **B179**, 33 (1981).

[2] J. D. Davies *et al.*, Phys. Lett. **B83**, 55 (1979).

[3] M. Izycki *et al.*, Z. Phys. A **297**, 11 (1980).

[4] P. M. Bird *et al.*, Nucl. Phys. **A404**, 482 (1983).

[5] M. Iwasaki *et al.*, Phys. Rev. Lett. **78**, 3067 (1997).

[6] T. M. Ito *et al.*, Phys. Rev. C **58**, 2366 (1998).

[7] G. Beer *et al.*, Phys. Rev. Lett. **94**, 212302 (2005).

[8] For example, J. Marton (SIDDHARTA Collaboration), arXiv:nucl-ex/0703028.

[9] J. Gasser, V. E. Lyubovitskij, and A. Rusetsky, arXiv:0711.3522 [hep-ph].

[10] N. Kaiser, P. B. Siegel, W. Weise, Nucl. Phys. **A594**, 325 (1995).

[11] A. Cieplý, E. Friedman, A. Gal, and J. Mareš, Nucl. Phys. **A696**, 173 (2001).

[12] A. Cieplý and J. Smejkal, arXiv:0711.4928 [hep-ph].

[13] T. Hyodo, S. I. Nam, D. Jido, and A. Hosaka, Phys. Rev. C **68**, 018201 (2003).

[14] B. Borasoy, R. Nißler, and W. Weise, Phys. Rev. Lett. **94**, 213401 (2005).

[15] B. Borasoy, R. Nißler, and W. Weise, Eur. Phys. J. **A25**, 79 (2005).

[16] B. Borasoy, U. G. Meissner, and R. Nißler Phys. Rev. C **74**, 055201 (2006).

[17] C. J. Batty, E. Friedman, and A. Gal, Phys. Rep. **287**, 385 (1997), and references therein.

[18] T. Waas, N. Kaiser, W. Weise, Phys. Lett. **B365**, 12 (1996).

[19] J. Schaffner-Bielich, V. Koch, and M. Effenberger, Nucl. Phys. **A669**, 153 (2000).

[20] A. Ramos and E. Oset, Nucl. Phys. **A671**, 481 (2000).

[21] A. Baca, C. García-Recio, and J.Nieves, Nucl. Phys. **A673**, 335 (2000).

[22] S. Hirenzaki, Y. Okumura, H. Toki, E. Oset, and A. Ramos, Phys. Rev. C **61**, 055205 (2000).

[23] L. Tolós, A. Ramos, A. Polls, and T. T. S. Kuo, Nucl. Phys. **A690**, 547 (2001).

[24] L. Tolós, A. Ramos, and E. Oset, Phys. Rev. C **74**, 015203 (2006).

[25] E. Friedman, A. Gal, and C. J. Batty, Phys. Lett. **B308**, 6 (1993).

[26] E. Friedman, A. Gal, and C. J. Batty, Nucl. Phys. **A579**, 518 (1994).

[27] E. Friedman, A. Gal, J. Mareš, and A. Cieplý, Phys. Rev. C **60**, 024314 (1999).

[28] J. Mareš, E. Friedman, and A. Gal, Nucl. Phys. **A770**, 84 (2006).

[29] N. Barnea, E. Friedman, Phys. Rev. C **75**, 022202(R) (2007).

[30] E. Friedman and A. Gal, Phys. Rep. **452**, 89 (2007).

[31] J. Yamagata, H. Nagahiro, Y. Okumura, and S. Hirenzaki, Prog. Theor. Phys. **114**, 301 (2005); errata ibid. **114**, 905 (2005).

[32] J. Yamagata, H. Nagahiro, and S. Hirenzaki, Phys. Rev. C **74**, 014604 (2006).

[33] J. Yamagata and S. Hirenzaki, Eur. Phys. J **A31**, 255 (2007).

[34] T. Kishimoto, Phys. Rev. Lett. **83**, 4701 (1999).

[35] T. Kishimoto *et al.*, Prog. Theor. Phys. Suppl. **149**, 264 (2003).

[36] T. Kishimoto *et al.*, Nucl. Phys. **A754**, 383c (2005).

[37] T. Kishimoto *et al.*, Prog. Theor. Phys. Suppl. **168**, 573 (2007).

[38] T. Waas, N. Kaiser, and W. Weise, Phys. Lett. **B379**, 34 (1996).

[39] T. Waas and W. Weise, Nucl. Phys. **A625**, 287 (1997).

[40] D. B. Kaplan and A. E. Nelson, Phys. Lett. **B175**, 57 (1986).

[41] A. E. Nelson and D. B. Kaplan, Phys. Lett. **B192**, 193 (1987).

[42] W. Scheinast *et al.*, Phys. Rev. Lett. **96**, 072301 (2006).

[43] Y. Nogami, Phys. Lett. **7**, 288 (1963).

[44] S. Wycech, Nucl. Phys. **A450**, 399c (1986).

[45] Y. Akaishi and T. Yamazaki, Phys. Rev. C **65**, 044005 (2002).

[46] T. Yamazaki and Y. Akaishi, Phys. Lett. **B535**, 70 (2002).

[47] A. Doté, Y. Akaishi, H. Horiuchi, and T. Yamazaki, Phys. Lett. **B590**, 51 (2004).

[48] A. Doté, H. Horiuchi, Y. Akaishi, and T. Yamazaki, Phys. Rev. C **70**, 044313 (2004).

[49] E. Oset and H. Toki, Phys. Rev. C **74**, 015207 (2006).

[50] D. Jido, J. A. Oller, E. Oset, A. Ramos, and U. G. Meissner, Nucl. Phys. **A725**, 181 (2003).

[51] V. K. Magas, E. Oset, and A. Ramos, Phys. Rev. Lett. **95**, 052301 (2005).

[52] M. Iwasaki *et al.*, Nucl. Instrum. Methods **A473**, 286 (2001).

[53] T. Suzuki *et al.*, Phys. Lett. **B597**, 263 (2004).

[54] T. Suzuki *et al.*, arXiv:nucl-ex/0310018.

[55] T. Suzuki *et al.*, Nucl. Phys.**A754**, 375 (2005).

[56] Y. Akaishi, A. Doté, and T. Yamazaki, Phys. Lett. **B613**, 140 (2005).

[57] M. Sato *et al.*, Phys. Lett. **B659**, 107 (2008).

[58] M. Iwasaki *et al.*, Eur. Phys. J **A33**, 195 (2007).

[59] H. Yim *et al.*, Eur. Phys. J **A33**, 201 (2007).

[60] T. Suzuki *et al.*, Phys. Rev. C **76**, 068202 (2007).

[61] M. Agnello *et al.*, Phys. Lett. **B654**, 80 (2007).

[62] N. Herrman, Proceedings of the EXA05 Conference, Vienna 2005 (Austrian Academy of Sciences Press, 2005).

[63] T. Yamazaki, A. Doté, and Y. Akaishi, Phys. Lett. **B587**, 167 (2004).

[64] G. Bendisciolia *et al.*, Nucl. Phys. **A789**, 222 (2007).

[65] M. Agnello *et al.*, Nucl. Phys. **775**, 35 (2006).

[66] M. Agnello *et al.*, Phys. Rev. Lett. **94**, 212303 (2005).

[67] A. D. Katz *et al.*, Phys. Rev. D **1**, 1267 (1970).

[68] C. Vander Velde-Wilquet, J. Sacton, and J. H. Wickens, Nuovo Cimento (SERIE XI) **39A**, 538 (1977), and references therein.

[69] R. Seki and C. E. Wiegand, Annu. Rev. Nucl. Sci. 25, 241 (1975), and references therein.

[70] H. Davis *et al.*, Nuovo Cimento (SERIE X) **53A**, 313 (1968).

[71] S. Ozaki, R. Weinstein, G. Glass, E. Loh, L. Neimala, and A. Wattenberg, Phys. Rev. Lett. **4**, 533 (1960).

[72] B. Bassalleck, H. D. Engelhardt, E. L. Haase, W. D. Klotz, C. W. Lewis, F. Takeuchi, H. Ullrich, and M. Furić, Phys. Lett. **65B**, 238 (1976).

[73] B. Bassalleck, W. D. Klotz, F. Takeutchi, H. Ullrich, and M. Furić, Phys. Rev. C **16**, 1526 (1977).

[74] B. Bassalleck, W. D. Klotz, F. Takeutchi, H. Ullrich, and M. Furić, Z. Phys. **A286**, 401 (1978).

[75] B. Bassalleck, E. L. Haase, W. D. Klotz, F. Takeutchi, H. Ullrich, M. Furić, and Y. Sakamoto, Phys. Rev. C **19**, 1893 (1979).

[76] B. Bassalleck, H. D. Engelhardt, W. D. Klotz, C. W. Lewis, F. Takeutchi, H. Ullrich, and M. Furić, Nucl. Phys. **A343**, 365 (1980).

[77] P. Heusi, H. P. Isaak, H. S. Pruys, R. Engfer, E. A. Hermes, T. Kozlowski, U. Sennhauser, and H. K. Walter, Nucl. Phys. **A407**, 429 (1983).

[78] N. F. Golovanova and N. S. Zelenskaya, Sov. J. Nucl. Phys. **8**, 158 (1969).

[79] K. Shimizu and A. Faessler, Nucl. Phys. **A333**, 495 (1980).

[80] V. K. Magas, E. Oset, A. Ramos, and H. Toki, Phys. Rev. C **74**, 025206 (2006).

[81] T. Bressani, Proc. Workshop on Physics and Detectors for DAΦNE, Frascati, Italy, April 9-12, 1991 (ed G. Pancheri, Servizio Documentazione dei Laboratori Nazionali di Frascati dell'INFN).

[82] The FINUDA Collaboration, M. Agnello *et al.*,"FINUDA, a detector for nuclear physics at DAΦNE", LNF publication LNF-93/021(IR) (1993).

[83] The FINUDA Collaboration, M. Agnello *et al.*, "FINUDA technical report", LNF publication LNF-95/024(IR) (1995).

[84] W. -M. Yao *et al.*, J. Phys. G **33**, 1 (2006).

[85] The LNF DAΦNE Home Page. (http://www.lnf.infn.it/acceleratori)

[86] H. Tamura, R. S. Hayano, H. Outa, and T. Yamazaki, Prog. Theor. Phys. Suppl. **117**, 1 (1994).

[87] E. Fermi and E. Teller, Phys. Rev. **72**, 399 (1947).

[88] C. T. Murphy, G. Keyes, M. Saha, and M. Tanaka, Phys. Rev. D **9**, 1255 (1974).

[89] T. Yamazaki and Y. Akaishi, Nucl. Phys. **A792**, 229 (2007).

[90] T. Suzuki *et al.*, arXiv:0711.4943 [nucl-ex].

[91] A. N. Ivanov, P. Kienle, J. Marton, and E. Widmann, arXiv:nucl-th/0512037.

[92] N. V. Shevchenko, A. Gal, and J. Mareš, Phys. Rev. Lett. **98**, 082301 (2007).

[93] N. V. Shevchenko, A. Gal, J. Mareš, and J. Revai, Phys. Rev. C **76**, 044004 (2007).

[94] Y. Ikeda and T. Sato, Phys. Rev. C **76**, 035203 (2007).

[95] T. Nishikawa and Y. Kondo, arXiv:hep-ph/0703100.

[96] T. Nishikawa and Y. Kondo, arXiv:0710.0948 [hep-ph].

[97] T. Doté and W. Weise, Eur. Phys. J **A33**, 249 (2007).

[98] A. Arai, M. Oka, and S. Yasui, arXiv:0705.3936 [nucl-th].

[99] For example, talk by Y. Akaishi at Chiral07. (http://www.rcnp.osaka-u.ac.jp/~chiral07/)

[100] A. Ramos, V. K. Magas, E. Oset, H. Toki, Eur. Phys. J **A33**, 273 (2007).

[101] D. Stephen, Ph.D. thesis, University of Massachusetts (1970).